Ultrasound markers for cancer

Ultrasound Markers for Cancer

The research presented in this thesis was financially supported by the European Research Council (ERC), the Dutch Technology Foundation STW, and the Dutch Cancer Society (KWF). Financial support for the printing of this thesis was kindly provided by Bracco Suisse SA.

Cover design by Jelle Janssen (www.jellejanssen.nl). Printed by Gildeprint.

A catalogue record is available from the Eindhoven University of Technology Library.

ISBN: 978-90-386-4423-3

Ultrasound Markers for Cancer

PROEFSCHRIFT

ter verkrijging van de graad van doctor aan de Technische Universiteit Eindhoven, op gezag van de rector magnificus prof. dr. ir. F. P. T. Baaijens, voor een commissie aangewezen door het College voor Promoties, in het openbaar te verdedigen op woensdag 17 januari 2018 om 16:00 uur

door

Ruud Johannes Gerardus van Sloun

geboren te Roermond

Dit proefschrift is goedgekeurd door de promotoren en de samenstelling van de promotiecommissie is als volgt:

voorzitter	prof.dr.ir. A.B. Smolders
promotor:	prof.dr.ir. H. Wijkstra
copromotor:	dr.ir. M. Mischi
leden:	prof.dr.ing. G. Schmitz (Ruhr-Universität)
	prof.dr. J. D'hooge (KU Leuven)
	dr. M. Averkiou (University of Washington)
	dr.ir. R.G.P. Lopata
adviseur:	dr. H.P. Beerlage (Jeroen Bosch Ziekenhuis)

Het onderzoek dat in dit proefschrift wordt beschreven is uitgevoerd in overeenstemming met de TU/e Gedragscode Wetenschapsbeoefening.

Summary

Ultrasound Markers for Cancer

Each year, about 14 million new cancer cases occur worldwide and over 8 million people die from it. Diagnostic imaging plays a critical role in cancer care, being a fundamental asset for timely cancer diagnosis, disease staging and management as well as for treatment choice, planning, guidance, and follow up. Despite this, imaging technologies that play a central role in this process, i.e. magnetic resonance imaging (MRI) and X-ray computed tomography (CT), have major drawbacks; MRI remains a highly expensive modality, and CT induces ionizing radiation. Moreover, in most cases their limited accuracy poses the need for invasive verification with biopsies. Ultrasound (US) imaging has the potential to shine as a non-ionizing and cost-effective technique that can limit the diagnostic burden on the healthcare system and the patient via an effective and accurate imaging protocol. In this dissertation, we aim to advance and extend ultrasound imaging to a level which will ultimately permit accurate cancer diagnosis based on ultrasound alone. To this end, we focus on imaging both vascular and tissue markers that are characteristic for cancer.

At the vascular level the impact of cancer is striking. Cancer vasculature is chaotic, characterized by increased microvascular density and tortuosity, as well as by the presence of irregular branching and arteriovenous shunts. The process that governs these vascular alterations is angiogenesis, a biomarker that is strongly associated to lethal cancer phenotypes. In the first part of this thesis, we therefore propose several novel methods based on contrast-enhanced ultrasound (CEUS) that characterize the vasculature, ranging from macroscopic features to microscopic features. CEUS enables these particular analyses by imaging intravenously administered microbubbles (sized similarly to red blood cells) flowing through the (micro)vasculature like red blood cells. On a macroscopic scale, we developed multiple signal processing systems that adequately assess microbubble dispersion, microbubble flow fields and flow heterogeneity. Clinically, all these markers proved to have diagnostic value for prostate cancer localization. At a smaller scale, we aim at evaluating features of the vascular net directly. We first introduce contrast-enhanced ultrasound tractography, setting a basis for characterization of microbubble trajectories. We proved that the proposed approach can directly be applied to clinically acquired 4D-CEUS datasets. Comparison with histopathology after prostate resection revealed higher densities and more tortuous geometries in malignant areas. Finally, at an even smaller scale, we adopted sparse reconstruction techniques to generate super-resolution ultrasound images of the vasculature using clinical CEUS, revealing features that were previously hidden by the diffraction limit. These developments open up additional opportunities for vascular characterization.

The above described methods rely on accurate detection and quantification of microbubbles. Yet, commercial CEUS imaging modes are not completely specific to microbubbles, leading to several artefacts. In this context, we investigated the use of a microbubble-specific marker for CEUS, a cumulative phase-shift between the second harmonic and fundamental of the ultrasound wave. A proof of concept aimed at quantification of microbubbles in a tomographic fashion showed the potential of this new technique.

Along with these vascular features, cancer tissue exhibits a specific set of characteristics. First of all, cancers are stiff compared to benign tissue. Physicians assess nodular firmness by palpation, a subjective technique with a long history in medicine. A fully quantitative measure of lesion stiffness can be obtained by shear wave elasticity imaging (SWEI), a method that uses a high-intensity acoustical "push" pulse to produce laterally propagating shear waves whose velocity can be estimated to obtain the shear modulus. However, not only elasticity, but also viscosity plays an important role in the propagation process of shear waves. In fact, viscosity is in itself a parameter of diagnostic value for detection and characterization of malignant lesions. In this thesis we therefore propose a new method that enables imaging of viscosity from SWEI by local model-based system identification. Our in-vitro studies indicated how this approach was for the first time able to provide high resolution viscosity maps, opening up the way for imaging this marker in the context of cancer diagnostics.

Besides viscoelastic remodelling, cancer tissue is dense with reduced fluid, as confirmed by diffusion-weighted MRI. The established link between fluid content and US nonlinear behaviour hence motivates towards the estimation of a marker that is able to quantify the nonlinear nature of ultrasound propagation. The acoustical coefficient of nonlinearity is a suitable marker, and we set the theoretical basis for a new method to image this parameter.

Although it is reasonable to belief that the new diagnostic options provided by this work will allow clinicians to harvest a broad and useful spectrum of information, the possibilities may be overwhelming. Therefore, incorporating the full set of US tools into a clearly defined multi-parametric protocol (mpUS) is of significant importance for clinical implementation of these techniques. Future work should therefore include the development an mpUS solution that suits the clinical workflow, and enables not only the detection and localisation of malignancies, but also their grading.

List of author's publications

Journal articles

[J-1] **van Sloun, R.J.G.**, Demi, L., Schalk, S.G., Caresio, C., Huang, J., Li, J., Postema, A.W., Mannaerts, Molinari, F., C., van der Linden, H., Huang, P., Wijkstra, H., Mischi, M., "In-vivo contrast-enhanced ultrasound tractography", *submitted*.

[J-2] Panfilova, A., Shelton, S., Caresio, C., **van Sloun, R.J.G.**, Molinari, F., Wijkstra, H., Dayton, P., Mischi, M., "On the relationship between dynamic contrast-enhanced ultrasound features and the underlying vascular architecture extracted from acoustic angiography", *in preparation*.

[J-3] Wildeboer, R.R., **van Sloun, R.J.G.**, Schalk, S.G., Mannaerts, C.K., van der Linden, J.C., Huang, P., Wijkstra, H., Mischi, M., "Convective-dispersion modelling in three-dimensional contrast-ultrasound imaging for the localization of prostate cancer", *in preparation*.

[J-4] Wildeboer, R.R., **van Sloun, R.J.G.**, Postema, A.W., Mannaerts, C.K., Mischi, M. and Wijkstra, H., "Accurate validation of ultrasound techniques for prostate cancer: challenges in registration of imaging and histopathology", *submitted*.

[J-5] Chen, C., Hendriks, G., **van Sloun, R.J.G.**, Hansen, R., de Korte, C., "Improved Plane Wave Ultrasound Beamforming by Incorporating Angular Weighting and Coherent Compounding in Fourier Domain", *in review*.

[J-6] **van Sloun, R.J.G.**, Wildeboer, R.R, Wijkstra, H., Mischi, M., "Viscoelasticity Mapping by Identification of Local Shear Wave Dynamics", *IEEE transactions on Ultrasonics, Ferroelectrics, and Frequency control*, accepted 2017.

[J-7] Demi, L., van Hoeve, W., **van Sloun, R.J.G.**, Demi, M., Soldati, G., "Lung Ultrasound Spectroscopy: Towards a Quantitative Measure of the State of the Lung", *Nature Scientific Reports*, accepted 2017.

[J-8] Postema, A.W., Scheltema M.J.V., Mannaerts, C.K., **van Sloun, R.J.G.**, Idzenga, T., Mischi, M., Engelbrecht, M.R.E., De la Rosette, J.J.M.C.H., Wijkstra, H.,"The prostate cancer detection rates of CEUS-targeted versus MRI-targeted versus systematic TRUS-guided biopsies in biopsy-naïve men: A prospective, comparative clinical trial using the same patients", *BMC Urology*, 2017.

[J-9] **van Sloun, R.J.G.**, Demi, L., Wijkstra, H., Mischi. M., "Mammography: developing a smarter and safer alternative", *Future Oncology*, 13(8), 2017 (Editorial article).

[J-10] **van Sloun, R.J.G.**, Demi, L., Postema, A.W., de la Rosette, JJMCH, Wijkstra, H., Mischi, M., "Entropy of ultrasound-contrast-agent velocity fields for angiogenesis imaging of prostate cancer", *IEEE transactions on Medical Imaging*, 2017 (Editorial selection as featured article & Best paper award 2015-2016 Benelux Chapter IEEE-EMBS).

[J-11] **van Sloun, R.J.G.**, Demi, L., Postema, A.W., de la Rosette, JJMCH, Wijkstra, H., Mischi, M., "Ultrasound-contrast-agent dispersion and velocity imaging for prostate cancer localization", *Medical Image Analysis*, 2016.

[J-12] Demi, L., **van Sloun, R.J.G.**, Wijkstra, H., Mischi, M., "Towards dynamic contrast-enhanced ultrasound tomography". *Nature Scientific Reports*, 2016.

[J-13] Demi, L., **van Sloun, R.J.G.**, Wijkstra, H., Mischi, M., "Cumulative phase delay imaging for contrast-enhanced ultrasound tomography". *Physics in Medicine and Biology*, 2015 (Editorial selection as featured article).

[J-14] **van Sloun, R.J.G.**, Pandharipande, A., Mischi, M., Demi, L., "Compressed sensing for ultrasound computed tomography", *IEEE transactions on Biomedical Engineering*, 2015.

[J-15] **van Sloun, R.J.G.**, Demi, L.; Shan, C., Mischi, M., "Ultrasound coefficient of nonlinearity imaging", *IEEE transactions on Ultrasonics Ferroelectrics, and Frequency control*, 2015 (IEEE TUFFC editor's selection 2016).

[J-16] **van Sloun, R.J.G.**, Srinivasan, S., Pandharipande, A., Sommen, P. C., "Ultrasonic array Doppler sensing for human movement classification", *IEEE Sensors Journal*, 2014

[J-17] Louter, M., **van Sloun, R.J.G.**, Pevernagie, D. A., Arends, J. B., Cluitmans, P. J., Bloem, B. R., Overeem, S., "Subjectively impaired bed mobility in Parkinson's disease affects sleep efficiency", *Sleep medicine*, 2013

International Conference Proceedings

[C-1] Panfilova, A., Shelton, S., **van Sloun, R.J.G.**, Caresio, C., Wijkstra, H., Dayton, P., Mischi, M., "On the relation between contrast-ultrasound kinetic features and microvascular density by acoustic angiography", *Acoustic bubbles in therapy: recent advances with medical microbubbles, clouds and harmonic antibubbles*, Tours, France, October 2017.

[C-2] **van Sloun, R.J.G.**, Solomon, O., Eldar, Y.C., Wijkstra, H., Mischi, M., "Sparsity-driven super-localization in clinical contrast-enhanced ultrasound", *Proceedings of the IEEE International Ultrasonics Symposium*, Washington, USA, September 2017.

[C-3] **van Sloun, R.J.G.**, Wildeboer, R.R., Wijkstra, H., Mischi, M., "Shear-wave imaging of viscoelasticity using local impulse-response identification", *Proceedings of the IEEE International Ultrasonics Symposium*, Washington, USA, September 2017.

[C-4] Wildeboer, R.R., **van Sloun, R.J.G.**, Schalk, S.G., Mannaerts, C.K., van der Linden, H., Huang, P., Wijkstra, H., Mischi, M., "Three-dimensional estimation of ultrasound-contrast-agent dispersion and convection in the prostate", *Proceedings of the IEEE International Ultrasonics Symposium*, Washington, USA, September 2017.

[C-5] Panfilova, A., Shelton, S., **van Sloun, R.J.G.**, Caresio, C., Wijkstra, H., Dayton, P., Mischi, M., "Which properties of the vascular architecture are reflected by dynamic contrast-enhanced ultrasound imaging of dispersion and wash-in rate? A comparison with acoustic angiography", *Proceedings of the IEEE International Ultrasonics Symposium*, Washington, USA, September 2017.

[C-6] Demi. L., van Hoeve. W., **van Sloun, R.J.G.**, Mischi, M., Demi. M., Soldati, G., "The native frequency of B-lines artifacts may provide a quantitative measure of the state of the lung", *Meeting of the Acoustical Society of America*, 2017.

[C-7] Demi. L., van Hoeve. W., **van Sloun, R.J.G.**, Wijkstra. H., Mischi. ,M., "Effects of a mono-disperse bubble population on the cumulative phase delay between second harmonic and fundamental component", *Meeting of the Acoustical Society of America*, 2017.

[C-8] **van Sloun, R.J.G.**, Demi, L., Postema, A.W., Saporito, S., Herold, I.H.F., Houthuizen, P., Korsten, H.H.M., Wijkstra, H., Mischi, M, "Velocity vector imaging based on time-delay estimation: applications to angiogenic perfusion and cardiac flow analysis", 22^{nd} *European Symposium on Ultrasound Contrast Imaging, Rotterdam*, The Netherlands, January 2017.

[C-9] **van Sloun, R.J.G.**, Demi, L., Postema, A.W., de la Rosette, J.J.M.C.H., Wijkstra, H., Mischi, M., "Statistical characterization of ultrasound-contrast-agent velocity fields for prostate cancer localization", *Proceedings of the IEEE International Ultrasonics Symposium*, Tours, France, September 2016.

[C-10] Panfilova, A., Shelton, S., **van Sloun, R.J.G.**, Demi, L., Kuenen, M., Wijkstra, H., Dayton, P., Mischi, M., "Does contrast ultrasound dispersion imaging reveal changes in vascular tortuosity? A comparison with acoustic angiograph", *Proceedings of the IEEE International Ultrasonics Symposium*, Tours, France, September 2016.

[C-11] Turco, S., Keravnou, C., **van Sloun, R.J.G.**, Wijkstra, H., Averkiou, M., and Mischi, M., "Effects of perfusion and vascular architecture on contrast dispersion: validation in ex-vivo porcine liver under machine perfusion", *Proceedings of the IEEE International Ultrasonics Symposium*, Tours, France, September 2016.

[C-12] Demi, L., **van Sloun, R. J.G.**, Wijkstra, H., Mischi, M., "Dynamic Contrast Specific Ultrasound Tomography", Meeting of the Acoustical Society of America, Honolulu, Hawaii, November 2016.

[C-13] Mischi, M., Turco, S., **van Sloun, R.J.G.**, Schalk, S., Demi, L., Wijkstra, H., "Contrast ultrasound dispersion imaging in prostate cancer: an update", 21^{th} *European Symposium on Ultrasound Contrast Imaging*, Rotterdam, The Netherlands, January 2016.

[C-14] Demi, L., **van Sloun, R.J.G.**, Shan, C., M. Verweij, Mischi, M.,"Ultrasound imaging of the coefficient of nonlinearity", *Meeting of the Acoustical Society of America*, Jacksonville Florida, November 2015.

[C-15] Demi, L., van Hoeve, W., Demi, M., van Sloun, R. J.G., Soldati, G., Mischi, M., "A new perspective for lung ultrasonography, preliminary results", *Meeting of the Acoustical Society of America*, Jacksonville Florida, November 2015.

[C-16] **van Sloun, R.J.G.**, Demi, L., Postema, A.W., de la Rosette, J.J.M.C.H., Wijkstra, H., Mischi, M., "Imaging the dispersion coefficient of ultrasound contrast agents by Wiener system identification for prostate cancer localization", *Proceedings of the IEEE International Ultrasonics Symposium*, Taipei, Taiwan, October 2015.

[C-17] **van Sloun, R.J.G.**, Demi, L., Shan, C., Mischi, M., "Imaging the ultrasonic coeffi-

cient of nonlinearity: the impact of speed of sound variations", *Proceedings of the IEEE International Ultrasonics Symposium*, Taipei, Taiwan, October 2015.

[C-18] **van Sloun, R.J.G.**, Pandharipande, A., Mischi, M., Demi, L., "Compressed sensing for beamformed ultrasound computed tomography", *Proceedings of the IEEE International Ultrasonics Symposium*, Taipei, Taiwan, October 2015.

[C-19] Demi, L., **van Sloun, R.J.G.**, Wijkstra, H., Mischi, M., "Cumulative Phase Delay Imaging – a new contrast enhanced ultrasound modality". *International Symposium on Nonlinear Acoustics*, Lyon, France, July 2015.

[C-20] Demi, L., **van Sloun, R.J.G.**, Zhao, X., Wijkstra, H., Mischi, M., "Cumulative Phase Delay Imaging – a new contrast enhanced imaging modality", 20^{th} *European Symposium on Ultrasound Contrast Imaging*, Rotterdam, The Netherlands, January 2015.

[C-21] **van Sloun, R.J.G.**, Pandharipande, A., Caicedo, D., Srinivasan, S., P. Sommen "Ultrasonic circular array sensing for human arm motion classification", *Proceedings of the* 4^{th} *IEEE International Conference on Consumer Electronics Berlin*, Berlin, Germany, September 2014.

International Patent applications

1. Mischi. M & van Sloun, R.J.G., "Imaging of dispersion and velocity of contrast agents", March 16, 2017.
2. Mischi. M & van Sloun, R.J.G., "Shear wave viscoelasticity imaging using local system identification", June 9, 2017.

Magazine article

1. **van Sloun, R.J.G.**, Wijkstra, H., Mischi, M., "Bubbels die kanker onthullen; belletjes in de bloedbaan voor lokalisatie van prostaatkanker", M*MT Integraal*, 2016.

Contents

1

Background and Motivation

This first chapter introduces the reader to current diagnostics in cancer, and highlights the motivation for the research conducted in the thesis.

1.1 The global burden of cancer

Each year, about 14 million new cancer cases occur worldwide and over 8 million people die from it. The increasing life expectancy causes the number of new cancer cases to rise moreover: if rates do not change, the global cancer burden is expected to increase to 21.7 million cases and 13 million deaths by 2030.[1] Breast cancer is the most common cancer in women, accounting for about 25% of all cases worldwide.[1] For western men, prostate cancer has the highest incidence (23%).[1]

The risk of being diagnosed with cancer increases substantially with age. In economically developed countries, 58% of all newly diagnosed cancer cases occur at 65 years of age and older, compared with 40% in developing countries.[1] This variation is predominantly caused by differences in age structure of the populations; developing countries have a smaller number of elderly people. According to the World Health Organization,[2] the impact of cancer is even more severe in low- and middle-income countries, where there is a lack of access to information about prevention, early detection, and treatment, as well as an inadequate medical and public health infrastructure. As a result, cancers are often diagnosed at a late stage, and people suffer needlessly from inadequate palliative care.

Along with the human toll of cancer, the financial cost is substantial. This obviously includes expenditures for treatment, as well as the cost of care and rehabilitation related to the disease. But also indirect costs such as the loss of economic output due to morbidity (missed work) and mortality (premature death) are sizeable. For example, the estimated cost of lost productivity due to premature cancer mortality in Europe in 2008 was €75 billion.[3] The exact total global cost of cancer is unknown, but it is estimated to be in the hundreds of billions of euros per year. This number is expected to rise even further due to the increased amount of new cancer cases, as well as the increasing cost of cancer therapies.[4]

Prostate cancer as a representative case

A striking, representative example in the western world is prostate cancer, the type of cancer with the highest incidence (27%) and second mortality rate (10%) in western men. Similar to breast cancer in women, one in seven men is diagnosed with prostate cancer in his lifetime; however, different from breast cancer, no reliable diagnostic imaging is available. To date, the only reliable diagnostics is based on multiple systematic biopsies. This procedure is invasive; a needle is inserted into the prostate for the collection of 12 or more tissue samples, according to a predefined scheme. Therefore, patient discomfort, costs, and risks of haemorrhages and infections are serious drawbacks. Moreover, repeated biopsy procedures are often necessary due to high false-negative rates of up to 41%,[5] while about 70% of biopsy procedures are in retrospect unnecessary due to poor patient stratification. In the United States alone, over 750,000 unnecessary biopsy procedures are performed each year, with related extra cost of about $1.5 billion/year.[6]

Timely and tailored treatment saves lives and is invaluable for reducing the burden on our society. Yet, it is limited by the complexity, cost, and/or invasiveness of available diagnostics today. A combination of complicated and expensive imaging modalities, along with invasive biopsy procedures, is usually required for cancer diagnosis.

1.2 Current cancer care

1.2a Diagnosis

Cancer diagnosis, including careful clinical and pathological assessments, is the first step to cancer management. Once a diagnosis is confirmed, the cancer must be staged and graded to determine treatment options and prognosis, and to apply the appropriate treatment protocols. A cancer's stage is based on the size or extent of the primary tumour and whether it has metastasised to nearby lymph nodes or other areas of the body. Early detection remains a major challenge, as cancer is often asymptomatic in early stages of the disease.[7,8] Suspicion is typically raised either by symptoms in advanced stages, or anomalies in routine physical examinations and lab tests or screening programs.[9]

Physical examination and palpation Invasive cancers are notoriously stiff compared to benign tissue. Physicians assess nodular firmness by palpation, a technique with a long history in medicine. Palpation is widely used, and is often the first physical examination. Nevertheless, its subjective nature inherently leads to large inter-observer variability.[11] Moreover, the physician can only examine areas that are accessible and palpable, such as superficial breast nodules or the posterior surface of the prostate.

Laboratory tests High or low levels of certain substances in the body can be a sign of cancer. Analysis of blood, urine, or other body fluids in a laboratory can reveal these substances and hence aid the diagnosis. Examples of blood tests include assessment of specific immunoglobulin (antibodies that help the body fight infections) levels for anomalies,[12] or particular tumour markers such as Cancer Antigen 15-3 (breast cancer), Alpha-Fetoprotein (liver cancer) and Prostate-Specific Antigen (prostatic cancer). The nature of these tests makes them attractive candidates for screening, or as a first diagnostic assessment after physical examination. However, abnormal lab results may be due to other reasons than cancer (poor specificity) and the use of some tumour marker tests remains controversial.

Patient stratification based on PSA in prostate cancer

For prostate cancer, patient stratification is currently based on PSA (prostate specific antigen) blood testing and digital rectal examination by palpation. The PSA is an enzyme secreted by the prostate gland. After the discovery that the PSA concentration in the serum of men with prostate cancer is often elevated, the PSA level has been adopted on a large scale as a marker for prostate cancer. Besides the PSA level, additional diagnostic information can be obtained by monitoring the evolution of the PSA level over time, e.g. by the PSA velocity.

Yet, elevated PSA levels can also be caused by other factors, such as benign prostatic hyperplasia (BPH) and infections (prostatitis). As a consequence, the PSA test suffers from a poor positive predictive value (as low as 30% when using the commonly used threshold of 4.0 ng/ml),[10] and prostate cancer diagnosis hence requires confirmation by biopsy.

Imaging Diagnostic imaging plays a critical role in cancer care, being a fundamental asset for timely cancer diagnosis, disease staging and management as well as for treatment choice, planning, guidance, and follow up. A comprehensive overview of today's main cancer imaging techniques is given in Sec. 1.3.

Biopsy Conclusive diagnosis is generally obtained using biopsy: the extraction and examination of tissue samples. The samples are microscopically graded to assess cancer type and aggressiveness based on the histopathological degree of cell differentiation, which can be quantified by e.g. the Gleason score.[13] Biopsies are typically taken from suspicious regions, such as a stiff nodule in the breast or an odd mole on the skin.

Sometimes, a biopsy is guided using imaging. During this procedure, a needle is manoeuvred to the location of interest with the help of an imaging technique. An image-guided biopsy can be performed using a fine needle, core, or vacuum-assisted biopsy. Occasionally, surgery may be needed to collect a tissue sample.

Notably, prostate cancer is the only solid tumour that still enforces systematic biopsies across the full gland based on a template. Transrectal ultrasound imaging is merely used to guide the biopsy needle. Despite being the current golden standard, recommended by the European Association of Urology guidelines,[14] initial systematic biopsies miss nearly a quarter of the clinically significant cancers,[15] requiring additional biopsy sessions in case of suspicion.

1.2b Treatment

The classic modalities of cancer treatment are surgery, radiotherapy, chemotherapy and endocrine (hormone) therapy. These therapies are old but take a pivotal role in this process, with their combined use accounting for most of cured cases.[16] Therapies can be local and systemic, where the former aims to prevent local recurrence of the cancer, and the latter involves therapy for distant metastasised cancer cells.

Surgery Surgery is most effective when treating localized primary tumour and associated regional lymphatics. Most procedures today are performed through modern minimally-invasive laparoscopic or robotic-assisted interventions, which significantly reduce haemorrhaging and hospitalization time compared to traditional open surgery. In prostate cancer, radical prostatectomy provides effective tumour control when cancer is confined to the organ. For patients with cancer extending beyond the capsule (indicated by positive surgical margins after prostatectomy[17]), the risk of local treatment failure varies from 10 to 50%.[18]

After surgery, histopathological assessment of the resected specimens can be used to decide on possible follow-up treatment, thereby considering aspects such as aggressiveness and positive surgical margins.

Drugs For almost a century, systemic therapy of cancer has been dominated by the use of cytotoxic chemotherapeutics,[16] known as chemotherapy. These drugs are designed to destroy or inhibit rapidly dividing cells, thereby arresting cancer growth. The dose of the drug should be appropriately chosen to act effectively against cancer cells, while limiting normal host cell death.[19]

Today many alternatives to these traditional drugs are becoming available, such as immune therapy and targeted therapy. The latter relies on the discovery of new biomarkers, which can serve as targets. A clear success story among these new therapies is the use of trastuzumab in HER2-positive breast cancer. This humanized antibody

effectively targets and acts against the extracellular domain of HER2,[20] a growth factor which has been shown to play an important role in the development and progression of certain aggressive types of breast cancer. A special type of targeted treatment is anti-angiogenic therapy. Rather than targeting tumour cells directly, these drugs are designed to inhibit vascular growth factors (VEGF) that are over expressed in most solid cancers, with the aim of disrupting the cancer's microenvironment and arresting the supply of oxygen and nutrients.[21]

Radiation therapy Approximately 50% of all new cancer cases will receive some form (X-rays, electron beams or proton) of radiation therapy (RT) during the course of their treatment.[22] It is often used in combination with chemotherapy and/or surgery, commonly in a post-operative fashion – although occasionally pre- or intra-operative RT is adopted as well. For instance through immediate external irradiation after radical prostatectomy in prostate cancer, which was shown to improve progression-free survival and local tumour control in patients with positive surgical margins who are at high risk of disease progression.[23]

Brachytherapy is a form of radiotherapy where a sealed radiation source is placed inside or next to the area requiring treatment.[24] Consequently, the irradiation affects only a very localized area around the radiation sources, resulting in reduced exposure (and hence less damage) to healthy tissue. Brachytherapy is commonly used as an effective treatment for cervical, prostate, breast, and skin cancer, but can also be used to treat tumours in many other body sites.

Focal treatment in prostate cancer?

One in three men already presents some sign of prostate cancer in his 50s, but actually only a small fraction of these tumours is aggressive and requires radical clinical intervention.

Despite this, the effective use of less invasive focal therapies is hampered by the lack of imaging solutions that enable precise and reliable prostate cancer localization. As a consequence, radical prostatectomy (surgical removal of the entire prostate) is the most common treatment, with serious associated risks for the patient to become impotent and incontinent. Therefore, not only late diagnosis and mortality, but also overtreatment with related high costs and impaired quality of life are large-scale problems associated with state-of-the-art solutions.

Focal treatments Focal therapies are minimally invasive, organ sparing procedures with numerous associated advantages such as reduced side-effects and hospitalization time. Among these therapies, *High-Intensity Focussed Ultrasound* (HIFU) exploits tightly focused ultrasound waves of high intensity (i.e. > 5W/cm²) to selectively ablate cancerous tissue. Coagulation necrosis and cell disruption are the main mechanisms of cell destruction in HIFU, occurring at temperatures above 56°C.[25] In *cryotherapy*, tissue destruction is achieved through freezing. A liquid or gaseous freezing agent (cryogen) is delivered with cryoneedles, and used to reduce the local tissue temperature below -40°C for at least three minutes.[25] During *Interstitial Laser Therapy*, image-guided quarts fibres are used to deliver radiant laser energy to the target tissue, thereby heating it up and causing coagulative necrosis. In *Photodynamic Therapy* (PDT), a photosensitizing agent is administered, after which exposure to a specific wavelength of light initiates

a chemical reaction that drives local production of a high-energy form of oxygen (singlet oxygen). The latter is very reactive towards tissue, and can rapidly lead to cell death[26] via direct cytotoxic effects, damage tot the vasculature and acute induction of an inflammatory reaction that can initiate anti-tumour immunity.[27] *Irreversible electroporation* (IRE) is a soft tissue ablation technique that uses ultra short and very powerful electrical fields to create permanent damage to the cell membrane in the form nanopores. It is generally believed that cell death then occurs through apoptosis, rather than necrosis as in other ablation techniques.[28]

1.3 Modern cancer imaging

As highlighted before, adequate cancer therapy and management relies on suitable diagnostic means; The extent and type of systemic treatment depends on whether cancer has migrated from the primary tumour towards distant sites, such as other organs and lymph nodes; The use of focal therapies dictates knowing the exact location of the tumour; Active surveillance instead of immediate treatment demands highly reliable monitoring of disease progression. In this context, diagnostic imaging is a fundamental asset for timely cancer diagnosis, disease staging and management as well as for treatment choice, planning, guidance, and follow up.

Yet, imaging technologies that currently play a primordial role in this process, i.e. magnetic resonance imaging (MRI), X-ray computed tomography (CT) and nuclear imaging, have important drawbacks; MRI remains an expensive modality with limited accessibility, CT and nuclear imaging induce ionizing radiation and specifically nuclear imaging yields a low spatial resolution. Moreover, in most cases their limited reliability and accuracy still poses the need for invasive verification with biopsies. This section provides an overview of the most relevant cancer imaging techniques, today.

1.3a Nuclear imaging

Cancer cells require a large amount of glucose to have enough energy to grow. Positron Emission Tomography (PET) and Single-Photon Emission Tomography (SPECT) utilize radioactive molecules that are similar to glucose, such as C-choline or fluorodeoxyglucose (F-FDG).[29] After injection, these tracers accumulate within malignant cells because of their high rate of glucose metabolism and the emitted (ionizing) gamma radiation can be imaged[30] using gamma cameras. For prostate cancer, imaging of radioactively-labelled Prostate-Specific Membrane Antigen (PSMA)[31] – a protein that is expressed in all types of prostate tissue, but increased in carcinoma – has recently been introduced.

The limited spatial resolution and adverse effects of radioactive decay in PET and SPECT hamper their use for early cancer imaging, making them more appropriate for whole body staging of metastasis.[32]

1.3b X-ray and computed tomography

X-ray imaging has a long history. It found its way into medicine in 1896, only 3 months after Röntgen's first announcement. Its initial use was to reveal bone fractures. Since

then, X-ray imaging advanced significantly. Today, computed tomography – a computerized reconstruction method that exploits X-ray illumination from multiple angles to produce 2 or 3 dimensional images[33] – has been adopted in applications ranging from breast to kidney cancer imaging.

However, like the gamma radiation that originates from radioactive decay, X-radiation is ionizing. Whilst it should be noted that the clinical gains of imaging are typically worth the risk, X-rays are known for their ability to induce DNA mutations. These could ultimately lead to the development of cancer. Hence, there is a strong trend towards X-ray solutions that use increasingly reduced doses.[37] Yet, there is no compelling evidence to indicate a dose threshold below which the risk of tumour induction is zero.[38]

Mammography in breast cancer

The golden standard for early detection of breast cancer is X-ray mammography; a fast and efficient procedure that enables scanning for dense masses and is incorporated into cancer screening programs around the world.[34] A mammogram provides the clinician with a two-dimensional projection of tissue-induced X-ray attenuation. Dense, highly attenuating structures such as tumours appear bright, whereas fatty tissues appear dark.

Nevertheless, current mammography has several drawbacks. First of all, the procedure involves a strong physical compression to squeeze the breast between the emitter and detector plates, and is commonly found unpleasant. Secondly, the illuminating radiation is ionizing.[35] Thirdly, mammograms often yield insufficient specificity to reliably designate bright anomalies as malignant or benign, especially when the breast is generally denser. Approximately 25% of women have dense breasts, and this condition is more likely to occur in younger women, who have a predominance of dense glandular tissue.[36]

A positive mammogram therefore requires additional testing to confirm the presence of cancer through e.g. an MRI or ultrasound exam, and invasive biopsy.

1.3c Magnetic resonance imaging

Magnetic resonance imaging (MRI) exploits the relation between tissue composition and the relaxation behaviour of hydrogen protons therein. After the application of an electromagnetic radiofrequency pulse, various relaxation properties can be investigated, of which the most straightforward ones are the longitudinal (T1) and transverse (T2) relaxation times.[39] It should be noted that performing image-guided or targeted biopsy with MRI is not trivial, as metals are incompatible with the strong magnetic field of the scanner. Hence, MRI imaging is often fused with ultrasound, either cognitively or through dedicated registration algorithms.[40]

T1 and T2-weighted imaging The local T1 and T2 relaxation times are dominantly affected by the size and motion of the molecules on which the hydrogen nuclei reside. Small, rapidly rotating molecules with poor spin-lattice energy exchange,[41] like free water, require more time to recover the original magnetization vector, and hence have relatively long T1 relaxation times. As for T1, the T2 characteristics are strongly determined by molecular rotation speeds. T2 relaxation is a consequence of the gradual de-phasing of transversal magnetization resulting from variance in the precession frequencies. Abundance of water leads to reduced de-phasing rates, and hence long T2 times. These properties make imaging T1 and (in particular) T2 times in the context of cancer localization notably useful,

as pathologies often manifests through an increase in water content (e.g. oedema, infarction, infection), and cancer is no exception.

Diffusion-weighted imaging Diffusion-weighted imaging assesses the extent of thermally-driven molecular water diffusion in tissue, which is highly influenced by its cellular environment *in-vivo*; cellular packing, intracellular elements, membranes, and macromolecules impede this process.[42] The high cellular density in most tumours is thought to constrain water diffusion, thereby causing the apparent diffusion coefficient to be lower than in benign tissue.

Spectroscopy Magnetic resonance spectroscopy exploits the fact that protons in different molecules resonate at slightly different frequencies.[43] Distinct metabolites exhibit characteristic chemical shifts in resonance frequency, thereby allowing the characterization of the metabolic changes associated with cancer through spectroscopy.[44] Among these, elevation of choline levels is associated with many malignant tumours, including prostate cancer.[45] The spatial resolution of magnetic resonance spectroscopy is low however (≈ 5 mm), impairing accurate tumour localisation.

Limited success of imaging in prostate cancer

MRI is believed to provide the most promising imaging markers for prostate cancer. Nevertheless, its clinical value and role is still debated,[46,47] and the anticipated disruptive innovation that should steer the paradigm of prostate cancer diagnosis away from blind systematic biopsies is unfortunately still lacking.

From the perspective of the urologists, integrating MRI into their workflow indeed poses various challenges. Most urologists are not trained to interpret MRI scans; the technology to fuse MRI scans with real-time ultrasound is expensive and involves a learning curve, and the patient must still be referred out for an MRI. "A portable ultrasound-based imaging device that would accurately distinguish between a prostate cancer tumour and healthy tissue would be a sort of Holy Grail for urologists".[48]

Dynamic contrast enhancement Dynamic contrast-enhanced (DCE)-MRI requires the injection of an intravenous bolus of gadolinium contrast agent, followed by the acquisition of a sequence of images while the contrast agent enters the vascular bed of the organ of interest.[49] Gadolinium ions are paramagnetic and interact with nearby hydrogen nuclei to shorten the T1 relaxation time of water in the local tissue, thereby increasing signal intensity on T1-weighted images. The degree of enhancement reflects physiological factors, including tissue perfusion and capillary surface area, but also capillary permeability. The latter is typically high in leaky angiogenic tumour vessels. Several DCE-MRI parameters can be extracted that aim at quantifying these cancer-related changes in microvascular physiology.[50]

Multiparametric MRI Although all these sequences have diagnostic value, individual MRI markers are on their own often not sufficient for reliable clinical diagnostics. This has led to the introduction of multi-parametric (mp)MRI, in which the rich but

complex toolset provided by MRI is exploited by devising diagnostic protocols that combine multiple MRI parameters.[51,52] Widespread introduction of mpMRI is however hampered by the limited availability of equipment, high costs, and complex workflow. Moreover, the clinical value of mpMRI is not established yet.[46,47]

1.3d Ultrasound imaging

In ultrasound (US) imaging, high-frequency acoustic pulses are transmitted into tissue by a transducer, after which their pulse-echoes originating from inhomogeneities in the medium (e.g. tissue interfaces) are used to derive various properties such as echo intensity. US has the remarkable potential to shine as a non-ionizing and cost-effective technique that can limit the diagnostic burden on the healthcare system and the patient via an effective and accurate imaging protocol. Below are some of the most important US modalities.

B(rightness)-mode Standard B-mode (or greyscale) imaging visualizes the beam-formed envelopes of the echoes to form an image in which the pixel values represent the echo intensities at that position in the field of view. As these echoes are particularly strong at the discontinuities in acoustic properties (impedance) of the medium, B-mode US gives insight into anatomical structure, and can indicate anomalies such as cysts or solid masses. B-mode breast US was shown to provide a more accurate diagnosis for pathologies than X-ray mammography in young subjects with dense breasts.[53]

Doppler Doppler sonography allows functional blood flow imaging by detecting the US Doppler shifts induced by the transport of blood-cells. The two dominant modes in cancer diagnosis are termed "colour Doppler" and "power Doppler". Where the former measures the mean frequency shift (and hence mean velocity), power Doppler integrates the entire Doppler spectrum, yielding increased sensitivity to blood perfusion.[54] Using Doppler US, Yang *et al.* showed that malignant axillary lymph nodes display significantly higher peripheral flow in 135 women with primary breast cancer.[55]

Elastography Cancer is stiff compared to benign tissue, which is why physicians assess nodular firmness by palpation. Today, tissue stiffness can more objectively be evaluated using US elastography. By palpating tissue using the US probe and consequently tracking the resulting echo displacements over time, tissue strain can be measured and displayed as a measure of elasticity. The applied stress can be imposed mechanically or via acoustic radiation force. A fully quantitative measure of lesion stiffness can be obtained by shear wave elastography (SWE), a method that uses a high-intensity acoustical push pulse to produce laterally propagating shear waves that can be tracked to obtain the shear velocity, which is in turn related to the Young's modulus. In,[56] SWE and standard grey-scale imaging were used to differentiate benign from malignant solid breast masses, yielding an accuracy of 86% for the detection of malignancy.

Dynamic contrast enhancement (DCE-US) In Dynamic Contrast Enhanced Ultrasound (DCE-US), the passage of an intravenously injected cloud of ultrasound contrast agents through an organ is recorded with an ultrasound imaging system.[57] The adopted contrast agents, lipid-shelled inert gas bubbles with a size similar to red blood cells (1-10 μm), remain intravascular while reaching the smallest capillaries in the vascular net. In the context of tumour detection, a particularly interesting application of DCE-US concerns the localization of neo-angiogenic vascularization associated with tumour growth and metastasis,[58],[59],[60] and with lethal phenotypes.[61] Where DCE-MRI is mainly used to assess microvascular permeability, DCE-US is typically used to analyse perfusion. To this end, clinicians mainly rely on qualitative inspection of the ultrasound videos,[62] searching for visual clues such as early contrast enhancement.

1.4 (Ultrasound) Markers for cancer

Several cancer tissue markers, common to most solid, angiogenic tumours, have been considered to differentiate cancer from benign tissue. For prostate cancer, markers suitable for tumour localization using imaging are mainly based on MRI and ultrasound. Below we summarize some of the most relevant markers.

1.4a Tissue structure

Cancer aggressiveness and risk of developing metastasis is reflected by the degree of cell differentiation, graded invasively trough histopathological examination of tissue. For prostate cancer, it is quantified by the Gleason score.

Diagnostic means US texture and spectral analysis can possibly capture some cancer-related changes in tissue structure. This idea has resulted in different system implementations such as C-TRUS (computerized transrectal US)[63] and Histoscanning™[64] for prostate cancer and a method for distinguishing benign and malignant breast tumours[65] based on texture and shape.

Limitations To date there is no *in-vivo* imaging method that can accurately quantify the degree of cell differentiation in deep tissue. One of the most promising US-based methods of the last decade, Histoscanning™, showed disappointingly low sensitivity (45%) and positive predictive value (19%) in recent clinical studies on prostate cancer detection.[66]

1.4b Angiogenesis

At the vascular level the impact of cancer is striking. Cancer vasculature is highly chaotic, characterized by increased microvascular density and tortuosity, as well as by the presence of irregular branching and arteriovenous shunts. The process that governs these vascular alterations is angiogenesis,[67] a biomarker that is strongly associated with lethal cancer phenotypes.[58]

Diagnostic means Many imaging techniques look for an increase in perfusion as a marker for cancer angiogenesis. Blood flowing through the macrovasculature at relatively high velocities can be imaged using colour- and power Doppler US. However, cancer angiogenesis is mainly characterized by a dominant increase in the number of microvessels (often only 10-50μm in diameter), limiting the effectiveness of Doppler US.[68] To assess microvascular perfusion, DCE-US videos can be inspected for visual clues such as early, rapid and increased contrast enhancement.[69] For prostate cancer detection, a meta-analysis of 16 studies with 2624 patients yielded a pooled sensitivity and specificity of 70% and 74%, respectively.[70]

Limitations While visual assessment of perfusion through DCE-US is promising, it qualitative nature hampers standardization and implies a steep learning curve. A logical step is translation towards robust, accurate and objective methods that are able to quantify the degree of disorganization in the microvascular architecture, preferably based on a cheap and accessible imaging modality. In recent years, several quantitative DCE-US methods have been proposed to fulfil exactly this demand. These approaches either aim to quantify perfusion-related aspects of the vasculature, or alternatively dispersion (spreading) of the adopted contrast-agent through the complex multi-path trajectories in this vascular net. The latter, termed contrast-ultrasound dispersion imaging,[71,72] has shown great promise among small groups of patients,[72] but has not reached clinical implementation.

1.4c Tissue mechanics

Along with these vascular features, cancer tissue exhibits a specific set of mechanical characteristics. First of all, cancers are stiff compared to benign tissue. Physicians assess nodular firmness by palpation, a subjective technique with a long history in medicine. However, not only elasticity, but also viscosity is a parameter of diagnostic value for detection and characterization of malignant lesions.

Diagnostic means A quantitative option to assess tissue stiffness is provided by ultrasound shear wave elastography. This method uses an acoustic radiation force to produce laterally propagating shear waves that can be tracked to obtain the speed, which in turn is related to the Young's modulus.

Limitations Not only elasticity, but also viscosity plays an important role in the propagation process of shear waves. In fact, viscosity itself is a parameter of diagnostic value for detection and characterization of malignant lesions. However, to date no imaging solution has been proposed for cancer localization by imaging viscosity, and is mostly limited by the need for quantification with high spatial resolution.

1.4d Interstitial fluid

Interstitial fluid is restricted by its cellular environment, governed by factors such as cellular packing, intracellular elements, membranes, and macromolecules. In cancer, the amount of fluid is typically greatly increased, poorly drained and highly restricted.[73]

Diagnostic means The amount of interstitial water can be assessed by quantifying the diffusion of water molecules using diffusion-weighted MRI.

Limitations Robust and accurate methods based on a cheap and widely accessible imaging modality such as US. The link between fluid content and nonlinear US behaviour[74] motivates towards the estimation of a marker that is able to quantify the nonlinear nature of US propagation.[75] To this end, several strategies to estimate the "coefficient of nonlinearity" have been proposed.[76] Yet, major fundamental drawbacks such as the need for a special transducer[77] or the dependency of the estimates on the distribution of scatterers and the resulting speckle pattern[78] hamper their applicability for clinical cancer imaging.

1.5 Scope of this dissertation

Effective cancer management requires adequate diagnostic means. Imaging plays a central role in this process. As described in Sec. 1.4, several cancer markers can be considered for this purpose. Yet, imaging of these markers is often not straightforward and has several limitations.

One essential limitation is that the most promising approaches are largely based on highly expensive MRI. The growing burden of healthcare costs on our society motivates the use of sustainable modalities. While a pivotal role of ultrasound would represent an excellent cost-effective and widely accessible alternative, the accuracy of ultrasound-based methods typically falls behind those of novel multi-parametric MRI strategies.

Hence, the ultimate goal is to advance and extend ultrasound imaging to such a level that it allows accurate cancer diagnosis based on ultrasound alone, providing timely and accurate assessment of both tumour location and aggressiveness. To achieve this, ultrasound imaging should be exploited to its full potential.

This dissertation aims to pave the way in this direction, by introducing new signal-processing methods for a variety of ultrasound imaging modalities. We will build upon those characteristics that are typical for cancer and will address several of the limitations listed in Sec. 1.4 by providing an ultrasound imaging solution through novel and dedicated signal processing methods.

In the first part of this thesis, new methods based on dynamic contrast-enhanced ultrasound (DCE-US) that aim at describing the peculiar *vascular* structure originating from cancer-driven angiogenesis are proposed. These approaches will extend beyond standard perfusion imaging, and assess new macroscopic features and reveal microscopic characteristics.

The second part of this dissertation will describe new methods to quantify two particular aspects of cancerous *tissue*: Viscoelastic behaviour and nonlinear propagation of ultrasound.

Throughout several chapters, clinical *in-vivo* imaging data obtained from patients with prostate cancer will be used as a representative test-case for the proposed methods. All human studies conducted in the present work were approved by the local ethics committees of the involved hospitals, and written informed-consent was obtained from the patients.

1.6 Outline

This thesis is subdivided into two parts, which address challenges related to the detection of cancer markers in two distinct categories: *Part I: vascular markers* and *Part II: tissue markers*.

Part I The first chapter (2) of *Part I* takes a macroscopic perspective, and describes a method that can adequately quantify the kinetics exhibited by ultrasound contrast agents when transported through the vascular net. The method was tested on a clinically acquired DCE-US dataset of 25 patients with biopsy-proven prostate cancer, referred for radical prostatectomy. This chapter has been published as [J-10]. In Chapter 3, we remain at a macroscopic level, and exploit DCE-US in combination with a new US vector velocity imaging method to quantify blood flow fields and in particular flow heterogeneity. The latter was adopted as a marker for angiogenesis, and used to predict the presence of prostate cancer among 24 patients. This chapter has been published as [J-9].

At a smaller scale, we aim at evaluating features of the vascular net directly. In Chapter 4, we introduce contrast-enhanced ultrasound tractography, setting a basis for characterization of microbubble trajectories. We show that the proposed approach can directly be applied to clinically acquired 4D DCE-US datasets, and a proof-of-concept is given on data obtained from 3 patients referred for radical prostatectomy. Comparison with histopathology after prostate resection revealed higher densities and more tortuous geometries in malignant areas. This chapter has been submitted for publication as [J-1] Then, in Chapter 5, we move to an even smaller scale, and employ dedicated sparse recovery techniques to generate a super-resolution ultrasound image of the vasculature using a clinical DCE-US dataset, revealing features that were previously obscured by the physical diffraction limit. These developments open up additional opportunities for vascular characterization. This chapter has been published as [C-2]

The above described methods rely on accurate detection and quantification of microbubbles. Yet, commercial DCE-US imaging modes are not completely specific to microbubbles, leading to several artefacts. In this context, we investigate the use of a microbubble-specific marker for DCE-US, a cumulative phase-shift between the second harmonic and fundamental of the ultrasound wave. A proof-of-concept aimed at quantification of microbubbles in a tomographic fashion is presented in Chapter 6, displaying the potential of this new technique. This chapter has been published as [J-11], and is a follow-up of [J-12].

Part II Moving on to *Part II: tissue markers*, we start by proposing a new method to assess tissue viscoelasticity through US shear wave elasticity imaging (Chapter 7). We perform dedicated *in-vitro* studies to demonstrate the ability of the approach to provide high resolution viscosity maps, opening up a way for imaging this marker in the context of cancer diagnostics. This chapter has been published as [J-5].

The established link between cancer, fluid content and the nonlinear behaviour of US motivates towards the estimation of a marker that is able to quantify the nonlinear nature of US propagation. In Chapter 8 we set the theoretical basis for a new method to image the acoustical coefficient of nonlinearity in tissue. Specifically designed *in-silico* and *in-vitro* studies are used to provide a proof-of-principle. This chapter has been published as [J-14].

Conclusions and possible future research directions are discussed in the final part of this thesis. Chapter 9 provides the author's view on what the role of advanced US in future breast cancer diagnosis could be, and in particular an outlook for its position along today's mammography. This editorial has been published as [J-8] Finally, in Chapter 10, a critical discussion of the work presented in this dissertation is given, and general conclusions are drawn.

Part I

Vascular Markers

2

Ultrasound-Contrast-Agent Dispersion and Velocity imaging

Abstract - *Prostate cancer (PCa) is the second-leading cause of cancer death in men; however, reliable tools for detection and localization are still lacking. Dynamic Contrast Enhanced Ultrasound (DCE-US) is a diagnostic tool that is suitable for analysis of vascularization, by imaging an intravenously injected microbubble bolus. The localization of angiogenic vascularization associated with the development of tumours is of particular interest. Recently, methods for the analysis of the bolus convective dispersion process have shown promise to localize angiogenesis. However, independent estimation of dispersion was not possible due to the ambiguity between convection and dispersion. Therefore, in this study we propose a new method that considers the vascular network as a dynamic linear system, whose impulse response can be locally identified. To this end, model-based parameter estimation is employed, that permits extraction of the apparent dispersion coefficient (D), velocity (v), and Péclet number (Pe) of the system. Clinical evaluation using data recorded from 25 patients shows that the proposed method can be applied effectively to DCE-US, and is able to locally characterize the hemodynamics, yielding promising results (receiver-operating-characteristic curve area of 0.84) for prostate cancer localization.*

From: R.J.G. van Sloun, L. Demi, A.W. Postema, J.J.M.C.H. de la Rosette, H. Wijkstra, and M. Mischi,"Ultrasound-contrast-agent dispersion and velocity imaging for prostate cancer localization", *Medical Image Analysis*, vol. 35: pp. 610-619, ©Elsevier, 2016

2.1 Introduction

Prostate cancer (PCa) is the most frequently diagnosed cancer in men aside from skin cancer, and the second-leading cause of cancer death in men.[79] Given the significant risk of serious side effects associated with PCa treatment (radical prostatectomy), careful observation (termed active surveillance) instead of immediate treatment is appropriate for many patients that have less aggressive tumours. This approach requires accurate and reliable monitoring techniques. When treatment is necessary, minimally invasive methods such as focal therapy may limit side effects, which in turn requires accurate tumour localization. The current golden standard for prostate cancer diagnosis is transrectal systematic needle biopsies. However, initial biopsies miss nearly a quarter of the clinically significant cancers,[15] and provide little information regarding exact tumour locations. Moreover, being an invasive technique, it carries significant risk of infection. This requires hospitalization in up to 6% of the cases,[80] becoming even more alarming with increasing resistance to antibiotics. Although transperineal biopsy is emerging as a way to reduce this risk, it is a more complex procedure that requires high grade anaesthesia.[81]

Dynamic Contrast Enhanced Ultrasound (DCE-US) is a minimally invasive diagnostic tool that allows analysis of vascularization, by imaging an intravenously injected microbubble bolus. Of particular interest is the localization of neo-angiogenic vascularization associated with tumour growth and metastasis,[58][59],[60]. In this paper, we aim at characterizing the microvasculature from the obtained indicator-dilution curves (IDCs) using DCE-US; each IDC represents the evolution over time of the ultrasound contrast agent (UCA) concentration in a pixel.

The microvascular structure that originates from tumour driven angiogenic growth is characterized by high microvascular density (MVD), small-diameter vessels that are highly tortuous, chaotic, irregular and have shunts. Ineffective blood flow can lead to hypoxia and deteriorated endothelial wall cells, potentially resulting in extra-vascular leakage and tumour metastases. With the aim of detecting angiogenic microvascularization, DCE-US imaging of hemodynamic features relies on the hypothesis that these features reflect changes in microvasculature associated with angiogenesis. Focusing at increased MVD, time-intensity features related to microvascular perfusion have been studied by several researchers.[82–84] However, ultrasound attenuation and scanner settings affect the estimation of local UCA concentration and the resulting amplitude based perfusion parameters. Moreover, increased tortuosity as well as increased flow resistance due to decreasing functional vascular cross-sectional area in neoplastic tissue cause lower tumour perfusion,[85] leading to perfusion heterogeneity and making localization of angiogenesis based on perfusion a challenging task. Related to this, intratumour vascular heterogeneity has been assessed,[86] although using DCE-CT instead of DCE-US. To enhance the sensitivity of perfusion imaging, regularized deconvolution of the perfused tissue signals with the feeding-artery signal (referred to as arterial input function) is investigated for DCE-CT and DCE-MRI in.[87]

Alternatively, features linked to UCA bolus dispersion have been proposed,[71,72] and are instead intended to directly reflect the tortuous and chaotic structure of the tumour vasculature. Although these approaches have shown promise, independent estimation of dispersion and velocity was not possible due to the ambiguity between

dispersive and convective processes reflected in the measured IDCs. Hence, so far only dispersion related parameters that represent a combination of dispersion and velocity were obtained, leaving the specific contribution of both components to the flow kinetics unassessed. Furthermore, to achieve a local estimate of the contrast kinetics, a specific spatial UCA bolus concentration profile was assumed.

Instead of modelling the individual measured IDCs, *we consider the vascular network as a dynamic linear system or channel, whose impulse response can be locally identified by input-output analysis of IDCs*. For this purpose, a Wiener filter is determined, providing an optimal (minimum mean squared error) estimation of the system impulse response. The extraction of the dispersion coefficient, velocity and Péclet number is then facilitated by employing model-based parameter estimation by least squares and maximum likelihood approaches.

The analytical details of the measurement model are given in Sec. 2.2a, and an estimator for the Wiener filter is derived in Secs. 2.2b and 2.2c. Sec. 2.2d provides a model-based parameter estimator based on Least Squares minimization. Alternatively, Maximum Likelihood estimators are derived in Sec. 2.2e. The data acquisition protocol and the validation methodology are reported in Secs. 2.3 and 2.4, respectively. The method is then clinically evaluated using a dataset consisting of 61 DCE-US planes, recorded transrectally from 25 patients. A qualitative as well as a quantitative analysis is performed, and the effectiveness of Least Squares and Maximum Likelihood parameter estimators is compared in Sec. 2.5. Finally, in Sec. 2.6, the results are discussed and conclusions derived.

2.2 Materials and methods

2.2a Measurement model

We consider a ring shaped kernel with an inner and outer radius of 1 mm and 1.5 mm, respectively, as shown in Figure 2.1. The dimensions of the kernel were selected based on the speckle-grain size[88] and the scale at which early angiogenesis occurs[59]. The kernel should be larger than the system resolution and smaller than the scale at which angiogenesis develops. With the ultrasound system's axial resolution being approximately 0.3 mm, and the lateral resolution being approximately 0.5 mm at 5 cm from the probe, the inner radius of the kernel was set to 1 mm. Angiogenesis is required for tumours to grow beyond 2-3 mm in diameter. Although the resolution is not adequate for imaging single microvessels, it is sufficient to appreciate changes in the macroscopic hemodynamic phenomena related to early angiogenesis. The adopted kernel is used as follows. The centre-pixel IDC is considered to be the local channel input, and the IDCs of the pixels in the kernel are the possible outputs of the channel. Here we assume that there are physically causal relations between the centre-pixel IDC and those in the kernel pixels. Firstly, the channel impulse responses from the input to the outputs are estimated. Then, all non-causal responses are discarded (those where the output anticipates the input), after which a mean causal impulse response is obtained.

To accomplish this, we model the IDC of the i^{th} pixel within the kernel $\vec{d}_i \in \mathbb{R}^N$ as a filtered version of the IDC of the pixel at the centre $\vec{x} \in \mathbb{R}^N$. Minimizing the mean squared

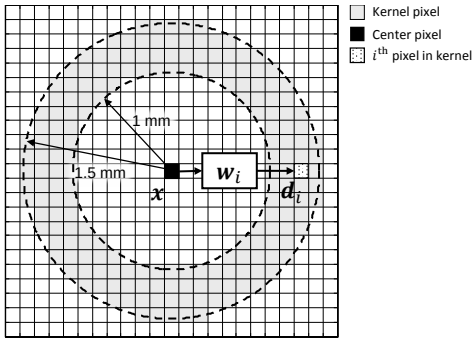

Figure 2.1: Kernel for impulse response estimation, showing the Wiener system model $\vec{w}_i$ between the indicator dilution curve at the centre pixel and the i^{th} pixel within the kernel.

error between the desired output $d_i[n]$ and the filtered input $\sum_{m=0}^{n-1} w_i[m]x[n-m]$, the optimal Wiener filter coefficients $\vec{w}_i$ are given by the Wiener-Hopf equations:[89]

$$\vec{r}_{d_i x} = \mathrm{R}_x \vec{w}_i, \tag{2.1}$$

where $\vec{r}_{d_i x}$ denotes the cross correlation vector between $\vec{d}_i$ and $\vec{x}$ and R_x is the autocorrelation matrix of $\vec{x}$. In practice, ultrasonic IDC measurements are corrupted by multiplicative (*e.g.* speckle) as well as additive (*e.g.* thermal, electronic) noise. We first analyse their effects on the Wiener estimate, and consider noisy observations

$$\tilde{\vec{x}} = u_1 \vec{x} + v_1, \tag{2.2}$$

$$\tilde{\vec{d}}_i = u_2 \vec{d}_i + v_2, \tag{2.3}$$

with v_1, v_2 being independent and identically distributed (i.i.d.) white $\mathcal{N}(0, \sigma_v^2)$ and u_1, u_2 following i.i.d. Rayleigh distributions with scale parameter σ_u, being mutually independent and independent of the signal components. The local assumption on equal noise variances of u_1 and u_2 is reasonable given the small kernel size. A Rayleigh distribution was chosen because it captures the effects of fully developed speckle noise in ultrasound[90]. The measured cross correlation vector is then given by

$$\vec{r}_{\tilde{d}_i \tilde{x}} = \mathrm{E}[u_1]\,\mathrm{E}[u_2]\,\vec{r}_{d_i x} = \frac{\pi}{2}\sigma_u^2 \vec{r}_{d_i x}, \tag{2.4}$$

where $\mathrm{E}[\cdot]$ denotes the expectation. Similarly, the measured autocorrelation matrix of $\tilde{\vec{x}}$ can be derived as

$$\mathrm{R}_{\tilde{x}} = \mathrm{R}_{u_1} \mathrm{R}_x + \sigma_v^2 \mathrm{I}, \tag{2.5}$$

where R_{u_1} is the autocorrelation matrix of the multiplicative noise component and I denotes the identity matrix. Assuming a white Rayleigh distribution, we have the following autocorrelation function:

$$\vec{r}_{u_1}(\tau) = \delta(\tau) \int_0^\infty u^2 \frac{u}{\sigma_u^2} \exp\left(-\frac{u^2}{2\sigma_u^2}\right) du = 2\sigma_u^2 \delta(\tau), \tag{2.6}$$

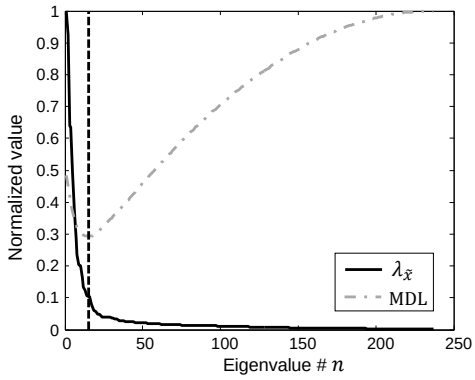

Figure 2.2: Eigenvalues $\lambda_{\tilde{x}}$ as well as the Minimum Description Length (MDL) criterion for an example sample-autocorrelation matrix. The value of n that minimizes the MDL is indicated by the dashed vertical line, here being 16.

where $\delta(\tau)$ is the Dirac delta function, for which we obtain

$$\mathrm{R}_{u_1} = 2\sigma_u^2 \mathrm{I}. \tag{2.7}$$

2.2b Estimation of auto- and cross-correlation

We proceed by estimating the true signal autocorrelation matrix and cross correlation vector from the measured data. The latter can directly be estimated from (2.4) as:

$$\hat{\vec{r}}_{d_i x} = \frac{2}{\pi} \frac{\vec{r}_{\tilde{d}_i \tilde{x}}}{\sigma_u^2}. \tag{2.8}$$

Estimating the autocorrelation matrix R_x is less trivial. With the aim of separating the signal and noise subspaces, we first perform an eigendecomposition on (2.5), yielding

$$\mathrm{R}_{\tilde{x}} = \begin{bmatrix} \mathrm{U}_x & \mathrm{U}_v \end{bmatrix} \begin{bmatrix} 2\sigma_u^2 \Lambda_x + \sigma_v^2 & 0 \\ 0 & \sigma_v^2 \end{bmatrix} \begin{bmatrix} \mathrm{U}_x^H \\ \mathrm{U}_v^H \end{bmatrix}, \tag{2.9}$$

where Λ_x is a diagonal matrix whose elements are the corresponding signal eigenvalues, *i.e.* $\Lambda_x(n,n) = \lambda_x(n)$, arranged in descending order. U_x and U_v denote the signal and noise subspaces, respectively. From (2.9), the signal subspace can readily be obtained by simply observing the eigenvalues $\lambda_{\tilde{x}}(n)$. However, this approach assumes $\mathrm{R}_{\tilde{x}}$ to be estimated from an infinite sample size. In practice, the number of observations is limited, and $\mathrm{R}_{\tilde{x}}$ is estimated by the sample-autocorrelation matrix, with noise eigenvalues that are all different. Hence, (2.9) does not hold and estimation of the signal subspace becomes more challenging.

To overcome this problem, we regard the subspace detection to be a model selection problem. Given the observations that are used to acquire the sample-autocorrelation matrix, along with a set of models parametrized by n signal eigenvalues and n eigenvectors in addition to a noise variance, we select the model that best fits the observations. Adopting the approach developed in[91], the Minimum Description Length (MDL) describes a trade-off between the log-likelihood of the maximum likelihood estimator of the model parameters (*i.e.* the sample eigenvalues and eigenvectors) and a term

promoting a low number of free parameters:

$$\mathrm{MDL}(n) = -\log\left[\frac{\prod_{l=n+1}^{N}(\lambda_{\tilde{x}}(l))^{\frac{1}{N-n}}}{\frac{1}{N-n}\sum_{l=n+1}^{N}\lambda_{\tilde{x}}(l)}\right]^{(N-n)M} + \frac{1}{2}n(2N-n)\log M, \tag{2.10}$$

where $\lambda_{\tilde{x}}(l)$ is the l^{th} eigenvalue of the sample-autocorrelation matrix $R_{\tilde{x}}$ and M is the number of samples used to compute $R_{\tilde{x}}$. The dimension of the signal subspace $\hat{n}$ is then determined as the value of n that minimizes the MDL. This procedure is exemplified in Figure 2.2. From this, an estimate of R_x can be obtained as:

$$\hat{\mathrm{R}}_x = \frac{1}{2\sigma_u^2}\hat{\mathrm{U}}_x[\hat{\Lambda}_x - \sigma_v^2]\hat{\mathrm{U}}_x^H, \tag{2.11}$$

where $\hat{\Lambda}_x$ and $\hat{\mathrm{U}}_x$ are the estimated signal eigenvalues and eigenvectors, respectively. To enable computation of the Wiener coefficients $\vec{w}_i$, an estimate of R_x^{-1} is also given. Since matrix inversion can be unstable and prone to noise amplification, we employ a strategy based on eigenvalue regularization. Given the measured eigenvalues, $\lambda_{\tilde{x}}(n)$, the regularized eigenvalues are given by:

$$\hat{\lambda}_x(n) = \begin{cases}\lambda_{\tilde{x}}(n) & \text{if } n \le \hat{n} \\ \lambda_{\tilde{x}}(\hat{n}+1) & \text{otherwise}\end{cases}, \tag{2.12}$$

after which inversion of the autocorrelation matrix is achieved by inverting the regularized eigenvalues:

$$\hat{\mathrm{R}}_x^{-1} = 2\sigma_u^2\mathrm{U}_{\tilde{x}}\begin{bmatrix}1/\hat{\lambda}_x(1) & 0 & 0\\ 0 & \ddots & 0\\ 0 & 0 & 1/\hat{\lambda}_x(N)\end{bmatrix}\mathrm{U}_{\tilde{x}}^H. \tag{2.13}$$

2.2c Wiener filter

Next, we combine Equations (2.1), (2.8), and (2.13) to obtain an estimate of the Wiener filter coefficients

$$\hat{\vec{w}}_i = \hat{\mathrm{R}}_x^{-1}\hat{\vec{r}}_{d_i x}, \tag{2.14}$$

describing the channel from $\vec{x}$ to $\vec{d}_i$. Note that the noise variance, σ_u^2, cancels out (see Equations (2.8) and (2.13)). Using this, the mean causal impulse response $\bar{\vec{w}}$ is calculated by averaging the obtained coefficients over all kernel IDC's $\vec{d}_i$ that show a causal relation with respect to the centre IDC $\vec{x}$:

$$\bar{\vec{w}} = \frac{1}{|S_c|}\sum_{i\in S_c}\hat{\vec{w}}_i, \tag{2.15}$$

where S_c denotes the set of causal impulse responses, and $|S_c|$ is the number of causal impulse responses. Causality between an IDC in the kernel ring and the IDC at the

centre pixel is assumed if the peak time of the cross correlation vector $\hat{\vec{r}}_{d_i x}$ is positive.

2.2d Least Squares parameter estimation

To provide a parameter-based characterization of the estimated mean Wiener channel, we take a macroscopic view of the vascular network by regarding the flow through all the multi-path trajectories similar to the flow through porous media.[92] In line with this, the differential model that we adopt to represent the hemodynamics captured in $\bar{\vec{w}}$, is the one-dimensional convection-diffusion equation[93] with constant diffusion and velocity within the kernel:

$$\partial_t C(z,t) = D\partial_z^2 C(z,t) - v\partial_z C(z,t), \tag{2.16}$$

where $C(z,t)$ is the contrast agents concentration at position z and time t, D is the diffusion coefficient, describing the apparent dispersion of contrast agents through the vascular network and v is the convective velocity. Being closer to the observed macroscopic physical phenomena of UCAs flowing through multi-path vascular trajectories, we will refer to D as the dispersion coefficient rather than the molecular diffusion.[94] From (2.16), our goal is the estimation of v and D. To this end, its Green's function[95,96] can be derived as,

$$g(z,t|v,D) = \frac{H(t)}{\sqrt{4\pi D t}} \exp\left(-\frac{(z-vt)^2}{4Dt}\right), \tag{2.17}$$

where $H(t)$ is the Heaviside step function, and can be curve-fitted to $\bar{\vec{w}}$ using Least Squares (LS) minimization. The position z is approximated by the average radial distance $L = 1.25$ mm of pixels in the ring shaped kernel with respect to the centre pixel. Obeying the conservation of mass, $g(L,t|v,D)/v$ has a temporal integral equal to one. However, if our assumptions on the noise model or the estimation of its power are not entirely correct (*e.g.* unequal noise variances of u_1 and u_2), the amplitude of the Wiener estimate depends on the noise variances. We therefore introduce a factor α, allowing the model to compensate for these mismatches. The resulting optimization problem can then be written as:

$$\{\hat{D}_{LS}(x), \hat{v}_{LS}(x)\} = \min_{D,v} \|\alpha \vec{g}(v,D) - \bar{\vec{w}}\|_2^2 = \min_{D,v} \|\alpha \vec{g}(v,D) - \frac{1}{|S_c|} \sum_{i \in S_c} \hat{\mathrm{R}}_x^{-1} \hat{\vec{r}}_{d_i x}\|_2^2, \tag{2.18}$$

where $\vec{g}(v,D) = \begin{bmatrix} g[1|v,D] & \cdots & g[n|v,D] \cdots & g[N|v,D] \end{bmatrix}$ is the discrete version of $g(L,t|v,D)$, with $g[n|v,D]$ being the n^{th} sample of this vector. The challenging inversion of $\hat{\mathrm{R}}_x$ can be addressed by regularization as given in (2.12) and (2.13). As we are only interested in the convection-diffusion model parameters, the inversion of the autocorrelation matrix can be avoided by rewriting the LS problem such that we have:

$$\{\hat{D}_{LS}(x), \hat{v}_{LS}(x)\} = \min_{D,v} \|\alpha \hat{\mathrm{R}}_x \vec{g}(v,D) - \frac{1}{|S_c|} \sum_{i \in S_c} \hat{\vec{r}}_{d_i x}\|_2^2. \tag{2.19}$$

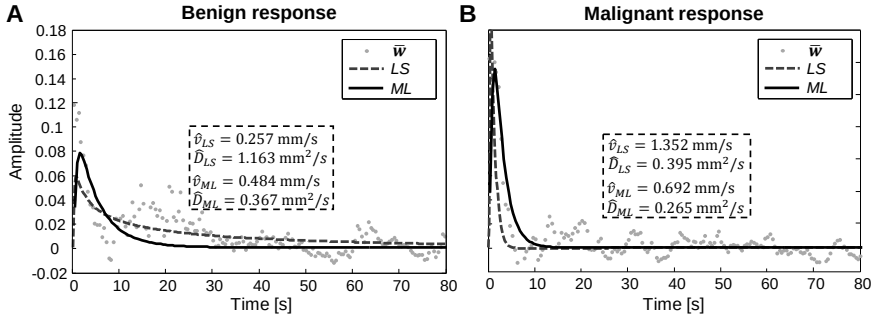

Figure 2.3: Wiener filter coefficient estimates obtained from a pixel in a benign (a) and a malignant (b) region. The convection-diffusion Green's functions for least squares (LS) and maximum likelihood (ML) parameter estimation are also shown.

The Péclet number, being the well-known dimensionless number describing the ratio between the dispersive time and the convective time,[96,97] is then estimated as:

$$\hat{\mathrm{Pe}}_{LS} = L\frac{\hat{v}_{LS}}{\hat{D}_{LS}}. \tag{2.20}$$

2.2e Maximum Likelihood parameter estimation

So far we assumed the local dynamic transport of microbubbles to be a solely deterministic process. However, for low microbubble concentrations it may be more realistic to express it as a stochastic process. In fact, the probability that a number of microbubbles X is delayed by n time samples from $\vec{x}$ to $\vec{d}_i$, may be modelled as a binomial distribution[98,99] with an expected value determined by the local hemodynamics. Here, the probability mass function of individual particle transit times is assumed to be $\mathrm{p}[n|v,D] = g[n|v,D]/|\vec{g}(v,D)|_1$, where $|\cdot|_1$ denotes the $\mathbb{L}_1$ norm. If the total number of particles K is high enough and the sample time is small enough, the probability that $k[n]$ particles have a transit time of n time samples can be approximated by a Poisson distribution[99], having a variance equal to the expected value:

$$\mathrm{P}(X = k[n]|\lambda) = \frac{\lambda^{k[n]}e^{-\lambda}}{k[n]!}, \tag{2.21}$$

where $\lambda = \mathrm{E}[X] = \mathrm{Var}[X] = K\mathrm{p}[n|v,D]$. For the purpose of estimating the transport kinetics, this non-additive, signal-dependent variance is regarded as noise. Since the noise model is not following a normal distribution and is signal dependent, the LS solution does not yield minimum-variance estimation. In this case, a more suitable approach may be to use a Maximum Likelihood (ML) estimator,[100] which is an asymptotically minimum-variance unbiased estimator that does not assume a specific noise

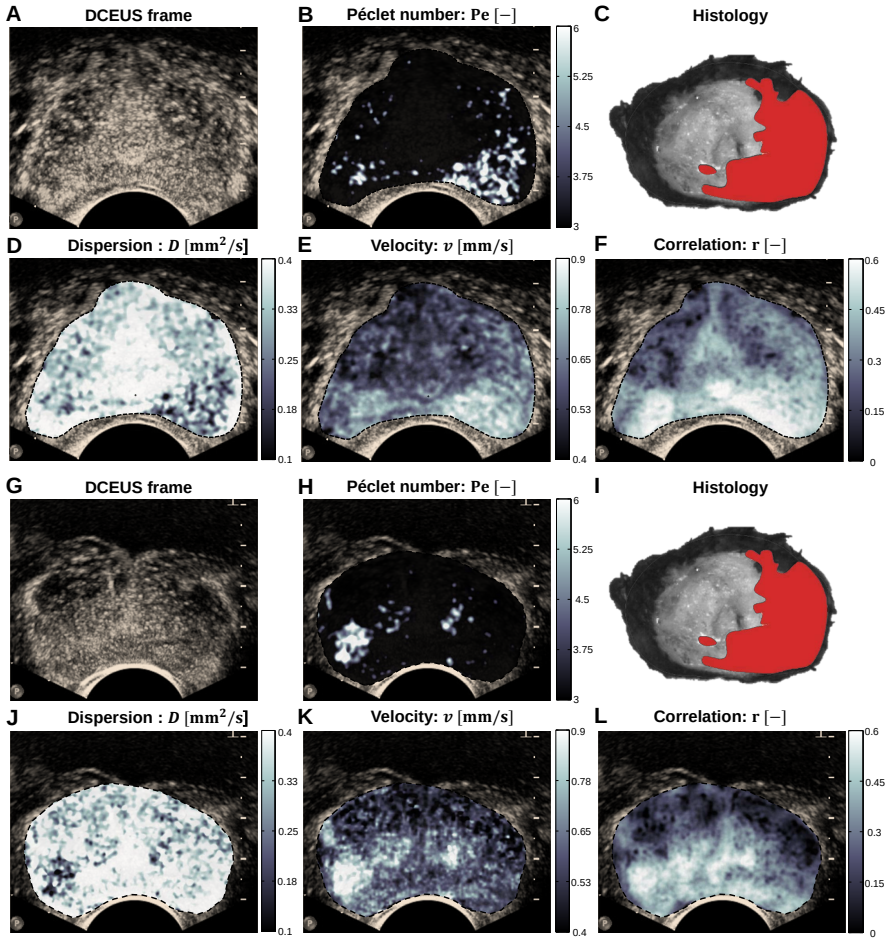

Figure 2.4: Two examples of DCE-US frames (A,G), together with the obtained hemodynamic parametric images showing the Péclet number Pe (B,H), the dispersion coefficient D (D,J), and the velocity v (E,K). Plots (F,L) show the maps based on the dispersion-related correlation analysis r^{72}. The corresponding histology slices are shown in (C,I), where malignant tissue is marked in red.

distribution. The log likelihood of the model parameters $\vec{\theta} = \{v, D\}$ is given by:

$$
\begin{aligned}
l(\vec{\theta}) &= \ln \prod_{n=1}^{N} \mathrm{P}(X = k[n]|\lambda) = \sum_{n=1}^{N} \ln\left(\frac{\lambda^{k[n]} e^{-\lambda}}{k[n]!}\right), \\
&= \sum_{n=1}^{N} k[n] \ln(\lambda) - \lambda - \ln(k[n]!), \\
&= \sum_{n=1}^{N} k[n] \ln\left(K \frac{g[n|\vec{\theta}]}{|\vec{g}(\vec{\theta})|_1}\right) - \frac{K}{|\vec{g}(\vec{\theta})|_1} \sum_{n=1}^{N} g[n|\vec{\theta}] - \sum_{n=1}^{N} \ln[k[n]!], \\
&= \sum_{n=1}^{N} k[n] \ln\left(K \frac{g[n|\vec{\theta}]}{|\vec{g}(\vec{\theta})|_1}\right) - \sum_{n=1}^{N} \ln[k[n]!] \qquad (2.22)
\end{aligned}
$$

which can be maximized to obtain the model parameters $\vec{\theta}$ as

$$\hat{\vec{\theta}} = \max_{\vec{\theta}} \sum_{n=1}^{N} k[n] \ln\left(\frac{g[n|\vec{\theta}]}{|\vec{g}(\vec{\theta})|_1}\right). \tag{2.23}$$

Using that $k[n]$, is proportional to the corresponding estimated Wiener coefficient $\bar{w}[n]$, we obtain

$$\hat{\vec{\theta}} = \max_{\vec{\theta}} \sum_{n=1}^{N} \bar{w}[n] \ln\left(\frac{g[n|\vec{\theta}]}{|\vec{g}(\vec{\theta})|_1}\right) \approx \max_{\vec{\theta}} \sum_{n=1}^{N} \bar{w}[n] \left\{\ln\left(g[n|\vec{\theta}]\right) + \ln(v)\right\}, \tag{2.24}$$

where we used that the area under the curve $|\vec{g}(\vec{\theta})|_1 \propto 1/v$ according to the Stewart-Hamilton equation.[101,102] Besides its advantages regarding the noise distribution, this specific ML problem has an analytical solution, which greatly reduces computational complexity with respect to the iterative approach required for the nonlinear LS problem. By taking the derivatives of (2.24) with respect to the model parameters and determining their zero crossings (see Appendix), we can obtain the following ML estimators for the velocity:

$$\hat{v}_{ML} = L \frac{\sum_{n=1}^{N} \frac{\bar{w}[n]}{n\Delta t}}{\sum_{n=1}^{N} \bar{w}[n]}, \tag{2.25}$$

where Δt is the sample time, and the dispersion coefficient

$$\hat{D}_{ML} = \frac{\sum_{n=1}^{N} \frac{\bar{w}[n]}{n\Delta t}[L - v(n\Delta t)]^2}{2\sum_{n=1}^{N} \bar{w}[n]} = L^2 \frac{\sum_{n=1}^{N} \frac{\bar{w}[n]}{n\Delta t}\left(1 - \frac{\sum_{m=1}^{N} \frac{\bar{w}[m]}{m\Delta t}}{\sum_{m=1}^{N} \bar{w}[m]} n\Delta t\right)^2}{2\sum_{n=1}^{N} \bar{w}[n]}. \tag{2.26}$$

The Péclet number is then estimated as:

$$\hat{\mathrm{Pe}}_{ML} = L \frac{\hat{v}_{ML}}{\hat{D}_{ML}}. \tag{2.27}$$

A disadvantage of the ML approach is the required inversion of $\hat{\mathrm{R}}_x$ to obtain $\bar{\vec{w}}$ according to (2.14) and (2.15).

Table 2.1: Classification results based on Pe, v, and D as obtained using Maximum Likelihood (ML) and Least Squares (LS) optimization, compared to the results obtained using the previously developed dispersion-related correlation analysis[72] and the pixel-wise modified local density random walk curve-fitting approach.[71] The optimal sensitivity (SEN), specificity (SPC), negative predictive value (NPV) and positive predictive value (PPV) are given.

	Parameter	SEN [%]	SPC [%]	NPV [%]	PPV [%]	ROC curve area
ML	v	72.5	82.1	74.9	80.2	0.807
	D	62.5	71.8	65.7	68.9	0.733
	Pe	73.4	79.9	75.0	78.5	0.835
LS	v	70.2	73.3	71.1	72.4	0.777
	D	58.3	46.9	52.9	52.3	0.521
	Pe	57.5	56.0	56.9	56.6	0.592
[71]	κ	65.2	67.6	63.2	69.5	0.718
[72]	r	64.0	74.9	64.8	74.3	0.730

2.3 Data acquisition

The *in vivo* DCE-US investigations were performed at the AMC University Hospital (Amsterdam, The Netherlands). In total, 25 patients with biopsy-proven prostate cancer scheduled for radical prostatectomy were included in this study. In some rare cases, severe motion artifacts due to patient movement (e.g., coughing) occurred during the ultrasound acquisitions. These acquisitions could not be analysed. The passage of a microbubble bolus through the prostate was obtained using an intravenous injection of 2.4-mL SonoVue® (Bracco, Milan, Italy), and consecutively imaged using a 2D transrectal ultrasound probe (C10-3v) and a Philips iU22 ultrasound system (Philips Healthcare, Bothell, WA). The ultrasound system's pixel size is 0.146 × 0.146 mm. Its elevational beam-width at 2 cm from the probe is approximately 1.4 mm. At a distance of 5 cm this value is about 3.4 mm. For each injection one plane was acquired. To record the full in- and out-flow, DCE-US acquisitions were performed during 120 s. The clinicians waited 180 s before the next injection/acquisition phase, so that most bubbles were dissolved. When insonified, microbubbles exhibit a resonating behavior that is strongly nonlinear with respect to the incident pressure. Exploiting this, a contrast agent-specific imaging mode based on a power modulation pulse scheme at 3.5 MHz was used to enhance sensitivity to microbubbles while suppressing linear backscattering from tissue. The mechanical index was set to 0.06, high enough to obtain sufficient echo signal power, while still limiting microbubble destruction[103],[104].

Using the methods described in,[71] the relation between SonoVue® concentration and acoustic intensity, along with the ultrasound scanner's compression function were determined and used to estimate the linearised IDCs from the measured acoustic intensity. For SonoVue® concentrations up to 1.0 mg/L, the contrast agent concentration and acoustic intensity were found to be linearly correlated ($R^2 = 0.96$)[71].

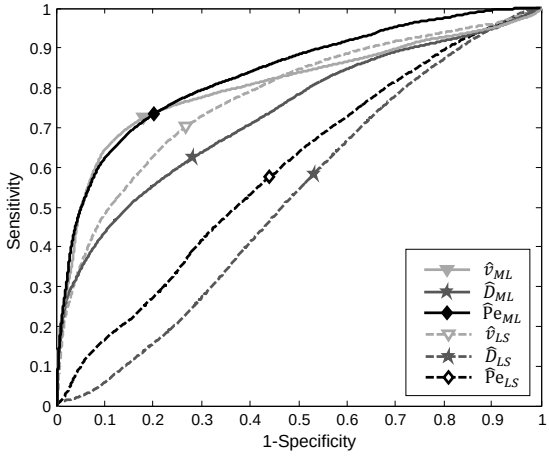

Figure 2.5: The Receiver-Operating-Characteristic (ROC) curves for classification of benign and malignant pixels by the estimated dispersion coefficient (D), velocity (v) and Péclet number (Pe), as obtained using Maximum Likelihood (ML) and Least Squares (LS).

2.4 Validation methodology

To evaluate the potential of the developed imaging method at localizing prostate cancer, a clinical validation was carried out using a dataset consisting of 61 DCE-US imaging planes recorded from 25 patients that underwent radical prostatectomy at the AMC University Hospital (Amsterdam, The Netherlands). The median number of planes recorded per patient was 2, ranging between 1 and 4. After radical prostatectomy, histopathological analysis of the prostate was performed. The prostate was dissected in slices of 4-mm thickness, and a pathologist marked the presence of cancer based on the level of cell differentiation, according to[105]. Using the histology results, regions of interest (ROI's) of approximately 0.5 cm^2 covering benign and malignant pixels were manually selected from the ultrasound data. Malignant was defined as tissue with a Gleason grade of at least 3+3=6.[13] Registration was performed cognitively. For this purpose, fundamental mode (B-mode) sweep videos ranging from base to apex where acquired. By comparing this with the fundamental mode image obtained in the contrast imaging plane, the contrast imaging plane's location was determined. Then the corresponding histology slice was chosen. To mitigate errors due to plane mismatch between ultrasound and histology, the ROI's were selected by considering tumours that occur throughout 3 neighbouring histology slices. In total, the ROI's contained approximately 177×10^3 voxels, of which 51% was taken from benign regions. After post-filtering the feature maps using a Gaussian spatial filter with a standard deviation σ_{post} = 1.3 mm, pixel-based classification was performed. For each feature, the Receiver-Operating-Characteristics (ROC) curves were calculated, after which the optimal threshold was determined as a trade-off between sensitivity and specificity by selecting the point on the ROC curve that is closest to the ideal classification, *i.e.* the top-left corner. Based on this, the area under the ROC curve, sensitivity, specificity, positive predictive value (PPV), and negative predictive value (NPV) of the individual parameters were calculated.

The performance of the ML and LS estimators across the observations were compared by calculating p-values of the difference between their area under the ROC curve. The

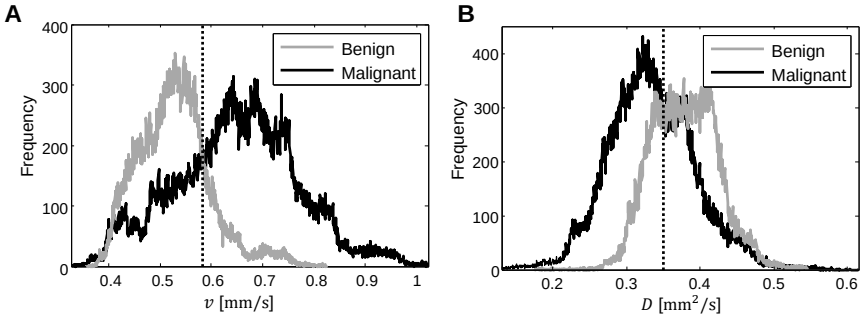

Figure 2.6: The benign and malignant class histograms for the Maximum Likelihood estimates of the velocity (v) and dispersion coefficient (D). The optimal classification thresholds are indicated by a dashed line. A pixel was classified malignant for $v > 0.583$ mm/s, and for $D < 0.350$ mm^2/s.

required standard errors related to the ROC area are computed according to,[106] and are dependent on the number of independent samples. Taking into account the correlation between pixels within the same ROI, the amount of independent benign and malignant samples is conservatively set to the number of benign and malignant ROI's, being 56 and 57, respectively, as not all planes contained both suitable benign and malignant regions. Suitable planes were defined as planes where a benign or malignant region could be identified throughout 3 neighbouring histology slices. Of the total set of 25 patients, 22 patients provided data for both the benign and malignant classes, 1 patient contributed only to the benign class, and 2 other patients contributed only to the malignant class. The difference in performance was considered significant for $p < 0.01$.

2.5 Results

Figure 2.3 illustrates the model identification procedure in a benign and malignant region. The plots represent the Wiener estimates of the channel between contrast-enhanced curves. We observe in this example that the estimated velocities were higher and the dispersion coefficients were lower for malignant pixels. Next, an example of the parametric images obtained by applying the proposed approach, along with the corresponding histology slice, are shown in Figure 2.4. Model parameter estimation is performed using ML. Although it is not a one-to-one match, the dark areas of the dispersion coefficient images, as well as the enhanced bright areas in the velocity and Péclet number images, qualitatively imply angiogenic vasculature, indicating the tumour's location. For comparison, the maps obtained using the previously developed dispersion-related correlation analysis[72] are also shown.

In Figure 2.5, the ROC curves for pixel-based classification using the dispersion coefficient, velocity, and Péclet number are given. To compare their performances, the curves when employing ML as well as LS to estimate the model parameters are shown. An overview of these results, including the corresponding PPV, NPV, and the ROC curve areas, is given in Table 2.1. We show that using ML instead of LS yielded significantly higher ROC curve areas for the estimation of D ($p = 0.0034$) and Pe ($p = 0.0002$). The improvement with respect to v estimation was not statistically

significant (p = 0.64).

Comparing the ML estimates of v, and D, we observed that v yielded a higher sensitivity and specificity than D. Classification using Pe showed the highest ROC curve area, being 0.84. The spatio-temporal correlation analysis[72] and modified local density random walk curve-fitting approach[71] showed a lower performance, leading to an ROC curve area equal to 0.73 and 0.72, respectively.

To give an indication of the probability distributions of the parameters given the class, histograms of the ML estimates of v and D in the ROI's are shown in Figure 2.6. The benign and malignant class means±standard deviations for v were 0.53±0.07 mm/s and 0.65±0.12 mm/s, respectively. For D these values were 0.38±0.045 mm^2/s and 0.33±0.059 mm^2/s, respectively. One can observe that for malignant pixels, the underlying contrast agent kinetics tended to be characterized by a higher velocity and a lower dispersion compared to benign pixels.

2.6 Discussion

2.6a Contributions and strengths

In this paper, we presented a new approach to prostate cancer localization based on dynamic contrast enhanced ultrasound (DCE-US) imaging. By combining Wiener system identification and model-based parameter estimation, the proposed method enables local characterization of the hemodynamics described by the dispersion coefficient (D), velocity (v), and Péclet number (Pe). The obtained parameters serve as features that relate to angiogenic activity. Stable estimates of the Wiener filter coefficients were obtained by adopting an information theoretic criterion, allowing regularized matrix inversion by determining the pure signal subspace from the eigenvalues, without requiring any subjective threshold settings. Next, model-based Least Squares (LS) and Maximum Likelihood (ML) parameter estimators were derived.

A qualitative comparison of the resulting parametric maps exemplified how the dispersion and velocity maps suggested the presence of angiogenic vasculature by showing dark or bright areas, respectively. The Péclet number map qualitatively displays a higher specificity, with bright areas implying angiogenic activity. Set against the corresponding histology slice, these areas indicated the presence of cancer.

A quantitative analysis showed that the ML parameter estimates outperformed the LS estimates in terms of receiver operator characteristic (ROC) curve area at distinguishing benign from malignant pixels. In particular, the estimated dispersion coefficient, and consequently the Péclet number, showed a significantly improved performance. This was exemplified in Figure 2.3, notably for the displayed malignant case. The ML response was typically more similar to the estimated Wiener coefficients. This result was expected, given that the model parameters are derived from it. On the other hand, the LS model parameters are directly derived from the input autocorrelation and output-input cross-correlations to avoid matrix inversion (2.19). By comparing the performance of v, D, and Pe, we conclude that the highest ROC curve area and the greatest flexibility is obtained for the ML estimate of Pe, having an ROC curve area of 0.84. followed by the ML and LS estimates of v. Although the ML estimate of D performs worse than v, it

does show diagnostic value and yields an ROC curve area of 0.73.

The lower dispersion observed in malignant regions may be a result of the tortuous nature of angiogenic neovasculature, limiting the diffusion of contrast agents in the measurement cell. This process is very similar to the diffusion of particles through porous media, where a decrease in macroscopic diffusion owing to irregular geometry of the porous media is predicted.[92] The effective diffusion decreases with increasing tortuosity.[107] Angiogenic vascularity is also characterized by high-velocity arteriovenous shunts[108,109] that may cause the observed elevated flow velocities in malignant regions. The overlap of benign and malignant classes for velocity and dispersion seen in Figure 2.6 may have several origins. First of all, the hypothesis that dispersion and velocity reflect angiogenic activity may not always hold. Secondly, angiogenesis could be absent in some of the malignant regions. Thirdly, the heterogeneous nature of tumour vasculature could introduce fluctuations of the hemodynamic parameters in the regions[85]. In this regard it is interesting to note that the standard deviations of the malignant classes are higher than those of the benign classes for both velocity and dispersion. In addition to this, angiogenesis can be present as a result of benign tissue inflammation. Finally, technical problems related to noise and artifacts could impair the model estimation accuracy.

The estimated velocity values are mostly in the sub-millimetre per second range; suggesting that flow in the capillaries is indeed measured. In,[110] red blood cell velocity was measured by television microscopy. The authors reported mean velocities of 0.47 and 0.84 mm/s for venular and arteriolar capillary limbs, respectively. Later,[111] human capillary blood velocity was determined with a laser Doppler anemometer, and a mean blood velocity of 0.47 mm/s (range 0.14 to 0.93 mm/s) was obtained. For comparison, we estimated a mean velocity of 0.53 mm/s in benign regions with the proposed method.

Adding to this, in[112], normal and tumour red blood cell fluxes were compared in a rat window chamber model. Red blood cell flux was found significantly greater in tumours than in normal tissues. In[113], red blood cell velocities where found to be twice as high in tumours as in granulating tissues for dorsal flap window chamber rat models. Related to this, in[114], elevated velocity values (although not statistically significant) in PC-3 (human prostate cancer line) mice where measured as compared to controls. However, in some other tumour models red blood cell velocity is found to be lower in tumour microvasculature as compared to normal tissues[85]. Increased flow resistance due to increased interstitial pressure can lower tumour perfusion. That being said, the macroscopic impact of possibly lowered velocities in the smallest neo-vasculature on the velocity estimates is determined by the local microbubble concentration.

With respect to previous methods that aim at characterizing contrast agent bolus dispersion,[71,72,88,98] the proposed approach enabled for the first time independent extraction of UCA dispersion and velocity from DCE-US. In[71] and[98], a Gaussian spatial input concentration was assumed such that a diffusion-related parameter could be identified from an IDC. This parameter is a function of dispersion and velocity. The methods in[72] and[88] aim at reflecting changes in the physical parameters (velocity and dispersion) by analysing the spatial similarity of time intensity curves. As a result, changes in this similarity also reflect changes in a combination of velocity and dispersion. Alternatively, the present study is aimed at independent estimation of velocity and dispersion. Moreover, compared to previous methods, this approach no longer requires the assumption of a Gaussian spatial input concentration.

The ability to independently estimate dispersion and velocity not only provides relevant insights into the relation between dispersive and convective processes for contrast agents in angiogenic vasculature, but it also opens up possibilities for more advanced characterization. In this regard, the advantage of exploiting independent estimation of dispersion and velocity becomes evident when considering the future application of dedicated classification algorithms to localization of angiogenesis. Whilst using Pe already improved the classification results by combining D and v in a straightforward way, a better combination may be identified by employing machine learning techniques.[115] Such an approach benefits from having independent and physically relevant features.

DCE-US imaging suffers from artefacts due to attenuation and nonlinear propagation. The resulting variations of echo-intensity over the imaging domain strongly affect intensity-based DCE-US quantification techniques. The proposed method characterizes the dynamics of the local system and is not impaired by time-invariant artefacts. However, in specific time-variant cases heavy nonlinear propagation artefacts can impact the estimates. One example occurs in the presence of far wall pseudo-enhancement in combination with movement, leading to strongly correlated and time-varying time-intensity curves. These types of artefacts may be reduced by advances in contrast-enhanced ultrasound imaging technology.[116]

2.6b Limitations

A limitation of the present study lies in the quantitative validation procedure. Standard histology assesses the degree of cell differentiation, which does not necessarily map one-to-one with the angiogenic activity that the method aims to detect. Furthermore, the ultrasound imaging planes are generally not parallel to the histology slices, as the dissection procedure is constrained by pathological guidelines. Although these problems are mitigated by considering multiple histology slices when selecting the regions of interest, errors might still be present. Since slices with small and scattered tumours were not considered suitable for drawing regions, the performance evaluation in this work is biased towards larger tumours that are consistent through multiple histology slices. The cognitive registration of fundamental mode ultrasound planes and histology slices, along with a manual selection of regions of interest was performed prior to the development of the method. A more detailed analysis that includes small and inconsistent (yet clinically significant) tumours may be enabled by advanced and dedicated registration algorithms.[117]

The DCE-US data used in this study is limited to 2D spatial information. Because of this, local channel estimation is affected by out of plane flows. As a result, the estimated absolute parameter values will differ from the real parameters. In fact, the pixel-wise value depends on the elevation angle of the flow. In the worst case, the apparent causality between the measured output and input indicator dilution curves may in fact not represent physical causality. This can occur for flow directions that are perpendicular to the imaging plane.

Hence, with the technical limitations of 2D DCE-US imaging, only macroscopic features representing the actual 3D vascular network can be estimated. In this regard, we assumed the elevation orientation components of the physical parameters, and their projections on the imaging plane, to have a broad distribution over the final resolution

cell volume ($2.355\sigma_{post} \times 2.355\sigma_{post} \times 1.4$ mm $\approx 3 \times 3 \times 1.4$ mm). The average macroscopic behaviour was then estimated using spatial post-filtering with a Gaussian kernel, and its clinical relevance with respect to prostate cancer localization was evaluated.

2.6c Perspectives

The frequently repeated biopsy indicated by active surveillance regimens is a burden to both patients and healthcare systems. It can cause complications, and the anxiety and discomfort associated with the repetitive biopsies may be a reason for patients to quit active surveillance. Imaging with a high negative predictive value for clinically significant disease can potentially defer or delay the need to repeat biopsy. The negative predictive required to defer biopsies depends on the risk of delayed detection of significant disease that patients and caregivers are willing to accept, but we can argue it should be above of the 80-90% range. The specificity then determines the proportion of biopsies that can actually be deferred. Nevertheless, we do not expect the decision to re-biopsy to be based on imaging alone in the near future; a significant rise of prostate specific antigen[118] despite negative imaging should prompt re-biopsy during active surveillance.

When clinical suspicion persists in spite of negative biopsies, the current European guidelines for prostate cancer recommend taking multiparameteric Magnetic Resonance Imaging (mpMRI)-targeted biopsies.[119] The long-term positioning of our DCE-US method will be decided by the results of future extended validation. Should the results become similar or better than those by mpMRI in a large cohort, one can contemplate replacing mpMRI. Advantages over mpMRI are the lower costs and higher mobility of the equipment, different/fewer contraindications, and US-US registration is likely less prone to error than MRI-US registration for biopsy targeting purposes. US equipment is also compatible with a wider set of (metal containing) focal therapy equipment than the MRI unit. Obviously these advantages come second to accurate tumour detection; this is where the proposed method will have to prove itself relative to mpMRI. In the short-term, we are going to use the technique next to mpMRI for comparison and assessment of their complementarity.

Within mpMRI protocols, dynamic contrast-enhanced MRI is often employed, making use of gadolinium contrast agents. These agents extravasate across the vessel wall and are often used to assess vascular permeability. In this context, the approach described in the present work may be followed to determine local gadolinium convection and dispersion along with permeability. The proposed impulse-response estimators should than be adjusted and based on dedicated models that combine these three terms.[120]

Technological developments currently facilitate 4D DCE-US imaging, which allows analysis of 3D spatial data over time[121] and enables exploitation of more elaborate system identification techniques. In this respect, one can imagine estimation of the 3D convection-diffusion model parameters, possibly providing more information relevant to the localization of angiogenesis. Therefore, adapting the developed approach to 4D DCE-US will be part of future work.

2.7 Conclusions

This paper proposes for the first time a method for the independent estimation of dispersion and velocity of ultrasound contrast agents (UCAs) based on dynamic contrast enhanced ultrasound (DCE-US) imaging. With the aim of localizing prostate cancer (PCa), the developed method enables local characterization of the vascular hemodynamics described by the apparent in-plane dispersion coefficient, velocity, and Péclet number of UCAs. A quantitative analysis on 25 patients revealed that PCa detection based on the ratio of UCA velocity and dispersion (the Péclet number) yields the highest receiver-operating-characteristics curve area (0.84). The presented clinical results are encouraging, even though they are constrained to the analysis of in-plane kinetics. Future work will include translation of the developed method to 4D DCE-US.

2.8 Appendix: ML estimators

Starting from the result of (2.24)

$$\hat{\vec{\theta}} = \max_{\vec{\theta}} \{ l(\vec{\theta}) \} \approx \max_{\vec{\theta}} \sum_{n=1}^{N} \bar{w}[n] \left\{ \ln \left(g[n|\vec{\theta}] \right) + \ln(v) \right\}, \tag{2.28}$$

we take the partial derivatives with respect to the model parameters v and D, and equate them to zero:

$$\partial_v l(\vec{\theta}) = \sum_{n=1}^{N} \bar{w}[n] \left\{ \frac{\partial_v g(n|v,D)}{g(n|v,D)} + \frac{1}{v} \right\} = 0, \tag{2.29a}$$

$$\partial_D l(\vec{\theta}) = \sum_{n=1}^{N} \bar{w}[n] \left\{ \frac{\partial_D g(n|v,D)}{g(n|v,D)} \right\} = 0, \tag{2.29b}$$

which, when using (2.17) with sample time Δt, leads to

$$\partial_v l(\vec{\theta}) = \sum_{n=1}^{N} \bar{w}[n] \left\{ \frac{(L - vn\Delta t)}{2D} + \frac{1}{v} \right\} = 0, \tag{2.30a}$$

$$\partial_D l(\vec{\theta}) = \sum_{n=1}^{N} \bar{w}[n] \left\{ \frac{(L - vn\Delta t)^2 - 2Dn\Delta t}{4D^2 n\Delta t} \right\} = 0. \tag{2.30b}$$

Next, we can rewrite (2.30) such that we have

$$D \sum_{n=1}^{N} \bar{w}[n] = - \sum_{n=1}^{N} \bar{w}[n] \frac{v(L - vn\Delta t)}{2}, \tag{2.31a}$$

$$D \sum_{n=1}^{N} \bar{w}[n] = \sum_{n=1}^{N} \bar{w}[n] \frac{(L - vn\Delta t)^2}{2n\Delta t} = 0. \tag{2.31b}$$

Then, we subtract (2.31b) from (2.31a) to obtain:

$$\sum_{n=1}^{N} \bar{w}[n] \left\{ \frac{vL}{2} - \frac{L^2}{2n\Delta t} \right\} = 0, \tag{2.32}$$

from which we can obtain the ML estimate of the velocity as:

$$\hat{v}_{ML} = L \frac{\sum_{n=1}^{N} \frac{\bar{w}[n]}{n\Delta t}}{\sum_{n=1}^{N} \bar{w}[n]}. \tag{2.33}$$

Finally, we use $\hat{v}_{ML}$ to solve (2.30b), and obtain the ML estimate of the dispersion

coefficient as:

$$\hat{D}_{ML} = \frac{\sum_{n=1}^{N} \frac{\tilde{w}[n]}{n\Delta t}\left[L - v(n\Delta t)\right]^2}{2\sum_{n=1}^{N} \tilde{w}[n]}. \tag{2.34}$$

2.9 Acknowledgements

This work is part of the research programme 10769, which is partly financed by the Netherlands Organization for Scientific Research (NWO). The research has also received funding from the European Research Council / ERC grant agreement n. 280209.

3

Entropy of Ultrasound-Contrast-Agent Velocity Fields

Abstract - *Prostate cancer care can benefit from accurate and cost-efficient imaging modalities that are able to reveal prognostic indicators for cancer. Angiogenesis is known to play a central role in the growth of tumours towards a metastatic or a lethal phenotype. With the aim of localizing angiogenic activity in a non-invasive manner, Dynamic Contrast Enhanced Ultrasound (DCE-US) has been widely used. Usually, the passage of ultrasound contrast agents thought the organ of interest is analysed for the assessment of tissue perfusion. However, the heterogeneous nature of blood flow in angiogenic vasculature hampers the diagnostic effectiveness of perfusion parameters. In this regard, quantification of the heterogeneity of flow may provide a relevant additional feature for localizing angiogenesis. Statistics based on flow magnitude as well as its orientation can be exploited for this purpose. In this paper, we estimate the microbubble velocity fields from a standard bolus injection and provide a first statistical characterization by performing a spatial entropy analysis. By testing the method on 24 patients with biopsy-proven prostate cancer, we show that the proposed method can be applied effectively to clinically acquired DCE-US data. The method permits estimation of the in-plane flow vector fields and their local intricacy, and yields promising results (receiver-operating-characteristic curve area of 0.85) for the detection of prostate cancer.*

From: R.J.G. van Sloun, L. Demi, A.W. Postema, J.J.M.C.H. de la Rosette, H. Wijkstra, and M. Mischi,"Entropy of Ultrasound-Contrast-Agent Velocity Fields for Angiogenesis Imaging in Prostate Cancer", *IEEE Transactions on Medical Imaging*, vol. 6, ©IEEE, 2017

3.1 Introduction

Prostate cancer (PCa) is the second-leading cause of cancer death in men, and the most frequently diagnosed cancer in men aside from skin cancer.[79] PCa diagnosis is typically performed using systematic needle biopsies, guided by transrectal ultrasound (TRUS): the extraction and examination of prostate gland samples based on a standard template. The samples are microscopically assessed based on the histopathological degree of cell differentiation, quantified by the Gleason score.[13] In this case, TRUS is merely used to guide the biopsy needle. Despite being the current golden standard, initial systematic biopsies miss nearly a quarter of the clinically significant cancers,[15] requiring additional biopsy sessions in case of suspicion. To enhance tumour detection rates, targeting of biopsies using multi-parametric magnetic resonance imaging (mpMRI)[122,123] has been proposed. This strategy combines T2 weighted and Diffusion weighted imaging with Dynamic Contrast Enhanced MRI (DCE-MRI) to detect and classify lesions, which can be targeted specifically during the biopsy procedure. Besides enabling targeted biopsies, accurate delineation of lesions using imaging would permit the use minimally invasive therapies such as focal therapy as opposed to radical prostatectomy. Nevertheless, mpMRI is a modality with high costs and a complex workflow. It would therefore be favourable to perform these diagnostic strategies by cost-effective TRUS.

Dynamic Contrast Enhanced Ultrasound (DCE-US) is a minimally invasive imaging modality that can be applied using TRUS. Where DCE-MRI in mpMRI is mainly used to assess microvascular permeability, DCE-US is used to analyse perfusion, by imaging an intravenously injected cloud of contrast agents that remain intra-vascular. In the context of tumour detection, a particularly interesting application of DCE-US concerns the localization of neo-angiogenic vascularization associated with tumour growth and metastasis,[58,59,60] and of lethal phenotypes.[61]

The microvascular network that originates from tumour-driven angiogenesis is characterized by increased microvascular density (MVD) and tortuosity, as well as by the presence of irregular branching and arteriovenous shunts. Decreasing functional vascular cross-sectional area in neoplastic tissue can increase flow resistance. Hypoxia in tumours due to ineffective blood flow can lead to deteriorated endothelial wall cells, causing extra-vascular leakage and metastases[124]. These factors contribute to heterogeneous blood flow in angiogenic vasculature,[85,125]. In this paper, we aim at localizing tumour-driven angiogenesis by exploiting the heterogeneity induced in the microvascular blood flow.

Focusing on increased microvascular density, several researchers have studied DCE-US time-intensity features related to microvascular perfusion.[82–84] However, ultrasound attenuation and scanner settings may affect the estimation of local contrast-agent concentration and the resulting amplitude-based perfusion parameters.[126–128] Moreover, its effectiveness is hampered by the heterogeneous nature of blood flow in angiogenesis. Exploiting this, intra-tumour vascular heterogeneity has been assessed for DCE-CT[86] and DCE-MRI.[129] In the domain of ultrasound, a histogram-based characterization of contrast agent wash-in rate distributions was used to classify benign or malignant ROIs.[130] Later, a DCE-US perfusion clustering algorithm was developed for the assessment of perfusion heterogeneity.[131] As an alternative to perfusion related parameters, features

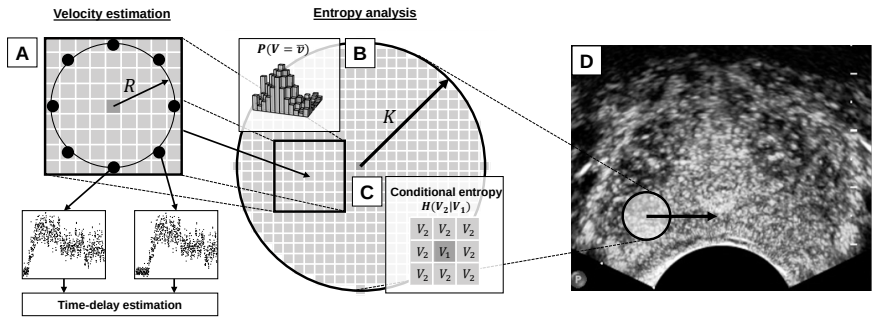

Figure 3.1: An illustration of the analysis steps: First, the velocity vector is estimated for all pixels based on IDC time-delay estimation (A). Then, its bivariate probability distribution is estimated within a kernel to derive the entropy (B). Finally, the conditional entropy is determined (C), and the kernel is translated across imaging plane (D).

linked to contrast agent bolus dispersion have been proposed.[71,72] These approaches are based on the hypothesis that structural alterations in the vascular architecture result in variations in contrast agent spreading: a macroscopic perspective of vascular characterization that is connected to modelling of flow through porous media.[94,132]

Additionally, disruption-replenishment techniques were investigated for vascular characterization[133]. After disrupting all microbubbles with a high-intensity flash, reperfusion kinetics are assessed by extracting parameters related to vascular cross-sectional area, mean flow speed, and vascular heterogeneity of the microvasculature using a log-normal model for the spatial flow distribution. Such approaches require the use of a destructive flash along with a steady infusion of contrast agents, and quantification depends on the angle between the imaging beam and the replenishing vessels[134].

In this work, we infer vascular heterogeneity by providing a bivariate statistical characterization of flow including contrast agent directionality. To this end, we first measure the ultrasound contrast agent's (UCA) indicator dilution curves (IDCs; a measure of contrast agent concentration over time) that result from an intravenous bolus injection at each pixel. From this, we estimate the local propagation vector of the agent's distribution over space. By estimating the time-delays between the IDCs measured at a set of imaging pixels, the macroscopic flow direction as well as its magnitude can be estimated. The diversity or disorder of the resulting vector field is then assessed by evaluating Shannon's Entropy,[135,136] ultimately yielding a measure of heterogeneity. Its diagnostic value is evaluated on data acquired from 24 patients and compared against histology.

The remainder of this paper is organized as follows. We first describe the data acquisition protocol (Secs. 3.2a-3.2c). A velocity vector field estimator is then derived based on a two-stage cross-correlation/least squares approach (Sec. 3.2e). Next, two approaches for statistical characterization based on Entropy (Sec 3.2f) and Conditional Entropy (Sec. 3.2g) are proposed. The adopted validation methodology is reported in Sec. 3.3, and the results are presented in Sec. 3.4. Finally, in Sec. 3.5, the results are discussed and conclusions derived.

3.2 Methods

3.2a Patient population

Initially, twenty-five patients scheduled for radical prostatectomy where included in this study. DCE-US investigations were performed on all patients. One patient was excluded based on unreliable histological data, compromising the validation procedure. The study was approved by the local ethics committee. All patients signed informed consent.

3.2b DCE-US data acquisition

The DCE-US data were acquired at the AMC University Hospital (Amsterdam, the Netherlands). An intravenous injection of a 2.4-ml UCA bolus (SonoVue®, Bracco, Milan, Italy) was administered, and its passage through the prostate was imaged using a C10-3v transrectal endfiring ultrasound probe. The DCE-US loops were acquired and stored using a Philips iU22 ultrasound system (Philips Healthcare, Bothell, WA), operating in a contrast-specific imaging mode. This mode exploits the microbubble's nonlinear behaviour using a power modulation pulse scheme at 3.5 MHz to suppress linear backscattering from tissue. A low mechanical index of 0.06 was used to minimize microbubble destruction.[104] The frame rate was 10 Hz. The axial resolution of the ultrasound system is approximately 0.3 mm and its lateral resolution is in the order of 0.5 mm at 5 cm from the probe. At this distance, the elevational beamwidth is approximately 3.4 mm. The pixel spacing is 0.146 mm in both directions. The median number of DCE-US planes recorded per patient was 2, ranging between 1 and 4. Imaging was performed for 120 seconds to record the full in- and out flow.

3.2c Histopathological analysis

A radical prostatectomy was performed in all patients. After resection, the prostate specimen was fixed in formalin, and dissected in 4-mm-thick slices. The slices were Haematoxylin & Eosin stained, and a pathologist determined the presence and extent of the tumour, based on the level of cell differentiation, according to.[105] Six patients had a Gleason score of $3 + 3 = 6$, nine patients had a Gleason score of $3 + 4 = 7$, five patients had a Gleason score of $4 + 3 = 7$, one patient had a Gleason score of $3 + 5 = 8$, one patient had a Gleason score of $4 + 5 = 9$, and two patients had a Gleason score of $5 + 4 = 9$.

3.2d Pre-processing

Prior to the analysis, the recorded log-compressed and quantized time-intensity curves were linearised to obtain IDCs using the methods described in.[71] A spatial Gaussian filter with a standard deviation of one pixel (0.146 mm) was then applied to mitigate the impact of spatially incoherent noise[137].

3.2e Velocity vector field estimation

For the purpose of estimating the in-plane UCA velocity vector at a certain location, we consider the IDCs that are measured at a specific set of imaging pixels around this location: N pixels distributed on a circle with radius R. The IDC shapes of two closely spaced pixels (< 2.2 mm) is similar since local effects are dominated by the complete UCA bolus history. Hence, assuming the transport of UCAs between two distinct pixels in this set to be convection-dominated, the measured IDCs may be written as:

$$y_1(t) = u_1(t)s(t) + n_1(t) \tag{3.1}$$

$$y_2(t) = u_2(t)s(t-\tau) + n_2(t), \tag{3.2}$$

where $s(t)$ represents the time evolution of contrast signal, τ is its time-delay with respect to the arrival time at the first pixel, $n_1(t)$, $n_2(t)$ are i.i.d additive noise components, and $u_1(t)$, $u_2(t)$ are i.i.d multiplicative noise components. The additive noise components model e.g. thermal and electronic noise, whereas the multiplicative components can describe the effects of speckle noise on the measured IDCs ([98,138]). The time-delay τ can be estimated by maximizing the cross-correlation function between $y_1(t)$ and $y_2(t)$, i.e.

$$\begin{aligned}\hat{\tau}_{1,2} &= \arg\max_{\tilde{\tau}} \mathrm{E}\left[y_1(t)y_2(t+\tilde{\tau})\right] \\ &= \arg\max_{\tilde{\tau}} \{\mathrm{E}\left[u_1(t)u_2(t)s(t)s(t-\tau+\tilde{\tau})\right] + \mathrm{E}\left[u_2(t)n_1(t)s(t-\tau+\tilde{\tau})\right] \\ &\qquad + \mathrm{E}\left[u_1(t)n_2(t)s(t)\right] + E\left[n_1(t)n_2(t)\right]\} \\ &= \arg\max_{\tilde{\tau}} \mathrm{E}\left[s(t)s(t-\tau+\tilde{\tau})\right], \end{aligned} \tag{3.3}$$

where $\mathrm{E}[\cdot]$ is the expectation operator. This function is maximized for $\tau = \tilde{\tau}$.[139] Analogous to the convolution theorem, the cross-correlation based time-delay estimation can also be performed using the Fourier transform, via:

$$\hat{\tau}_{1,2} = \arg\max_{\tilde{\tau}} \int_{-\infty}^{\infty} Y_1(\omega)Y_2^*(\omega)e^{-j\omega\tilde{\tau}}d\omega, \tag{3.4}$$

where $Y_1(\omega)$ and $Y_2(\omega)$ are the Fourier transforms of $y_1(t)$ and $y_2(t)$, respectively, and $(\cdot)^*$ denotes the complex conjugate. In practice, this allows us to pre-compute and store the Fast Fourier Transforms (FFTs) of all IDCs, reducing the procedure's computation time by avoiding duplicate FFT evaluations while translating the ring-kernel (see Figure 3.1). We then collect all the $N(N-1)$ time-delays amongst all the IDCs from the set in an array $\hat{\vec{\tau}}$. The relation between $\hat{\vec{\tau}}$ and the average velocity vector $\vec{v}$ can be described as:

$$\vec{v}^T\vec{\tau} = \mathrm{D}, \tag{3.5}$$

where D is the $2 \times N(N-1)/2$ matrix that describes the inter-pixel distance vectors. Equation (3.5) is solved for $\vec{v}$ by minimizing the mean squared error between $\vec{v}^T\hat{\vec{\tau}}$ and

D using weighted least-squares minimization:

$$\hat{\vec{v}} = \arg\min_{\vec{v}} \sum_{i}^{N(N-1)} w_i \left| \mathrm{D}_i - \vec{v}\hat{\tau}_i \right|_2^2, \tag{3.6}$$

where D_i is the i^{th} column of D and τ_i is the corresponding time delay. The weight w_i is the value of the normalized cross-correlation function at lag $\hat{\tau}_i$, reflecting our confidence in the time-delay estimate:

$$w_i = \frac{E\left[y_{i,1}(t)y_{i,2}(t+\hat{\tau}_i)\right]}{\sigma_{y_{i,1}}\sigma_{y_{i,2}}}, \tag{3.7}$$

where $\sigma_{y_{i,1}}$ and $\sigma_{y_{i,2}}$ depict the standard deviations of $y_{i,1}$ and $y_{i,2}$, respectively.

This procedure is repeated on a grid of pixels that covers the prostate to produce an estimate of the complete vector field. An *in silico* validation of the velocity vector field estimator is given in appendix 3.6.

3.2f Entropy

To locally assess the amount of diversity or disorder in the field components we calculate its Shannon's entropy.[136] This information theoretical quantity provides a measure of the intricacy of the velocity field pattern: the higher the heterogeneity the higher the entropy. Shannon's entropy is defined as

$$H(V) = -\int \mathrm{P}(\vec{v}) \log \mathrm{P}(\vec{v}) d\vec{v}. \tag{3.8}$$

where $\mathrm{P}(\vec{v} = [v_x, v_y])$ is the two-dimensional probability distribution for the occurrence of a specific velocity vector (x and y components) and log denotes the natural logarithm.

Since $\mathrm{P}(\vec{v})$ is unknown, we estimate its discrete probability mass function from the data based on rectangular bins, by computing the two-dimensional histogram $\tilde{\mathrm{P}}(i,j)$ of all the velocity vectors obtained within a circular kernel of radius K (see Figure 3.1), i.e.,

$$\tilde{\mathrm{P}}(i,j) = \tilde{\mathrm{P}}(V \in \mathrm{bin}\{i,j\}) = \frac{1}{|\mathcal{S}_k|} \sum_{m \in \mathcal{S}_K} c(\vec{v}_m, i, j), \tag{3.9}$$

where $\mathcal{S}_K$ is the set of indices that point to the velocity vectors in the kernel, $\vec{v}_m$ is the m^{th} velocity vector, and the bin function

$$c(\vec{v}_m, i, j) = \begin{cases} 1 & \text{if } \vec{v}_m \in \mathrm{bin}\{i,j\} \\ 0 & \text{otherwise} \end{cases}, \tag{3.10}$$

where the rectangular bin width is $2v_{max}/N_b$, with N_b being the amount of bins in both dimensions and v_{max} the upper limit of the velocity magnitude. The entropy is

then estimated from the data as:

$$\hat{H}(V) = -\sum_{i,j} \tilde{\mathrm{P}}(i,j) \log \tilde{\mathrm{P}}(i,j). \tag{3.11}$$

3.2g Conditional entropy

To extend the analysis of spatial heterogeneity, we consider the predictive value of a velocity vector with respect to its surrounding pixels. We describe this with the conditional entropy of the field given knowledge about its direct neighbourhood. To this end, we employ the conditional probability density function of a specific velocity vector at a certain location (described by random variable V_1) given a neighboring velocity vector (V_2):

$$\begin{aligned} H(V_2|V_1) &= \int \mathrm{P}(\vec{v}_1, \vec{v}_2) \log \frac{\mathrm{P}(\vec{v}_1)}{\mathrm{P}(\vec{v}_1, \vec{v}_2)} d\vec{v}_1 d\vec{v}_2 \\ &= \int \mathrm{P}(\vec{v}_2|\vec{v}_1)\mathrm{P}(\vec{v}_1) \log \frac{\mathrm{P}(\vec{v}_1)}{\mathrm{P}(\vec{v}_2|\vec{v}_1)\mathrm{P}(\vec{v}_1)} d\vec{v}_1 d\vec{v}_2 \\ &= -\int \mathrm{P}(\vec{v}_1) \int \mathrm{P}(\vec{v}_2|\vec{v}_1) \log \mathrm{P}(\vec{v}_2|\vec{v}_1) d\vec{v}_2 d\vec{v}_1. \end{aligned} \tag{3.12}$$

The conditional entropy $H(V_2|V_1)$ is equal to zero if V_1 is completely determined by V_2.

Again, the true probability density functions are inherently unknown. Hence, we compute their discrete probability mass function estimates $\tilde{\mathrm{P}}(V_1 \in \mathrm{bin}\{i,j\})$ and $\tilde{\mathrm{P}}(V_2 \in \mathrm{bin}\{k,l\}|V_1 \in \mathrm{bin}\{i,j\})$ according to (3.9), using the data obtained within a circular kernel of radius K based on two-dimensional histograms. Similarly, the conditional probability distribution can be estimated as:

$$\begin{aligned} \tilde{\mathrm{P}}(k,l|i,j) &= \tilde{\mathrm{P}}(V_2 \in \mathrm{bin}\{k,l\}|V_1 \in \mathrm{bin}\{i,j\}) \\ &= \frac{\frac{1}{|\mathcal{S}_k|} \sum_{m \in \mathcal{S}_K} \frac{1}{|\mathcal{S}_m|} \sum_{n \in \mathcal{S}_m} c(\vec{v}_m, i, j) c(\vec{v}_n, k, l)}{\frac{1}{|\mathcal{S}_k|} \sum_{m \in \mathcal{S}_K} c(\vec{v}_m, i, j)}, \end{aligned} \tag{3.13}$$

where $\mathcal{S}_m$ is the set of indices that point to the velocity vectors that lie adjacent to the m^{th} velocity vector. The conditional entropy is then calculated as:

$$\hat{H}(V_2|V_1) = \sum_{i,j} \tilde{\mathrm{P}}(i,j) \sum_{k,l} \tilde{\mathrm{P}}(k,l|i,j) \log \tilde{\mathrm{P}}(k,l|i,j). \tag{3.14}$$

The analysis is repeated by sliding the circular kernel across the entire vector field in order to generate parametric maps of $\hat{H}(V)$ and $\hat{H}(V_2|V_1)$.

An illustrative overview of the described methodology is shown in Figure 3.1.

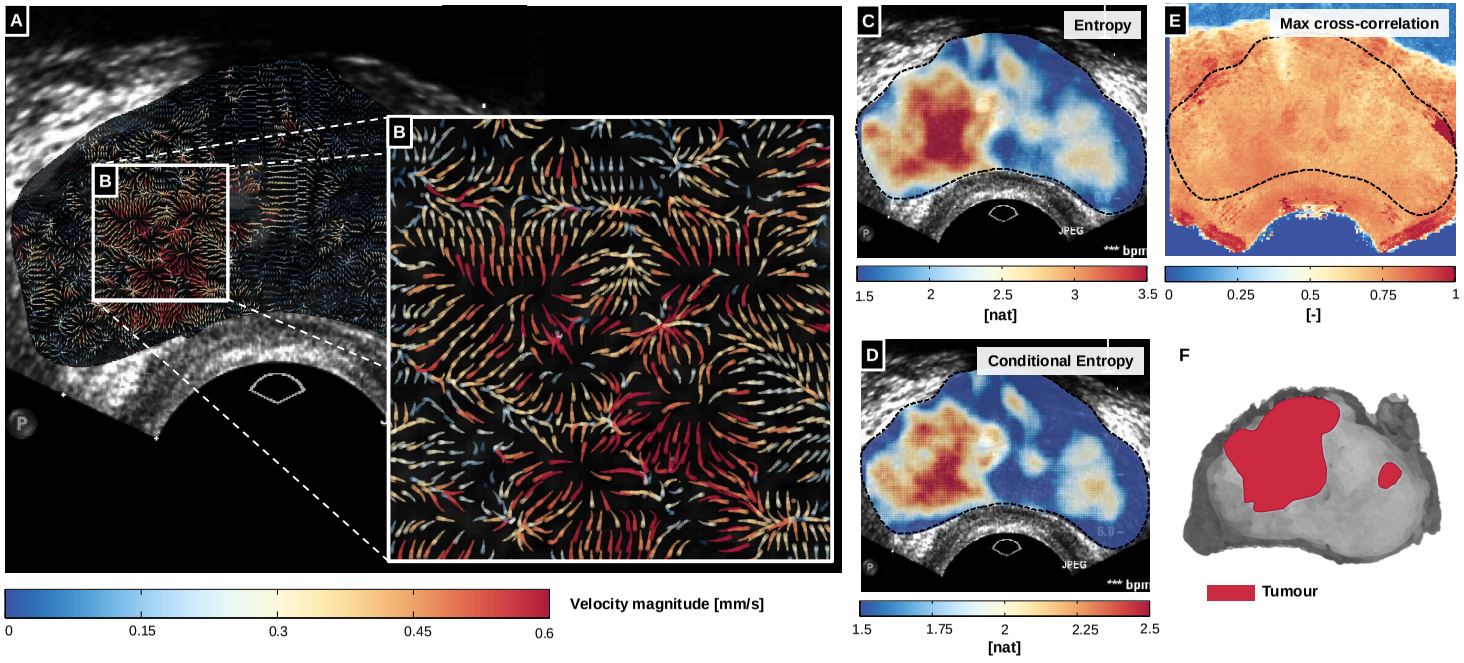

Figure 3.2: An example of the estimated ultrasound-contrast-agent velocity fields (A, zoom B), as well as the parametric maps resulting from the statical characterization using Entropy (C) and Conditional Entropy (D). Image values are given in nats (natural unit of information). To provide a measure of confidence in the time-delay estimation procedure, a map of the maximum normalized cross-correlation values is shown in (E). The corresponding histology slice is also given (F). Tumour lesions are marked in red.

3.3 Validation Methodology

The proposed method was clinically validated on a group of twenty-four patients, of which fifty-seven DCE-US planes were included. Contrast-mode as well as fundamental-mode loops were simultaneously recorded for each plane. Additional fundamental-mode US sweeps were recorded from the prostate's base to apex for each patient. These served as a reference for manual identification of the DCE-US plane location within the full prostate volume using the anatomical features captured by the fundamental mode images. Then, cognitive registration between the histopathological set of slices with marked lesions and the DCE-US planes permitted drawing regions of interest (ROIs) of approximately 0.5 cm^2 indicating either benign (Gleason score $< 3 + 3 = 6$) or malignant areas. For this purpose, fundamental mode (B-mode) sweep videos ranging from base to apex where acquired. By comparing this video with the fundamental mode image obtained in the contrast imaging plane, the contrast imaging plane location was determined. Then the corresponding histology slice was chosen.

To mitigate errors in the registration procedure, slices with small tumours (with respect to the ROIs) and inconsistencies across multiple slices were not considered suitable for drawing malignant ROIs. In total, fifty-two benign regions and fifty-tree malignant ROIs were selected. On average, these ROIs included about 2000 time-intensity curves (min: 308, max: 6695), and were drawn prior to the development of the methods presented in this work.

A Receiver-Operating-Characteristic (ROC) analysis was adopted to evaluate classification performance: Pixel-based classification was performed using a variable threshold per parameter, thereby displaying the relation between sensitivity and specificity in a curve. The area under the ROC curve is used as a general measure of flexibility and performance. The optimal classification threshold is a trade-off between sensitivity and specificity, and was determined by selecting the point on the ROC curve that yields the minimum Euclidean distance to ideal classification, *i.e.* to a sensitivity and specificity of 1. The method's sensitivity, specificity, positive predictive value, and negative predictive value were calculated for this threshold.

The adopted algorithm settings are given in Table 3.1. The number of pixels in the ring kernel for velocity estimation N was set to 8; a trade-off between inter-pixel spacing (related to the system resolution) and least-squares estimation variance. The entropy kernel radius K was set to 3.6 mm, being a trade-off between the accuracy of the probability density estimates and the achieved spatial resolution of the parametric

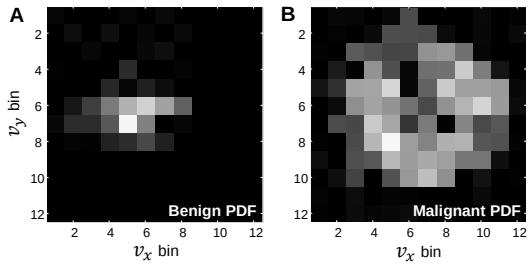

Figure 3.3: Typical probability density function estimates of velocity fields from benign (A) and malignant (B) regions.

Table 3.1: Adopted settings for the proposed algorithm. Values between brackets indicate the set of tested parameters.

Parameter	Description	Value
N	Pixels in set of velocity estimation	8
K	Kernel radius for entropy analysis	3.6 mm
v_{max}	Maximum histogram bin velocity	1 mm/s
R	Radius circle for velocity estimation	{0.7,0.9,1.2} mm
N_b	Histogram bins	{9,12,15}

maps. v_{max} was set to 1 mm/s, in line with the expected blood velocities in human capillaries.[111] The method's performance was assessed for 3 different radii of the velocity estimation kernel R, and varying number histogram bins.

The pixel-wise signal quality was assessed by estimating the Signal to Noise Ratio (SNR). The signal component $s[n]$ was estimated by filtering the TIC with a moving median filter (window size of 4 seconds) and subtracting the baseline, which was estimated by calculating the median value in the first 5 seconds of the TIC. The noise component $u[n]$ was estimated by subtracting the filtered TIC from the raw TIC. A measure of SNR in dB is then calculated as:

$$\text{SNR} = 10\log_{10}\left(\frac{\sum_n s[n]^2}{\sum_n (u[n]-\bar{u})^2}\right), \tag{3.15}$$

where $\bar{u}$ is the mean value of u across all samples.

The classification performance of the proposed methods was compared to that obtained with different DCE-US quantification parameters reported in the literature. To this end, the spatiotemporal correlation (r),[72] wash-in time (WIT),[140] wash-in rate (WIR), peak intensity (PI), and area under the IDC (AUC) were also extracted. To facilitate a robust estimation process, the Local Density Random Walk model was fitted to the curves according to[71], after which the desired parameters could be derived.

Additionally, a comparison amongst heterogeneity-based measures was made by evaluating the classification performance obtained by estimating the entropy of the other quantification parameters based on a univariate version of the methods described in Sec. 3.2f

To achieve similar spatial smoothing as the kernel-based entropy analysis, the single-pixel parameters were post-filtered using a 2D Gaussian kernel (standard deviation of 1.3 mm, half the entropy kernel radius).

Finally, the p-values for testing the hypothesis that there is a difference between the parameter means for benign and malignant areas were calculated. Since some of the parameter distributions are heavily skewed and do not follow a normal distribution, a non-parametric Kruskal-Wallis test (one-way ANOVA on ranks) was adopted for this purpose.[141] Taking into account the spatial correlation between parameter values within a ROI, the number of independent samples in a distribution was conservatively set to the number of ROIs used for that distribution.

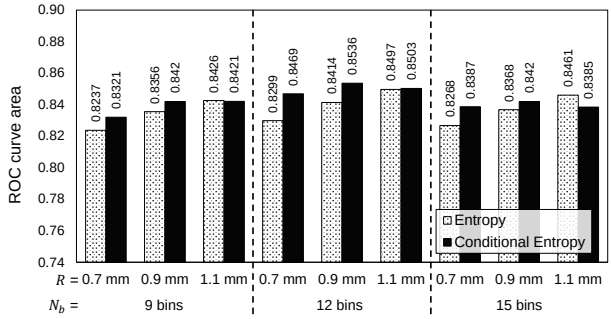

Figure 3.4: Description of performance in terms of Receiver-Operating-Characteristics curve area (range 0-1), as a function of algorithm settings. Blue dotted bars indicate the performance for Entropy, yellow bars give the performance for Conditional Entropy.

3.4 Results

Figure 3.2 shows a qualitative example of the obtained velocity fields, along with the parametric maps of its Entropy and Conditional Entropy. In addition, the maximum normalized cross-correlation value (i.e. weight, see Eqn. (3.7)) is given for each pixel, serving as a measure of confidence in the velocity estimate. The corresponding histology slice is also shown. One can observe that both parameters display elevated values in areas with marked tumour lesions.

Figure 3.3 shows two typical examples of the probability density function estimates of the velocity fields within a kernel from a benign and malignant region. One can observe a broad distribution of velocity vectors in the malignant case, resulting in a high entropy.

Figure 3.4 displays the attained ROC curve areas for the velocity field Entropy as well as the velocity field Conditional Entropy as a function of the radius R and the number of histogram bins N_b. The adopted settings are summarized in Table 3.1. One can observe that the highest ROC curve area is reached with R = 1.1 mm and N_b = 12 for Entropy, and R = 0.9 mm and N_b = 12 for Conditional Entropy. For the remainder of the results, the adopted settings are R = 0.9 mm and N_b = 12, unless explicitly mentioned otherwise.

Figure 3.5 demonstrates the relation between the achieved ROC curve areas of the proposed methods and measurement quality in terms of SNR. Performance monotonically increases when excluding pixels from the ROIs based on SNR. As a consequence, the number of independent samples decreases. To provide an indication of this reduction in data, the amount of benign and malignant ROIs that preserve over 50% of their pixels after exclusion is also plotted.

The histograms and box-plots of the benign and malignant classes for velocity field Entropy and Conditional Entropy are given in Figure 3.6. The malignant class distribution displays higher median values for both parameters. Moreover, the box-plots indicate that the 25th percentile ($Q1$) of the malignant distribution is higher than the 75th percentile ($Q3$) of the benign distribution for both parameters. Values are depicted as outliers if they are larger than $Q3 + 1.5(Q3 - Q1)$ or smaller than $Q1 - 1.5(Q3 - Q1)$. A pixel was classified malignant for Entropy > 2.47 and Conditional Entropy > 1.91.

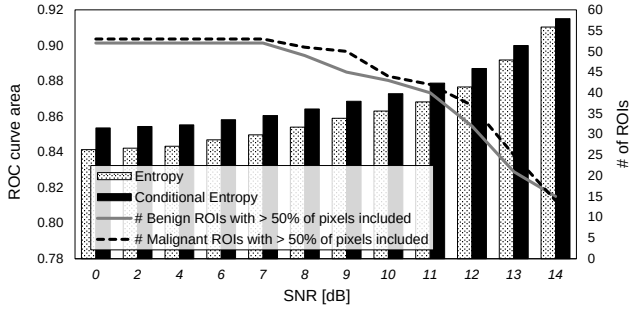

Figure 3.5: Description of performance in terms of Receiver-Operating-Characteristics curve area, as a function of SNR threshold. Blue dotted bars indicate the performance for Entropy, yellow bars give the performance for Conditional Entropy. The amount of benign and malignant ROIs that preserve over 50% of their pixels after applying the SNR threshold are given by the solid grey and dashed black lines, respectively.

In Figure 3.7, two typical parametric maps of velocity-field Conditional Entropy are shown together with their binary classification maps obtained by applying the histogram-based optimal threshold. The adopted benign and malignant ROIs are displayed, as well as the resulting classification performance within the ROIs as described in Sec. 3.3. For comparison the corresponding parametric maps of AUC, PI, WIR and WIT are also given.

Figure 3.8 shows the ROC curves for velocity field Entropy and Conditional Entropy along with those obtained using other entropy and non-entropy based DCE-US quantification methods. The classification characteristics of Conditional Entropy generally yield higher specificities, whereas Entropy tends to result in higher sensitivities. Both methods outperform the reference quantification methods.

The pixel-based classification results are summarized in Table **??**, where the settings that yield the highest ROC curve area for velocity field Entropy and Conditional Entropy (see Figure 3.4) are used. Of all evaluated parameters, Conditional Entropy yields the highest ROC curve area. The difference with respect to Entropy is however small. The AUC yields the lowest ROC curve area, and the lowest values of sensitivity, specificity, negative predictive value, and positive predictive value. These statistics are always the highest for either Entropy or Conditional Entropy.

In addition to this, the results for ROI-based classification are presented in Table **??**, by taking the mean value of each parameter in the ROI. The highest sensitivity, specificity, negative predictive value and positive predictive value are reached by the Conditional Entropy of the velocity fields.

Table 3.2: Pixel-based classification performance in terms of sensitivity (SEN), specificity (SPC), negative predictive value (NPV), positive predictive value (PPV), and Receiver-Operating-Characteristics (ROC) curve area. For both Entropy [$H(V)$] and Conditional Entropy [$H(V_2|V_1)$], the results with settings that yield the highest ROC curve area (see Figure 3.4) are given. As a reference, other relevant parameters for DCE-US quantification proposed in the literature are also given, along with their spatial heterogeneity based on entropy.

Parameter	**SEN [%]**	**SPC [%]**	**NPV [%]**	**PPV [%]**	**ROC curve area**	**p-value**
Entropy $H(V)$	79.8	78.4	79.5	78.7	0.849	$\ll 0.01$
Conditional Entropy $H(V_2\|V_1)$	77.9	78.9	78.1	78.7	0.854	$\ll 0.01$
Spatiotemporal correlation r	68.6	74.5	70.4	72.9	0.763	$\ll 0.01$
Wash-in time	69.2	74.1	70.6	72.7	0.786	$\ll 0.01$
Wash-in rate	68.5	74.3	70.2	72.7	0.759	$\ll 0.01$
Peak-intensity	60.5	65.7	62.4	63.8	0.682	$\ll 0.01$
AUC	59.7	43.1	51.7	51.2	0.513	0.58
Entropy of spatiotemporal correlation r	47.8	62.1	54.3	55.8	0.522	0.63
Entropy of wash-in time	72.1	76.7	73.3	75.5	0.816	$\ll 0.01$
Entropy of wash-in rate	59.0	67.2	62.1	64.3	0.646	$\ll 0.01$
Entropy of Peak-intensity	50.8	60.4	55.1	56.2	0.549	0.23
Entropy of AUC	60.6	58.6	59.8	59.4	0.590	0.09

Table 3.3: Region-based classification performance in terms of sensitivity (SEN), specificity (SPC), negative predictive value (NPV) and positive predictive value (PPV) are given for the optimal threshold. The true positives (TP), true negatives (TN), false positives (FP) and false negatives (FN) are also shown, along with the overall accuracy.

Parameter	**SEN [%]**	**SPC [%]**	**NPV [%]**	**PPV [%]**	**TP**	**TN**	**FP**	**FN**	**Accuracy [%]**
Entropy $H(V)$	81	79	80	80	43	41	11	10	80
Conditional Entropy $H(V_2\|V_1)$	81	83	81	83	43	43	9	10	82
Spatiotemporal correlation r	64	83	69	68	34	43	9	19	73
Wash-in time	70	79	72	77	37	41	11	16	74
Wash-in rate	72	65	69	68	38	34	18	15	69
Peak-intensity	62	62	62	62	33	32	20	20	62
AUC	49	62	54	57	26	32	20	27	55
Entropy of spatiotemporal correlation r	49	67	57	61	26	35	17	27	58
Entropy of wash-in time	76	83	77	82	40	43	9	13	79
Entropy of wash-in rate	62	65	63	65	33	34	18	20	64
Entropy of Peak-intensity	45	73	57	63	24	38	14	29	59
Entropy of AUC	66	60	63	63	35	31	21	18	63

3.5 Conclusions and Discussion

In this paper, we presented a method for the estimation and statistical characterization of flow vector fields from clinically acquired DCE-US data. By employing time-delay estimation in combination with least squares minimization, the proposed method enables estimation of the in-plane flow vector fields of perfused microvasculature, after which histogram-based measures of heterogeneity are extracted: the vector field's Entropy and Conditional Entropy.

Both Entropy and Conditional Entropy estimates yielded higher values in malignant areas. The typical examples of benign and malignant probability density functions shown in Figure 3.3 indeed display a broader distribution of velocity vectors for the malignant case. Qualitatively, this can also be observed from Figure 3.2, where an example of the obtained flow vector fields is shown for one DCE-US plane. The complexity of the flow patterns is noticeable in the area corresponding to the tumour location. Moreover, one can recognize multiple field "sources" and "sinks". We hypothesize that these coincide with feeding and draining vessels that enter the imaging plane and perfuse the area through the microvasculature. The Entropy and Conditional Entropy of the fields both display elevated values in malignant regions; a finding that is confirmed by the quantitative analysis. When trialled on a set of 24 patients, Entropy and Conditional Entropy are significantly higher in malignant pixels as compared to benign pixels ($p \ll 0.01$). Presuming that these features reflect the heterogeneity of contrast-agent flow patterns, this result is in line with previous observations on the heterogeneous nature of blood flow in tumours.[85]

The pixel-based classification performance for detecting prostate cancer was expressed in terms of the ROC curve area. On the entire dataset, the proposed parameters outperformed all other evaluated DCE-US features, and both resulted in a ROC curve area of approximately 0.85. Spatiotemporal correlation, WIR and WIT yielded lower performances (ROC curve areas of 0.76, 0.76, and 0.79, respectively), followed by the amplitude-based peak-intensity (ROC curve area of 0.68) and area under the IDC (ROC curve area of 0.51). The latter aims to reflect the level of perfusion based on the IDC integral, but is hampered by the ambiguity between blood fractional volume and velocity, as well as by the dependency on ultrasound pressure and attenuation.

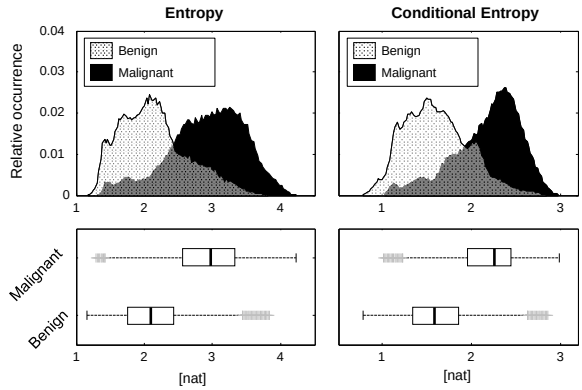

Figure 3.6: The benign (blue dotted) and malignant (yellow) class histograms for Entropy and Conditional Entropy (R = 0.9 mm, N_b = 12 bins). A pixel was classified malignant for Entropy > 2.47 and Conditional Entropy > 1.91. The corresponding boxplots for both classes are also given. Outliers are indicted with yellow crosses.

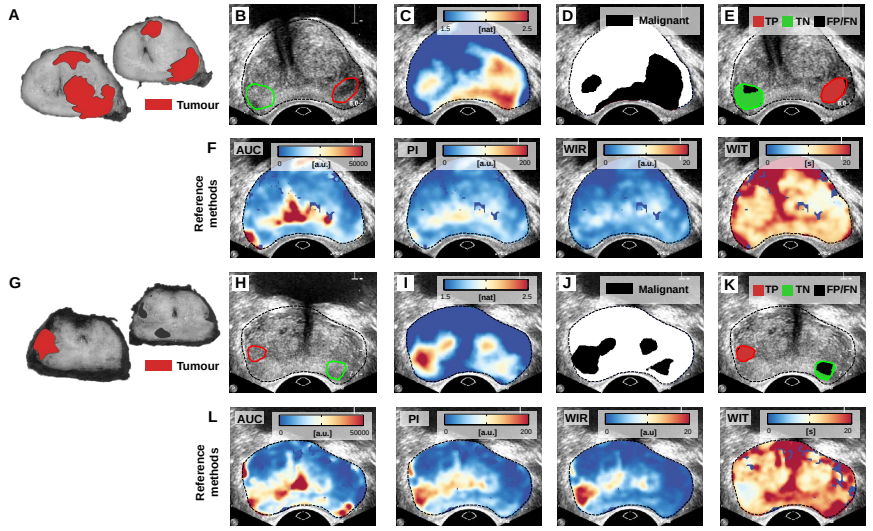

Figure 3.7: Two examples of benign and malignant regions of interest (ROIs, as defined in section 3.3) drawn on the fundamental mode images (B,H), along with the nearest histology slices (A,G). The maps of conditional entropy for these imaging planes are shown in (C,I). Classification results using the pixel-based optimal threshold are given in (D,J) for the full field of view. Finally, the true positives (green), true negatives (red), and false positives/negatives (black) are shown in (E,K). As a reference, the maps of area under the IDC (AUC), peak-intensity (PI), wash-in time (WIT), and wash-in rate (WIR) for these imaging planes are given in (F,L).

In this work, assessment of heterogeneity of flow was proposed by calculating the entropy of UCA velocity fields. In addition, we evaluated the entropy of other DCE-US features. Of these, only WIT entropy and WIR entropy display a significant ($p < 0.05$) difference between malignant and benign pixels. As expected, the mean WIR entropy was indeed higher for malignant pixels, since WIR is proportional to flow. Its classification performance is limited however (sensitivity and specificity of 62.3% and 65.4%, respectively). On the other hand, the mean WIT entropy is significantly lower for the malignant distribution, reaching a test sensitivity and specificity of 72.1% and 76.7%, respectively (see Table **??**). This observed local similarity in wash-in times may be a direct consequence of the inverse proportionality of WIT to flow velocity: heterogeneities in flow cause reduced variations in WIT for high flows.

Interestingly, pixel-based classification performance of velocity field Entropy and Conditional Entropy monotonically increases when excluding pixels that suffer from a low signal to noise ratio (SNR). This most likely leads to exclusion of wrongly estimated velocity vectors, as estimation of time-delays between IDCs becomes increasingly difficult for higher noise levels. Therefore, the development of a time-delay estimation procedure that is more robust in the presence of the low SNR conditions observed in DCE-US measurements is part of future work. In line with this, dedicated maximum likelihood estimators based on the particular noise statistics of DCE-US (Rayleigh distribution) may be exploited.

The frame rate of the imaging system plays a primordial role in the estimation of time-delays. In this work, the selected rate of 10 Hz was sufficient to reach the required

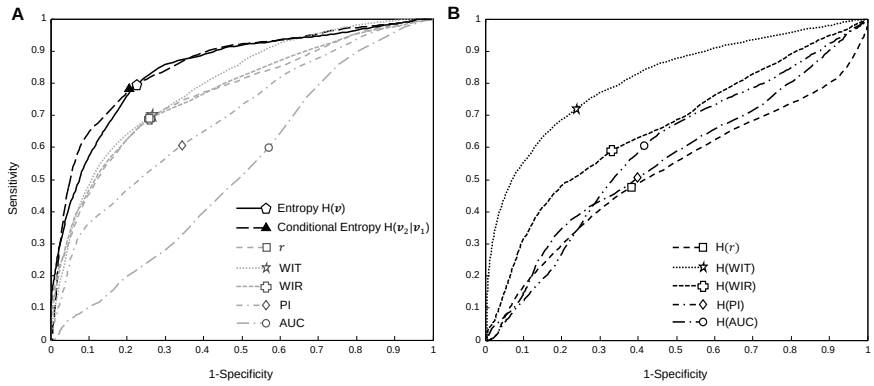

Figure 3.8: Receiver-Operating-Characteristic (ROC) curves for the classification performance of the proposed Entropy [$H(\vec{v})$] and Conditional Entropy [$H(\vec{v}_2|\vec{v}_1)$] of velocity fields (R = 0.9 mm, N_b = 12 bins), against those obtained with spatio-temporal IDC correlation (r), wash-in time (WIT), wash-in rate (WIR), peak intensity (PI) and the area under the IDC (AUC) as parameters (A). The ROC curves obtained when using the entropy [$H(\cdot)$] of these parameters are shown in (B).

velocity resolution for the Entropy analysis: the histogram bin width (0.167 mm/s). The latter is approximately equal to the error standard deviation of the estimated velocity magnitudes obtained in the *in-silico* validation (Appendix 2.8).

The Entropy and Conditional Entropy are determined by estimating the probability distributions of the vector fields using bivariate histograms. The histogram estimator approximates the true density from the data using rectangular bins. The probability for a value to fall within such a bin is calculated based on the incidence of these values in the dataset. The larger the dataset (kernel size) on which the density is estimated, the higher the accuracy of this probability estimate. As a consequence, the spatial resolution of the analysis decreases. The required amount of samples depends on the amount of histogram bins. Choosing a smaller number of bins requires less samples to effectively fill those bins, but deteriorates the resolution of the histogram. This realization touches upon a fundamental trade-off. In our test set, the highest ROC curve area was attained using 12 bins in both directions.

An alternative to the histogram estimator is the kernel density estimator.[142] In this case, the probability distribution is represented by a mixture of kernels (e.g., a Gaussian) that have a certain adjustable bandwidth. Although this approach can yield a smooth estimate of the density function, it is computationally more demanding. The methodology presented in the present paper requires estimating one probability distribution per pixel for Entropy, and N_b^2 probability distributions per pixel for Conditional Entropy. Hence, we chose to employ the fast histogram estimator as opposed to the kernel density estimator.

The validity of the results presented in this work is hampered by the limitations of the quantitative validation procedure. First of all, histological assessment of Haematoxylin & Eosin stained prostate specimens is based on the level of cell-differentiation, whereas the developed methods are aimed at detecting angiogenesis. Hence, not all malignantly labelled time-intensity curves are necessarily obtained from angiogenic vasculature. It would therefore be interesting to validate the methods presented in this work with stains

of the endothelial marker CD31, or the angiogenesis-stimulating vascular endothelial growth factor (VEGF). Secondly, the registration procedure has some pitfalls. The ultrasound imaging planes are in general not parallel to the histology slices, as specific pathological guidelines constrain the dissection procedure. Finally, the performance is biased towards large tumours and those that are consistent through multiple slices. This is a consequence of the infeasibility of drawing reliable regions-of-interest for small and scattered tumours, given the adopted registration procedure.

The adopted time-delay estimator relies on the assumption that IDCs show a strong local similarity in shape. Violations of this assumption impact the estimation accuracy. In case of high local bolus dispersion or diffusion, a model-based transit time estimator that incorporates the IDC shape alteration (e.g. the local density random walk model) may be employed.[143]

The velocity field estimator described in (3.5) uses the time-delay estimates obtained at a set of pixels to infer a local dominant propagation vector. As such, the attained velocity vector represents the macroscopic contribution of flows originating from all vessels in the final resolution cell. To test the performance of the estimator given such macroscopically measured flows, we performed a simple *in-silico* experiment, in which the propagation of a UCA bolus through an intermediately sized branching structure was simulated. The introduction of random walk motion in this propagation model facilitated the generation of microscopic UCA particle trajectories, that lead to macroscopic bolus dispersion. Although this simple experiment yielded promising results, its performance on a physiologically more realistic model (*in-silico* or *in-vitro*) of flow trough the capillary network of a tumour could be studied as a topic of future work. Given such a model, an extensive validation of the proposed entropy measures may be performed.

The presented method is applied to 2D DCE-US data. Hence, out of plane flows affect the velocity estimates and lead to an ambiguity between the elevational orientation and magnitude of the velocity vector. In fact, the lateral and axial velocity vector components are the projections of the true 3D velocity vector onto the imaging plane. With this in mind, heterogeneity in the elevational component of this vector within the kernel would be reflected by its estimated magnitude. As a result, it would contribute to the estimated Entropy.

Recently, 4D DCE-US imaging systems have been introduced. Such systems facilitate the acquisition of 3D volumes over time and hence permit an analysis that incorporates the full 3D spatial information.[121] One can envisage computing 3D velocity vector fields by performing the time-delay estimation procedure on a set of voxels that are distributed in 3D space. The spatial entropy analysis can then be implemented based on a spherical kernel in combination with trivariate probability density estimation. The added dimension comes at the price of a reduced frame rate of the ultrasound data, which impairs the temporal resolution of the cross-correlation based delay estimator employed in this paper. Nevertheless, contrast-agent bolus injections produce time intensity curves that contain dominantly low frequency content (< 0.5 Hz).[121] Hence the required phase information is retained, even at the low frame rates achieved by 4D systems. The extension of the proposed method to 4D DCE-US, along with the development of algorithms that provide high-resolution time-delay estimation in these systems, will be part of future work. Additionally, the possibility of staging the severity of lesions in terms of the Gleason grade can be investigated.

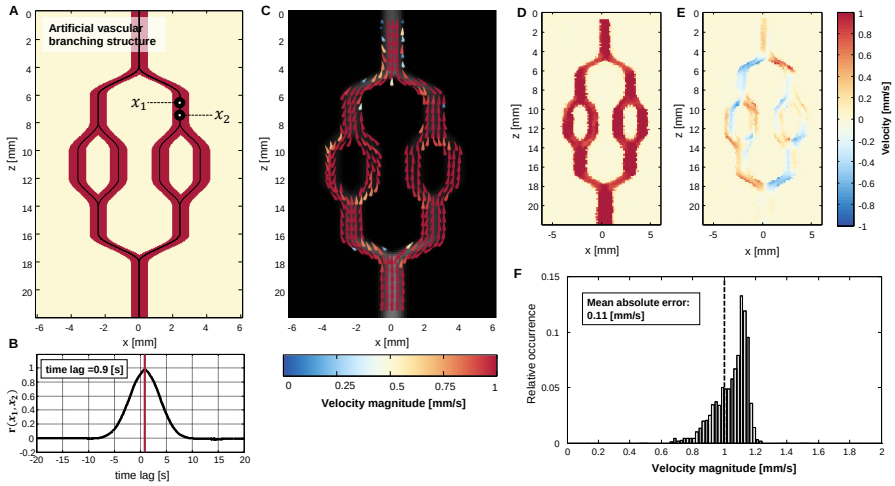

Figure 3.9: *In-silico* validation of velocity vector field estimation. The artificial branching structure is shown (A), along with the cross correlation function of the time-intensity curves obtained at two locations x_1 and x_2 (B). The estimated velocity vector field mapped on the maximum intensity projection is given in (C). The axial and lateral velocity components are shown in (D) and (E), respectively. A histogram of the obtained velocity magnitude estimates within the structure is given in (F).

The proposed time-delay based approach can be applied to DCE-US recordings of any perfused organ to resolve flow patterns with magnitudes that can be well below 1 mm/s, such as those found in tumour arterioles and capillaries[144]. As such, this provides a key advantage with respect speckle-tracking based methods, which are designed to image the relatively high flows found in arteries and the heart, and suffer from the severe speckle decorrelation that results from UCAs moving through the microvasculature as opposed to a large blood pool.

3.6 Appendix: In-silico validation of vector fields

In this section, the vector velocity field estimator is validated using an *in-silico* experiment in which the 2D transport of particles (microbubbles) through an artificial branching (vascular) structure was simulated. For this purpose, particles were propagated through the structure with a given velocity, comprising a deterministic flow plus an additional Gaussian process noise component. The former simulates pure convection, whereas the latter served as a model for diffusion. Particles were bound to stay within 0.5 mm of the central axis (vessel radius). The amount of particles was 2000. The velocity magnitude was set to 1 mm/s.

The ultrasound acquisition of this process was simulated by modelling the scanner's point spread function as a bivariate Gaussian, with standard deviations that are dependent on the axial (0.156 mm) and lateral ($0.142 + 0.0054 \times z$ mm) resolution, where z is the imaging depth. These numbers are selected based on measurements of the speckle-grain dimensions as a function of imaging depth for the C10-3v transrectal

endfiring ultrasound probe in combination with the Philips iU22 scanner.[88] The frame rate was set to 10 Hz, and the pixel spacing was 0.15 mm.

The velocity vector fields were estimated according to the procedure described in section 3.2e. The adopted values for N and R are 8 and 0.5 mm, respectively. Figure 3.9 displays the observed maximum intensities of all the ultrasound time-intensity curves (maximum intensity projection) along with the velocity vector estimates in pixels with a peak-intensity greater than 10% of the maximum intensity. The estimated velocities in both the axial and lateral direction as well as the histogram of velocity magnitudes within the branching structure are also given. The mean absolute error of the velocity magnitudes is 0.11 mm/s, and the standard deviation of the error is 0.17 mm/s.

3.7 Acknowledgements

This work is part of the research programme 10769, which is partly financed by the Netherlands Organization for Scientific Research (NWO). The research has also received funding from the European Research Council / ERC grant agreement n. 280209.

4

In-vivo contrast-enhanced ultrasound tractography

Abstract - *Diffusion tensor tractography (DTT) enables visualization of fibre trajectories in soft tissue using magnetic resonance imaging.[145] DTT exploits the anisotropic nature of water diffusion in fibrous structures to identify diffusion pathways by generating streamlines based on the principal diffusion vector.[146] Anomalies in these pathways can be linked to neural deficits.[147,148] In a different field, contrast-enhanced ultrasound is used to assess anomalies in blood flow with the aim of locating cancer-induced angiogenesis.[71,149,150] Like water diffusion, blood flow and the movement of contrast agents will also have a principal direction that is however now dictated by the local vasculature. Here we show how the tractographic techniques developed for magnetic resonance imaging DTT can be translated to contrast-enhanced ultrasound, by first estimating contrast flow velocity fields from contrast-enhanced ultrasound acquisitions, and then applying tractography. We performed 4D in-vivo contrast-enhanced ultrasound of human prostates, and found that the proposed approach can be directly applied to clinically acquired datasets. By comparing the results to histopathology after prostate resection, we observed that the contrast flow tracts qualitatively display typical markers of cancer angiogenic microvasculature: higher densities and tortuous geometries in tumour areas.[151] The method can be used in-vivo using a standard contrast-enhanced ultrasound protocol, opening up new possibilities in the area of vascular characterization.*

From: R.J.G. van Sloun, L. Demi, S.G. Schalk, C. Caresio, J. Huang, J. Li, A.W. Postema, C. Mannaerts, F. Molinari, J.C. van der Linden, P. Huang, H. Wijkstra, and M. Mischi,"In-vivo contrast-enhanced ultrasound tractography", *Submitted*, 2017

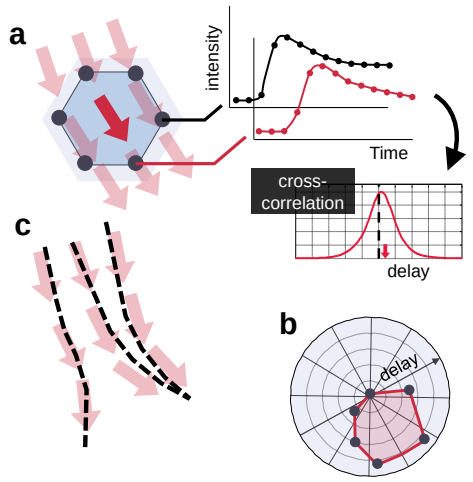

Figure 4.1: Principle of CEUS-T a. Time-delay estimation amongst a set of time-intensity curves. b. Time-delay magnitude as a function of orientation. c. Velocity vector estimation and tractography.

4.1 Introduction

The introduction of diffusion tensor tractography (DTT) in magnetic resonance imaging (MRI) led to numerous new studies in brain research.[152] It was the first non-invasive *in-vivo* imaging modality enabling the generation of white matter fibre trajectories in soft fibrous tissues, such as nerves and muscles.[145] Relevant information about neural network connectivity, white matter deficits and tumour infiltration are now all available through DTT. The method has widespread potential implications in both cognitive neuroscience and neurobiology.[147,148] At the core of DTT lies the anisotropic nature of water diffusion in white matter. Water molecules have a preferred direction of diffusion in fibrous structures, a directionality that can be tracked and displayed with streamlines.[146] As such, DTT became a widely used technique to visualize white matter axons in the brain. In this work, we translate these tractographic technologies to contrast-enhanced ultrasound (CEUS), which has now advanced to the level that it permits 4D (3D space + time) acquisitions of contrast agent concentration. Where DTT MRI is used to visualize white matter axons, CEUS tractography will be employed to visualize vascular structures.

In CEUS, the passage of an intravenously injected bolus of ultrasound contrast agent through an organ is recorded with an ultrasound imaging system.[57] These lipid-shelled microbubbles have a size similar to red blood cells and therefore remain intravascular while reaching the smallest capillaries in the vascular net. CEUS has been adopted in clinical practice with applications ranging from cardiology to oncology. For the latter, clinicians mainly rely on qualitative inspection of the ultrasound videos,[62] searching for visual clues such as early contrast enhancement. Although recent developments in quantitative interpretation of CEUS videos have shown promise,[71,150,153] a technique that provides explicit information on the underlying vascular architecture using standard clinical CEUS protocols is still hampered by the resolution limits of clinical ultrasound scanners.

Current methods for direct *in-vivo* vascular imaging using CEUS are indeed challenging

to fit into clinical protocols. If one extends beyond the regular protocols and permits longer acquisition times, a recently proposed technique named ultrafast ultrasound localization microscopy[154] can be considered. This approach visualizes the microvascular architecture with astonishing resolution by borrowing concepts from photo-activated localization microscopy.[155] However, super-localization technologies remain highly sensitive to motion artifacts, complicating their clinical application. Moreover, their 3D implementation is currently restricted by data overload as well as challenging probe design and electronics.[156] Another ultrasound-based approach for microvascular imaging is acoustic angiography.[157] It embraces the high frequency content generated by resonating microbubbles to reach resolutions that can resolve vessels with a diameter of around 150 μm. While these high frequencies are an asset for achieving a high spatial resolution, they are also the method's main drawback: Penetration depth is limited as acoustic absorption by tissue strongly increases with frequency. Moreover, its peculiar imaging strategy requires the use of very broad-banded ultrasound transducers ($\approx$ 2 to 45 MHz) or specially designed dual-frequency probes.

Here, we propose contrast-enhanced ultrasound tractography (CEUS-T), which combines revolutionary concepts from DTT MRI for fibre visualization with CEUS blood flow vector imaging,[150] yielding 3D images of contrast agent trajectories. The analogy with DTT MRI is clear: as with diffusion of water molecules in fibres, microbubbles move through an organ with a directionality that is now dictated by the vascular architecture. CEUS-T was performed *in-vivo*, using 4D CEUS recordings of the human prostate obtained in a clinical setting, with a clinically approved ultrasound system (LOGIC E9, GE Healthcare, Wauwatosa, WI, USA) and ultrasound contrast agents (SonoVue ®, Bracco, Milan, Italy).

4.2 Methods

At the core of CEUS-T lies the estimation of flow vector fields from 4D CEUS. The low volume rates obtained with standard 4D CEUS, typically even below one volume per second, pose a major problem for standard velocity vector imaging based on speckle tracking or optical flow.[158] Severe spatial de-correlation can be expected within one frame. While the temporal resolution is hence not sufficient to track microbubbles over space, it is sufficiently high to capture the dynamics of a diffused cloud of microbubbles.[121] As such, all the required phase information to determine the bolus transit time from one point in space to another point in space is retained. The usefulness of this property becomes evident when comparing the transit times, or time-delays, amongst the contrast time-intensity curves obtained at a spatially distributed set of voxels surrounding the location of interest. The relation between this specific set of curves can be visualized in an orientation distribution function[159] (Fig. 1a-b), reflecting the dominant flow directivity.[150]

To achieve an accurate estimate with a sufficiently high temporal resolution, we first increase the sample rate of the time signals using Sinc-interpolation.[160] As the dominant bandwidth of the contrast agent evolution over time is mostly below the Nyquist frequency in the prostate,[121] this approach allows near-perfect reconstruction of the true signal values at the interpolated sample-points. The time-lag that maximizes the cross correlation function between two time-intensity curves serves as an estimate of

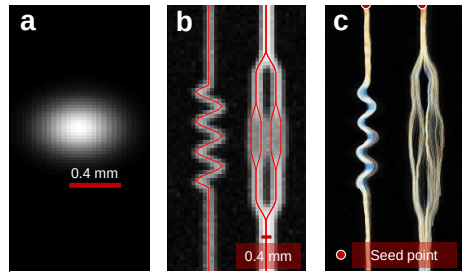

Figure 4.2: 2D CEUS-T on synthetic data a. The adopted imaging point spread function. b. Maximum echo intensity for a simulation of contrast agent transport through an artificial branching structure (red lines) c. Multiple streamlines originating from indicated seed points.

the time-delay. This procedure allows for a very simple, yet effective high resolution time-delay estimate from low volume-rate 4D CEUS.

We estimate the time-delays amongst a set of 113 curves at over 6 million locations in the volume, accounting for more than 600 million evaluations of this procedure. For each of those 6 million voxels in the 3D volume, a delay-orientation distribution function can be generated. The dominant flow orientation and magnitude is then obtained by minimizing the squared error between a model-prediction of the time-delays given a velocity vector, and the measured time-delays.[150] This facilitates the estimation of a 3D velocity field of microbubble propagation through the organ.

After generating the full 3D representation of propagation directions, we exploit tractography[161] to visualise flow trajectories. As for DTT, this translates into solving the differential equation that describes the movement of a particle within the estimated vector fields, given an initial seed point (Figs. 4.1c). A CEUS-T image is formed by determining the trajectories originating from many of these points distributed uniformly throughout the organ. We render the trajectories as semi-transparent colour-coded lines, emphasizing those paths that are followed by many streamlines as opposed to the ones that originate from only few. The colour coding can for instance reflect the macroscopic velocity magnitude (as calculated from the local time-delay distributions) or a tract feature (e.g. tortuosity, density).

4.2a 2D in-silico data generation.

The 2D transport of ultrasound contrast agents through a synthetic branching structure was simulated by propagating 2000 particles through the structure with a given velocity, comprising a deterministic flow (magnitude 1 mm/s) plus a Gaussian process noise component (zero mean with standard deviation 0.5 mm/s). The former simulates pure convection, whereas the latter served as a model for diffusion. The ultrasound acquisition was simulated by modelling the scanner's point spread function as a bivariate Gaussian, with standard deviations that reflect the axial (σ = 0.14 mm) and lateral (σ = 0.16 mm) resolution. The frame rate was set to 10 Hz, and the pixel spacing was 0.15 mm.

4.2b 3D DCE-US in-vivo data acquisition.

The 3D transrectal DCE-US acquisitions were performed at the Second Affiliated Hospital of the Zhejiang University School of Medicine (Hangzhou, Zhejiang, China). The

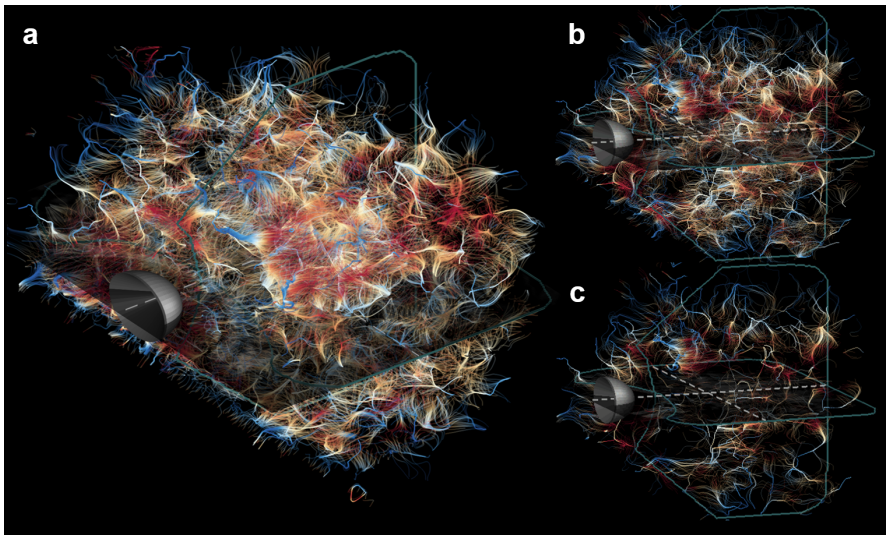

Figure 4.3: 3D CUVT of a human prostate a. CEUS-T image, displaying the network of trajectories obtained by applying the method to a transrectally recorded CEUS sequence of a human prostate. b. CEUS-T image where only trajectories longer than 5mm are displayed. c. only trajectories longer than 8mm are displayed. Colors depict the macroscopic flow velocity.

patients received a 2.4-ml bolus injection of SonoVue®, of which the passage through the prostate was imaged using a 3D transrectal ultrasound probe (RIC5-9) and a LOGICQ E9 ultrasound scanner (GE Healthcare, Wauwatosa, WI, USA). A contrast-specific imaging mode was employed, and the organ was imaged for 2 minutes. The imaging quality setting was set to "low" in order to reach a volume rate of approximately 0.3 Hz. The voxel size is 0.25 × 0.25 × 0.25 mm. The *in-vivo* studies received prior approval from the local ethics committee. Informed consent was obtained from all patients.

4.2c Up-sampling and interpolation.

The 3D datasets are up-sampled by a factor 10 prior to the analysis using Whittaker-Shannon interpolation by zero-padding the temporal fast Fourier transform (FFT) of the input dataset, after which an inverse FFT is performed.[160]

4.2d Velocity vector estimation.

A local estimation of the microbubble flow velocity and directionality is obtained by considering the time-intensity relation amongst specific set of data points: $N = 226$ voxels spatially distributed on a sphere with a radius of 0.8 mm around the origin. The antipodes (pairs of voxels that are mirrored with respect to the origin) are selected, and the time delays amongst those time-intensity curves are then estimated by determining the peak of their cross-correlation functions.[150] The local propagation velocity vector $\vec{v} = \left[v_x, v_y, v_z\right]$ can then be estimated by solving the following linear system of equations using least-squares:

$$\vec{v}^{\,T}\tau = \mathrm{D}, \tag{4.1}$$

where τ is the row vector that contains all the estimated time delays and D is the matrix that describes the inter-voxel distance vectors. This procedure is repeated for all pixels in order to produce a velocity vector field.

4.2e Anisotropic filtering.

The obtained vector fields are smoothed using an anisotropic Gaussian filter that promotes velocity vectors that share a similar orientation with neighbouring voxels.[162] The standard deviation of this oriented filter was 2 voxels in the direction of ultrasound-contrast-agent propagation, whereas this value is set to 1 voxel in the directions orthogonal to this component.

4.2f Tractography.

The streamlines of the velocity field are obtained by solving the following ordinary differential equation:[161,163]

$$\begin{cases} \partial_t x(t) = \vec{v}\,[x(t)] \\ x(0) = x_0 \end{cases}, \tag{4.2}$$

which describes how, given an initial seeding point x_0, a particle moves within the velocity vector field $\vec{v}(x)$. We employ an explicit Euler method to solve (4.2), as implemented in the MATLAB (MathWorks, Massachusetts, United States) `stream3c` function. The seeding points of the algorithm are distributed uniformly across the imaging space, sub-sampled by a factor 3 in each direction. The maximum number of streamline vertices was set to 1000 and the integration step size was 0.1 (one-tenth of a cell). We finally re-sample the resulting tracts based on a nearest-neighbour scheme such that the distance between two samples is approximately 0.1 mm.

4.2g Tortuosity.

Tortuosity is assessed by calculating the inflection-count metric (ICM) of each tract.[164] The ICM calculates the number of inflection points along the tract and multiplies this number (plus 1) by the total path length of the curve divided by the distance between endpoints.

4.2h Histopathological analysis.

After surgical resection, the prostate glands were fixed in formalin and the prostate was dissected into slices of 4-mm thickness. The slices were Haematoxylin/Eosin stained, and a pathologist determined the presence and extend of the tumour based on the degree of cell differentiation, according to the International Society of Urological Pathology (ISUP) consensus recommendations.[165]

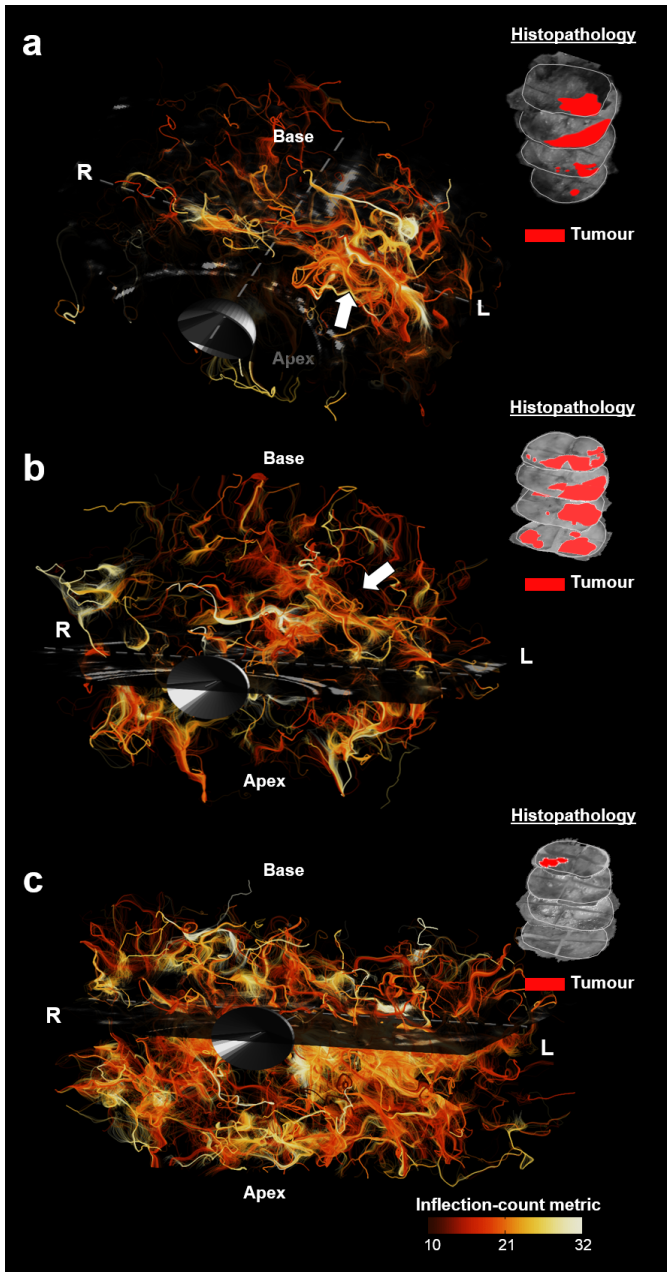

Figure 4.4: 3D CEUS-T and tortuosity quantification on 3 different human prostates with histology. Colours encode the tract inflection count metric (ICM). a. *Prostate I*: CEUS-T displays elevated ICM and higher tract-density on the left mid-base side of the prostate. Histology reveals a malignant lesion (Gleason score: 4+5=9), with a left mid-basal focus. b. *Prostate II*: CEUS-T yields a higher tract density on the complete left side of the prostate. Histology reveals a malignant lesion on the left (Gleason score: 5+5=10) and another significant lesion with a right apical focus (Gleason score: 4+5=9). c. *Prostate III*: CEUS-T shows a generally dense image. Here histology yielded benign prostate hyperplasia across the entire gland and a small malignant lesion (Gleason score: 3+3=6) in the basis.

4.3 Results

Figure 4.2 demonstrates the ability of CEUS-T to identify flow trajectories from synthetic *in-silico* data of microbubble transport through a branching network. Multiple streamlines are generated from the indicated seed-points based on a probabilistic approach, displaying the four branches of the vascular tree that are not visible in the standard maximum ultrasound intensity image.

When applying CEUS-T to an *in-vivo* 4D CEUS recording of a human prostate, we obtain a dense network of trajectories, with pathways of high incidence revealing what are most likely real vascular structures (Fig. 4.3). We can regulate the density of streamlines by visualizing only those trajectories that have a path length above a certain threshold, as shown in Figs. 4.3b-4.3c.

More *in-vivo* examples are given in Fig. 4.4. These cases come from patients that were diagnosed with prostate cancer, and referred for radical prostatectomy. We encoded CEUS-T tracts with colours that represent a tract-feature related to tortuosity: the inflection-count metric (ICM). In case one (4.4a), the image displays a denser network of trajectories on the left side of the prostate, with elevated ICM values. A corresponding malignant lesion (Gleason score 4+5=9) was found by histology. A similar CEUS-T pattern can be observed for case two (4.4b), where histology revealed a malignant lesion (Gleason score 5+5=10) on the complete left side of the prostate, and another lesion with a right apical focus (Gleason score: 4+5=9). In case three, the CEUS-T image generally appears very dense however. Interestingly, vast benign prostate hyperplasia (BPH) was found across the entire gland along with a small low-grade lesion (Gleason grade: 3+3=6). As for prostate carcinoma, BPH is associated with neo-vascularization.[166,167]

4.4 Conclusions

We demonstrated that the techniques developed for DTT magnetic resonance imaging can be applied to 3D microbubble flow vector fields obtained from CEUS, to attain CEUS-T images. CEUS-T has the remarkable ability to visualize 3D microbubble flow trajectories in a comprehensible and effective manner. The method can be applied effectively to standard CEUS data that is acquired with a clinical ultrasound scanner in a clinical setting using approved contrast agents. In two out of three prostate-cancer cases, the tract density of CEUS-T qualitatively showed a striking resemblance with the malignancies found by histopathology (the third case displayed widespread benign hyperplasia). These results suggest that the information captured by CEUS-T can be used to assess vascular characteristics linked to tumour-driven angiogenesis. While its full potential and diagnostic value remains to be investigated, it is conceivable that CEUS-T provides a relevant asset in those applications where vascular characteristics are of interest. The cases shown in this article are related to the detection of prostatic malignancies; yet CEUS-T is in principle suited to any dynamic CEUS recording of any organ. As such, it carries a widespread potential.

4.5 Acknowledgements

This work is part of the research programme 10769, which is partly financed by the Netherlands Organization for Scientific Research (NWO). The research has also received funding from the European Research Council / ERC grant agreement n. 280209.

5

Sparsity-driven super-resolution in clinical contrast-enhanced ultrasound

Abstract - *Super-resolution ultrasound enables detailed assessment of the fine vascular network by pinpointing individual microbubbles, using ultrasound contrast agents. The fidelity and achieved resolution of this technique is determined by the density of localized microbubbles and their localization accuracy. To obtain high densities, one can evaluate extremely sparse subsets of microbubbles across thousands of frames by using a very low microbubble dose and imaging for a very long time, which is impractical for clinical routine. While ultrafast imaging somewhat alleviates this problem, long acquisition times are still required to enhance the full vascular bed. As a result, localization accuracy remains hampered by patient motion. The aim of this work is hence twofold. First, to attain a high microbubble localization accuracy on dense contrast-enhanced ultrasound data using a clinical dose of ultrasound contrast agents and a standard clinical scanner. Second, to retain a high resolution by adequate motion compensation.*

From: R.J.G. van Sloun, O. Solomon, Y.C. Eldar, H. Wijkstra, and M. Mischi,"Sparsity-driven super-resolution in clinical contrast-enhanced ultrasound", *Proceedings of the IEEE International Ultrasonics Symposium*, Washington, USA, 2017

5.1 Introduction

Super-resolution ultrasound is a recently emerged imaging technology that enables detailed assessment of the fine vascular network by translating concepts from fluorescence photo-activated localization microscopy (FPALM,[168]) to ultrasound. Where FPALM localizes active and isolated fluorophores, super-resolution ultrasound exploits ultrasound-contrast-agents: inert gas microbubbles (MBs) that are sized similarly to red blood cells. Hence, they remain intravascular. By pinpointing individual isolated MBs with high precision across many frames, one can circumvent the diffraction limit and reconstruct an image at a 10-fold increase in resolution.[169] The availability of such an imaging technique in clinical practice would open up new possibilities for precise vascular characterization in the context of localizing tumour-driven angiogenesis, or assessment of impaired cardiac perfusion. In this paper, we apply sparse signal recovery techniques to attain super resolution on highly dense, clinically acquired contrast-enhanced ultrasound (CEUS) images.

Typically, extremely sparse subsets of MBs are evaluated across thousands of frames by using a very low MB dose and imaging for a very long time. Such a condition enables isolating individual bubbles effectively; however, in particular the latter is impractical for clinical routine. While high-frame-rate imaging somewhat alleviates this problem,[154] long acquisition times (in the order of minutes) are still required to cover the full vascular bed. Alternatively, and more practically, one can increase the density of MBs to a clinical dose. However, this causes the point-spread-functions of bubbles to overlap severely, invalidating the widely used single-particle localization methods.[170]

In optics, a similar trade-off between acquisition time and localization accuracy was addressed by the introduction of super-resolution optical fluctuation imaging (SOFI), which features a moderate resolution gain within short acquisition times.[171] Bar-Zion *et al.* translated the principles of SOFI to CEUS, by relying on the temporal statistics of demodulated echoes of flowing MBs between consecutive frames, demonstrating a moderate spatial resolution gain, but with a temporal resolution of tens-hundreds of milliseconds.[172] More recently, the introduction of sparsity-based ultrasonic super resolution hemodynamic imaging (SUSHI)[173] led to further increase the spatial resolution, while maintaining sub-second temporal resolution. This ultrasound method exploits sparsity in the temporal correlation structure of fluctuating MBs at a very high frame-rate (e.g. by using plane-wave imaging). When scanning with low frame-rates, as in most clinical scanners, this correlation vanishes due to the MBs decorrelation time of a few milliseconds however.[154]

Here, we apply similar sparse signal recovery techniques to attain super-resolution on highly dense, clinically acquired *in-vivo* CEUS images of a human prostate. By modelling an individual CEUS frame as the convolution of the MB distribution with the system point spread function (PSF), we employ sparse reconstruction techniques to recover the MB positions even in scenarios with extensive overlaps.

The clinical CEUS data acquisition protocol is given in Section 5.2a, after which the adopted sparse recovery and motion compensation algorithms are presented in Sections 5.2b and 5.2c, respectively. The results are described in Section 5.3, and the

conclusions are derived in Section 5.4.

5.2 Methods

5.2a Data acquisition

The *in-vivo* CEUS data were acquired at the AMC University Hospital (Amsterdam, the Netherlands). An intravenous injection of a 2.4-ml MB bolus (SonoVue®, Bracco, Milan, Italy) was administered, and its passage through the prostate was imaged using a C10-3v transrectal endfiring ultrasound probe. The CEUS loops were acquired and stored using a Philips iU22 ultrasound system (Philips Healthcare, Bothell, WA). A dual-screen view was selected to simultaneously obtain fundamental mode as well as contrast-specific imaging data. The axial resolution of the ultrasound system is approximately 0.3 mm and its lateral resolution is in the order of 0.5 mm at 5 cm from the probe. At this distance, the elevational beamwidth is approximately 3.4 mm. The pixel spacing is 0.146 mm in both directions. Imaging was performed for 120 seconds to record the full in- and out-flow of the injected MB bolus. The data were then linearised according to[71] in order to obtain the ultrasound intensities from the log-compressed and quantized image data.

5.2b Sparse recovery

We model the measured CEUS frames as:

$$\mathbf{y} = \mathrm{A}\mathbf{x}, \tag{5.1}$$

where $\mathbf{x}$ is a vector which describes the MB distribution on a high-resolution image grid, $\mathbf{y}$ is the vectorized frame of the CEUS loop, interpolated to the grid dictated by $\mathbf{x}$, and A is the measurement matrix where each column of A is the shifted PSF. Each entry of $\mathbf{y}$ and $\mathbf{x}$ corresponds to a specific pixel in the image. The PSF of the system is estimated from the data by first manually pinpointing several isolated MB spots from those frames in which only few were present. These spots were then block-windowed and fitted with a rotated anisotropic 2D Gaussian kernel to mitigate the impact of noise on the PSF. Given the PSF, the goal is now to obtain the MB vector $\mathbf{x}$ from the measurements $\mathbf{y}$ according to (5.1). With $\mathbf{x}$ defined on a much denser grid than the original CEUS frame, this is an ill-posed problem however, requiring the use of some form of regularization. If we assume that the MB distribution is sparse on a sufficiently high-resolution grid, i.e. $||\mathbf{x}||_0$ (number of non-zero entries in $\mathbf{x}$) is low, we can formulate the following regularized problem:

$$\hat{\mathbf{x}} = \arg\min_{\mathbf{x}} ||\mathbf{y} - \mathrm{A}\mathbf{x}||_2^2 + \lambda||\mathbf{x}||_0, \tag{5.2}$$

where λ is a parameter that determines the influence of the sparsity-promoting penalty $||\mathbf{x}||_0$ on the estimate. The problem described in (5.2) is however an NP-hard combinatorial problem. To make the solution tractable, we resort to a widely adopted heuristic alternative to (5.2), by replacing $||\mathbf{x}||_0$ with $||\mathbf{x}||_1$:[174]

$$\hat{\mathbf{x}} = \arg\min_{\mathbf{x}} ||\mathbf{y} - \mathrm{A}\mathbf{x}||_2^2 + \lambda||\mathbf{x}||_1. \tag{5.3}$$

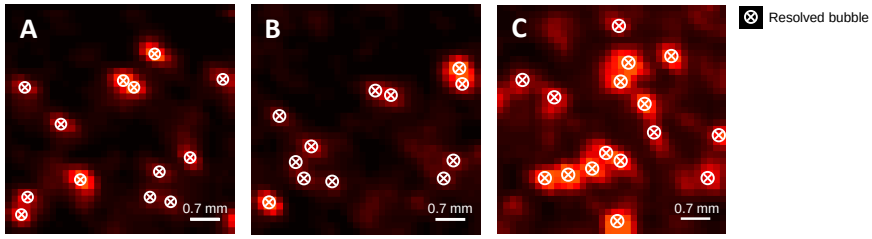

Figure 5.1: Selected examples of microbubble (MB) location recovery using the proposed algorithm with varying MB densities. (A,B) Localization for relatively low densities, with several overlapping point-spread-functions. (C) Localization for high densities, with many overlapping point-spread-functions.

To facilitate high-resolution MB localization, the grid on which $\mathbf{x}$ is assessed is over-sampled by a factor 4 with respect to the original pixel grid. For large $\hat{\mathbf{x}}$, solving this optimization problem poses very high demands on memory and computation power. To limit the dimensions of the matrix A, we divided the up-sampled CEUS frames into partially overlapping patches of size 128×128, which were processed separately. The results for all these subregions are then stitched together.

For each region, eqn. (5.3) is numerically solved using the Fast Iterative Shrinkage Thresholding Algorithm (FISTA), a fast proximal gradient method.[175] The FISTA algorithm is modified to only consider non-negative values for $\mathbf{x}$. After estimating $\mathbf{x}$ for each frame, the estimated MB distributions in $\mathbf{x}$ are summed across all frames to yield the final super-resolution image.

5.2c Motion compensation

To correct the detected high-resolution MB distribution for tissue motion, we first extract the pure-tissue signal from the fundamental mode images. With the aim of separating those components originating from tissue, MBs, and noise, we formulate the source extraction problem as a subspace selection problem. To this end, we perform a singular value decomposition (SVD) on the full space-time CEUS data (*i.e.* a matrix of which the columns are the vectorized frames), and attribute the first k singular values to tissue. The resulting rank-k approximation of the original space-time matrix that is based on these low-order singular values yields signal components with high spatiotemporal coherence. Such an approach was recently introduced as a highly effective clutter filtering strategy to remove tissue signal.[176] Here we exploit it for tissue-signal extraction rather than removal. For each subregion/patch, we determine the affine transformation that maps the image data back to the first frame in the loop, by minimizing the mean squared error among those patches. We use MATLAB's (The MathWorks, Natick, MA) `imregtform` function for this purpose. We then apply the same transformation to the estimated MB distribution $\hat{\mathbf{x}}$ to adequately compensate for displacements induced by tissue motion. While this patch-based approach effectively deals with probe-motion (translation) and to some extent local strain (scaling), it is limited to in-plane transformations. Motion compensation is performed after MB localization to avoid distortion of the system PSF following the affine transformation.

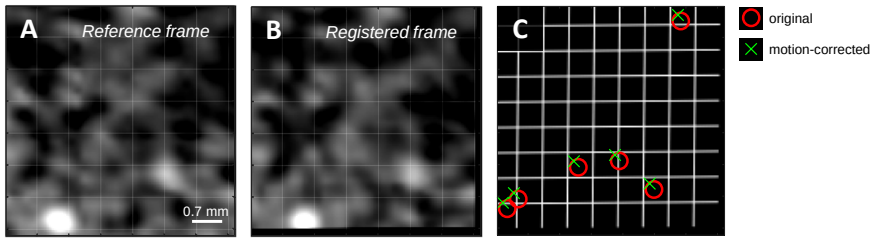

Figure 5.2: (A) First up-sampled fundamental mode image in the sequence, serving as the reference frame. (B) Resulting registration of a frame captured 3 seconds later. (C) Motion-corrected microbubble locations.

5.3 Results

Several examples of MB localization based on sparse recovery are given in Figure 5.1. Compared to (A,B), the detected MB density is notably higher in (C), demonstrating the method's ability to deal with varying densities and signal intensities.

In Figure 5.2, we exemplify the adopted motion compensation procedure and indicate how this impacts the MB location estimates.

Figure 5.3 shows the obtained super-resolution ultrasound image of a region of interest in the human prostate. In total, 300 frames were used to construct this image, which were taken during the wash-out phase of the CEUS acquisition. The proposed sparse-recovery method reveals fine details that are not visible in the diffraction limited maximum-intensity projection.

5.4 Conclusions and Discussion

In this paper, a new super-resolution ultrasound method that is designed specifically to deal with high-density clinically-acquired CEUS data is presented. By adapting sparse reconstruction techniques as used in fast super-resolution fluorescence microscopy, and combining them with effective motion compensation, the proposed method enables high resolution imaging of the perfused vasculature in a standard clinical setting.

We observed that bubbles can be localized (Figure 5.1), even if their PSFs show significant overlap. Moreover, the method yields plausible position estimates for varying densities, without adapting the algorithm parameters (e.g. the sparsity-promoting penalty λ).

A qualitative exemplification of the results obtained with this principle is shown in Figure 5.3, where complex and fine vascular structures are revealed. This level of detail was achieved with merely 300 image frames, which was predominantly limited by the increasingly impaired robustness of motion compensation after longer accumulation times.

Tissue motion impedes the achievable resolution and fidelity of super-resolution

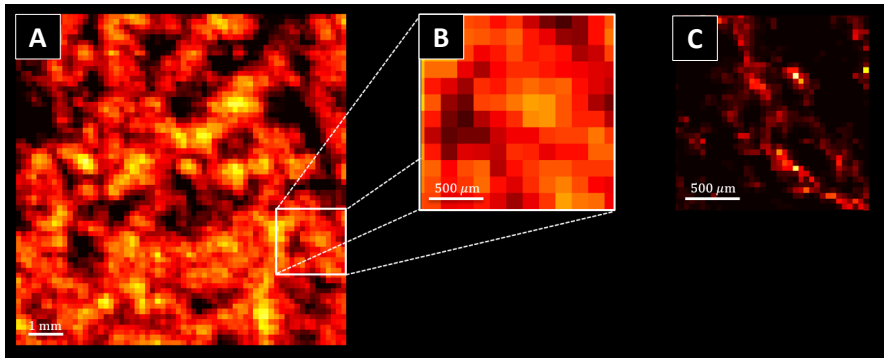

Figure 5.3: (A) Standard maximum intensity projection of a CEUS acquisition in a human prostate and (B) a selected area in the image. (C) Sparsity-driven super-resolution ultrasound on the same area.

methods. Although dedicated registration techniques were exploited to mitigate its impact, one can not account for out-of-plane movements which are in practice inevitable. This stresses the need for methods that can reach a high density of localized bubbles in a very short time in a clinical setting, and exploitation of 3D ultrasound acquisitions that facilitate complete registration in all directions.

The initial results presented in this work are promising and yield plausible outcomes. Yet, a more extensive study is required to validate the proposed approach. The localization performance should be thoroughly assessed *in-silico* and, ideally, to some extent *in-vitro*. The latter poses challenges on its own, as microfabrication of vascular structures is in practice not an easy task. These aspects, along with optimization of the adopted algorithm and exhaustive comparison with alternative super-resolution methods, are therefore part of future work.

5.4 Acknowledgement

This work was supported by the European Research Council Starting Grant (#280209).

6

Towards Dynamic Contrast Specific Ultrasound Tomography

Abstract - *We report on the first study demonstrating the ability of a recently-developed, contrast-enhanced, ultrasound imaging method, referred to as cumulative phase delay imaging (CPDI), to image and quantify ultrasound contrast agent (UCA) kinetics. Unlike standard ultrasound tomography, which exploits changes in speed of sound and attenuation, CPDI is based on a marker specific to UCAs, thus enabling dynamic contrast-specific ultrasound tomography (DCS-UST). For breast imaging, DCS-UST will lead to a more practical, faster, and less operator-dependent imaging procedure compared to standard echo-contrast, while preserving accurate imaging of contrast kinetics. Moreover, a linear relation between CPD values and ultrasound second-harmonic intensity was measured (coefficient of determination=0.87). DCS-UST can find clinical applications as a diagnostic method for breast cancer localization, adding important features to multi-parametric ultrasound tomography of the breast.*

From: L. Demi, R.J.G. van Sloun, H. Wijkstra, and M. Mischi,"Towards Dynamic Contrast Specific Ultrasound Tomography", *Nature Scientific Reports*, vol. 6, ©Nature Publishing Group, 2016

6.1 Introduction

Nowadays, there is growing interest in the development of imaging techniques which are capable of detecting and localizing angiogenesis and neovascularization. These processes induce specific changes in the microvascular structure, represent an established marker for tumours, and also relate to tumour aggressiveness.[177] In particular, dynamic contrast-enhanced ultrasound (DCE-US) imaging shows promise, with many novel approaches focusing on the direct and/or indirect characterization of the microvasculature. However, when considering the various imaging options, several challenges emerge for imaging the breast.

Typical ultrasound contrast agents (UCAs) are gas-filled microbubbles with diameters ranging between 1 and 10 μm; they can therefore be injected intravenously and can flow through the smallest microvessels. This is exploited by super-localization ultrasound techniques, which overcome the diffraction limit and are capable of imaging the microvasculature with a spatial-resolution as small as 8-12 μm.[154,178] Additionally, these techniques provide accurate velocity maps, thereby offering a powerful tool for studying microvascular blood flow. However, the relatively long imaging time required (e.g., >2 minutes per plane[154]), the influence of motion, and the difficulties in imaging and localizing single microbubbles in deep tissue, pose limitations to the use of these modalities in large organs.

Another recently-developed imaging method is acoustic angiography.[157] With this technique, high spatial-resolution images (in the order of 100 μm) are obtained using tenfold higher frequencies than with normal DCE-US echo-imaging. Once again, the key lies in the UCAs peculiar response to ultrasound. Because of their highly nonlinear behaviour, UCAs backscatter high-frequency broadband echo signals (15-35 MHz), which can be used to achieve improved spatial-resolution.[179] However, frequency-dependent attenuation practically constrains the applicability of this technique to relatively small depths, such as those required for imaging the peripheral zone of the prostate (1-2 cm).

Other techniques chose a different path rather than targeting high spatial-resolution. Standard DCE-US imaging (i.e., Harmonic Imaging, Pulse Inversion, and Amplitude Modulation) is an echographic technique, which in essence exploits variations in the second harmonic amplitude to generate real-time images of UCA kinetics when flowing through the vasculature.[180,181] In particular, the analysis of microbubble flow-dynamics through the vessels can be used to reveal changes in the vasculature itself. To this end, several techniques which are based on the quantification of parameters related to UCA perfusion and dispersion have been proposed.[71,182–185] Although the typical DCE-US spatial resolution is in the order of 1 mm, hence unsuitable for imaging microvascular changes, these techniques are still able to infer relevant information in relation to the 'angiogenic switch' (the transition from a pre-vascular to a vascularized tumour phenotype) required for cancer to grow beyond 1-2 mm in diameter.[67,186]

However, performing a hand-held DCE-US is particularly challenging for the breast, and makes imaging highly dependent on the skill and experience of the operator. Moreover, imaging artefacts affect standard DCE-US and limit UCA quantification and localization accuracy.[187,188] The development of dynamic contrast-specific ultrasound

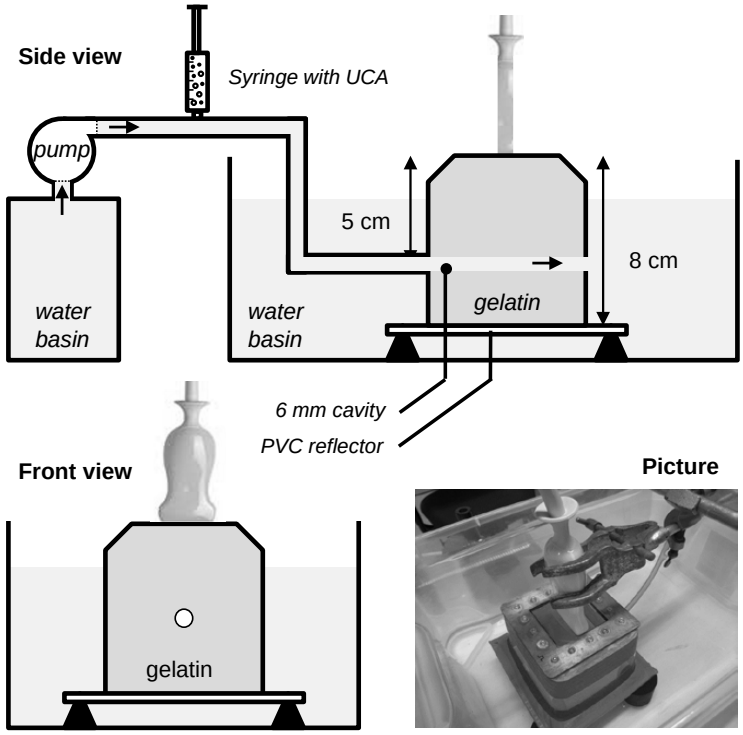

Figure 6.1: Illustrative picture, and schematics of the side and front view of the set-up are shown.

tomography can alleviate these issues, allowing for a more-practical, faster, and less operator-dependent imaging procedure.[189,190]

To this end, a contrast-specific imaging modality named cumulative phase delay imaging (CPDI) has recently been proposed for contrast-enhanced ultrasound tomography.[191,192] CPDI is based on the fact that the different physical phenomena behind nonlinear propagation in tissue and UCA are producing a different delay accumulation between the second harmonic (2H) and fundamental (Fo) component of the ultrasound field. In particular, a positive delay between 2H and Fo is a marker which is specific to UCAs as opposed to variations in harmonic amplitude (exploited for echo imaging), speed of sound, and attenuation (exploited for ultrasound tomography). CPDI has already proved to be capable of detecting and imaging UCA concentrations when working at pressure regimes ($0.05 \leq MI \leq 0.2$) and frequencies (2.5-3 MHz) of interest for clinical applications. Although these initial studies demonstrated the feasibility of CPDI, its ability to capture UCA kinetics has never been demonstrated.

As the achievable spatial resolution for ultrasound tomography is not expected to be comparable with that achievable with acoustic angiography and super-localization techniques, the ability of CPDI to image UCA kinetics is crucial to reach clinical significance.

6.2 Methods

6.2a Flow phantom

A dedicated flow phantom was used to perform the experiment. A tissue-mimicking gelatin phantom (as reported in 20) containing a cylindrical cavity with a 6-mm diameter was employed. A solenoid pump E410 (CEME) was used to generate the flow. A calibrated flow value equal to 0.26 L/s was employed. A fixed volume (5 mL) of SonoVue®contrast agent with a concentration equal to 240 μL/L was repeatedly injected (manually) throughout the cavity. The cavity lay at a depth of 5 cm from the location of the probe, and perpendicular to the imaging plane. Further down, at 8 cm, a PVC plate was positioned. The echoes which backscattered from the plate could therefore be recorded by the probe and used to form a tomographic image. At the same time, it was possible to measure the backscattered echoes from the microbubbles and use them to form harmonic images in echo graphic mode. This approach allowed us to compare the two imaging techniques, CPDI and HI, when (simultaneously) imaging the same bolus passage.

6.2b Data collection

An active sub-aperture of 64 elements was used to transmit and receive the ultrasound fields, and linearly shifted over the 192-elements linear array to form a 128-line data set. The field of view was 20 mm wide and 90 mm deep. No focusing was applied in transmission and dynamic receive beamforming was used. The post beamformed data were stored and used for the analysis. A 10-cycle pulse with its centre frequency at 2.5 MHz, and whose amplitude was modulated by a Hamming envelope, was used as a driving signal. In receive mode, a sampling frequency of 50 MHz was used. A total of 80 frames were consecutively acquired for each bolus, at a frame rate of 8 Hz. A mechanical index (MI) equal to 0.07, which was measured with a hydrophone (HGL-0400 Onda, Sunnyvale, CA) at a depth of 5 cm, was used to minimize bubble disruption. The hydrophone, with a bandwidth ranging from 250 kHz to 20 MHz, was connected to a preamplifier (AH-2010-025 Onda, Sunnyvale, CA) whose bandwidth ranged from 50 kHz to 25 MHz, which in turn was connected to a 100 MHz A/D converter (PCI-5406 National Instruments, Austin, TX). Dedicated Labview ®software was implemented and used for data acquisition. The MI was calculated as the ratio of the peak negative pressure in MPa and the square root of the frequency in MHz.

6.2c Harmonic Imaging

The second harmonic (2H) component was extracted by band-pass filtering. A -12 dB bandwidth around 5 MHz was selected. Subsequently, a two-dimensional spatial Gaussian filter (spatial standard deviation σ_x = 0.5 mm and σ_z = 0.25 mm) was applied to enhance the signal-to-noise ratio. To reconstruct the harmonic images, an average speed of sound equal to 1510 m/s was assumed.

6.2d Cumulative Phase Delay Imaging

In order to measure the cumulative phase delay (CPD) between Fo and 2H, firstly, the pressure fields which had backscattered from the plate were selected by time-windowing (window length equal to 5 μs). Secondly, the two components, i.e., Fo and 2H, were extracted from the data (a -12 dB bandwidth was selected around 2.5 MHz and 5 MHz, respectively) and the corresponding envelopes were obtained by using the Hilbert transform. Thirdly, the time delay between the maxima of the fundamental and second harmonic envelopes was obtained for each line, providing a measure of CPD as a function of the lateral direction, i.e., a projection. For this experiment, the symmetry of the target was exploited for the reconstruction, i.e., CPD projections were assumed to be independent on the imaging angle. Finally, the filtered back-projection (filter type: Shepp-Logan) algorithm[193] was used to generate 2D-CPD images.

6.2e Time Intensity Curve

To obtain the time intensity curves from the HI and CPDI data, the image intensity values were averaged over the region corresponding to the location of the cavity. Following that, a moving average filter (window size equal to 0.75 s) was applied, and the baseline removed from the CPDI and HI TICs. The baseline was calculated as the mean value over the first 0.75 s. The average CPDI baseline was equal to -0.6 cycles/m.

6.2f Quantitative analysis

The peak time (PT) was calculated as the time at which the maximum of a TIC was observed. The arrival time (AT) was estimated as the first time the TIC amplitude exceeded 5% of its value at PT. The wash-in time (WIT) was calculated as the time between AT and PT. The full-width-half-maximum (FWHM) was calculated as the time interval across which the TIC amplitude remained above 50% of its value at PT. The area-under-the-curve (AUC) was calculated as the sum of the TIC-amplitude values over the entire time window (10 s long) multiplied by the length of the sampling interval (0.125 s).

6.2g Speed-of-sound and attenuation estimation

By using the same filtered back-projection algorithm that was applied to perform CPDI, tomographic images based on speed-of-sound and attenuation were obtained from the variations in the time-of-flight and amplitude of the peak of the fundamental envelope, respectively. Subsequently, histograms were obtained by analysing the image values over the region corresponding to the location of the cavity, during the passage of the boluses.

6.2h Dispersion evaluation

Values of CPD in tissue are determined by the combined effect of tissue nonlinearity and frequency dispersion. Both phenomena result in a negative CPD value. However, the contribution due to tissue nonlinearity can be assumed to be negligible as compared to that due to frequency dispersion, especially for highly absorbing tissues. In fact, in line with the Kramers-Kronig relationship,[194] dispersion and absorption are interlinked.

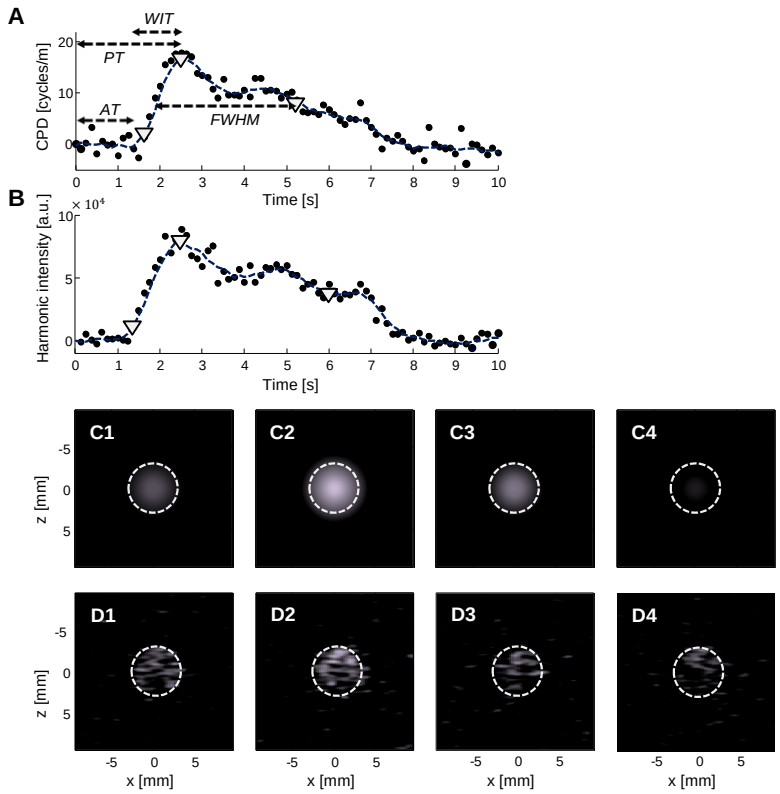

Figure 6.2: The ability of CPDI to capture UCA kinetics and qualitative comparison with HI: time-intensity curves (TICs) obtained from cumulative phase delay (A) and harmonic imaging (B). Raw (dots) and processed (lines) curves are shown. The cumulative phase delay (C) and harmonic (D) images of an ultrasound contrast agent bolus passage are shown at different time instants.

In conclusion, to evaluate CPD values, absorption measures reported in[195] for blood, fat, and breast tissue were used in combination with the theoretical model in.[196]

6.3 Results

The ability of CPDI to image UCA kinetics was investigated by imaging the passage of repeated UCA boluses through a dedicated gelatin flow-phantom (see Figure 1). CPDI and Harmonic Imaging (HI) were simultaneously applied to each bolus passage (in tomography and echo mode, respectively) in order to perform a comparison between the two methods and to analyse the relation between CPD values and harmonic intensity. In this paper, HI specifically refers to the pulse-echo imaging technique which relies on band-pass filters for the extraction of the second harmonic component.

Each bolus resulted from a 5-ml injection with a 240-μL/L UCA dilution. A clinically

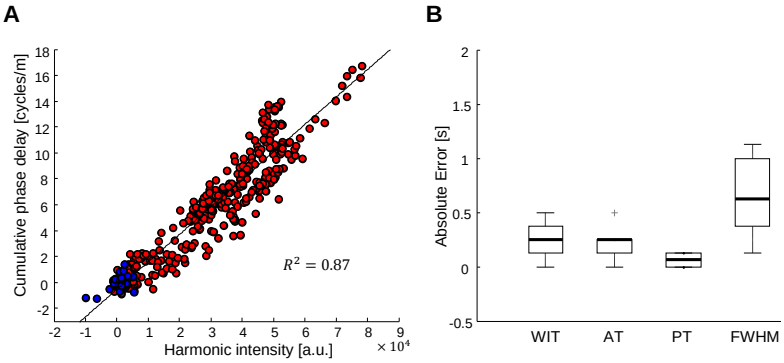

Figure 6.3: Linear relation between CPD values and 2H intensity and quantitative analysis: (A) Scatterplot of the cumulative phase delay values compared to the harmonic intensity values as obtained for the measured TICs. Blue points refer to values obtained before the arrival time. The red points refer to values measured during the passage of the bolus. (B) Box-plot showing the absolute error in seconds in comparison with quantitative analysis of multiple TICs features: wash-in time (WIT), arrival time (AT), peak time (PT), and full width half maximum (FWHM).

approved agent, SonoVue®(Bracco, Milan, Italy), was used for this study. To generate and store the ultrasound fields, a ULA-OP[197] ultrasound open research platform was employed together with an LA332 linear array probe (Esaote, Firenze, Italy). Insonating frequency, mechanical index (MI), and frame rate were set at 2.5 MHz, 0.07, and 8 Hz, respectively.

The ability of CPDI to capture UCA kinetics and qualitative comparison with HI. Figure 6.2 shows, for both CPDI and HI, an example of a time intensity curve (TIC), together with the corresponding images obtained at different time instances. Processed curves (red lines) are obtained using a 0.75-s moving average filter. Various TIC features which are commonly used to quantify UCA kinetics[71] are also marked: arrival time (AT), peak time (PT), wash-in time (WIT), and full width half maximum (FWHM). For both imaging modalities, each TIC was obtained by averaging the image values over the surface corresponding to the location of the channel cross-section (indicated by white dashed lines). Qualitatively, the two imaging methods provided similar results.

Figure 6.3a shows the relation between CPD values and second harmonic intensity as a scatterplot of the data-points of all TICs. The blue points refer to the values obtained before the arrival time. A linear relation is observed with a coefficient of determination equal to 0.87. Figure 6.3b shows a box-plot analysis of the absolute error values calculated for different TIC features when comparing CPDI and HI data. The feature that shows the highest absolute error is FWHM, with a median absolute error value equal to 0.625 s. As for the other features, the median absolute error was 0.25 s, 0.25 s, and 0.0625 s for AT, WIT, and PT, respectively.

The relative standard deviation of the area under the dilution curves, a feature which can be used for assessment of perfusion, was also calculated across all the measurements and was found to be equal to 0.18 and 0.17 for CPDI and HI, respectively. Moreover, the mean and standard deviation of the Pearson's correlation coefficient between TICs extracted by CPDI and HI were equal to 0.91 and 0.04, respectively. Overall, the

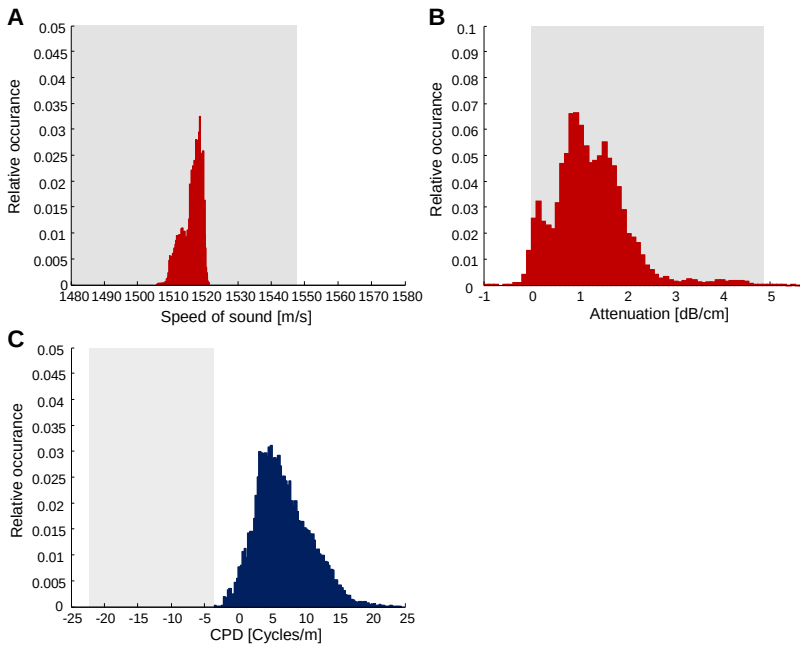

Figure 6.4: Comparison with speed of sound changes and attenuation due to UCA: Histograms of (A) speed of sound, (B) attenuation (measured at 2.5 MHZ), and (C) CPD values (expressed in cycles per mm) as obtained from our experiment. Histograms are obtained by analysing all the data over the area which corresponds to the location of the channel cross-section during the bolus passage. Each figure also shows the range (grey area) of values representative for breast tissue for each parameter: 1480-1548 m/s for speed of sound, 0.74-4.575 dB/cm for attenuation, and -22.5 to -3.56 cycles/m for CPD.

quantitative analysis of TICs obtained with both imaging methods provides equivalent results.

Comparison with speed of sound changes and attenuation due to UCA. Currently, no contrast-specific modality exists for ultrasound tomography. In fact, speed-of-sound variations and attenuation (normally used to perform ultrasound tomography[189,190]) due to UCAs can be confused (same range) with those caused by different tissue types,.[198–200] Conversely, CPDI is based on a marker specific for UCAs, thereby enabling dynamic contrast-specific ultrasound tomography.

Figure 6.4 shows the histograms of (A) speed of sound, (B) attenuation (measured at 2.5 MHz), and (C) CPD values (expressed in cycles per mm) obtained from our experiment. These histograms were generated by analysing all the data over the area corresponding to the location of the channel cross-section. Each figure also shows the range of values typically found in breast tissue for each parameter. The data for attenuation and speed of sound in breast tissue were obtained from[198] and,[199] respectively. The tissue range shown in Figure 6.4c was calculated considering blood, fat, and breast tissue, and based on frequency dispersion as derived from the models described in.[?,195] When considering speed of sound and attenuation variations, TICs can also be obtained by subtracting the baseline image, i.e., the tomographic image obtained in the absence of contrast, from all subsequent images. For illustrative purposes, Figure 6.5

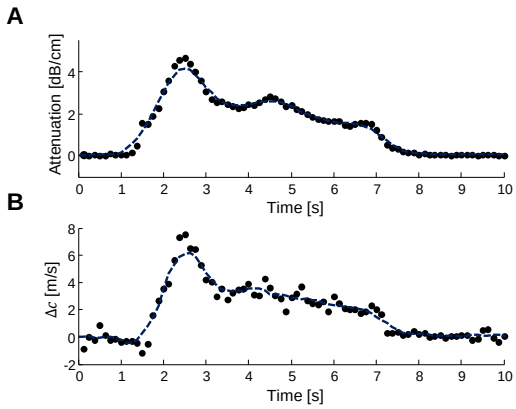

Figure 6.5: Time intensity curves displaying variations in attenuation (top) and speed of sound (bottom) with respect to baseline.

shows TICs obtained from speed of sound and attenuation variations corresponding to those shown in Figure 6.2. Such an approach would however suffer from motion artefacts; in the presence of motion, the actual baseline image will differ from that measured before contrast enhancement.

6.4 Discussion

In this paper the ability of CPDI to image UCA kinetics was investigated for the first time. A qualitative and quantitative comparison with HI was also performed.

Results show that CPDI can be successfully applied to image and quantify UCA kinetics. In particular, when compared to HI, equivalent results were obtained. Variations in speed of sound and attenuation due to UCA were also evaluated, and it was confirmed that they fall within tissue range. CPD values measured during the passage of the UCA boluses were confirmed to be positive. This allows full tissue separation, since CPD values in tissue are inherently negative. The fact that a positive CPD value represents a marker specific to UCA is of particular importance. In principle HI could also be implemented on tomography systems which are capable of reflection tomography. However, this will not avoid typical artefacts common to HI,[187,188] which limit UCA quantification and localization accuracy by HI.

Unlike standard DCE-US in echo-mode, CPDI does not require any particular multi-pulse scheme. In fact, the information required for imaging is contained in the time delay between 2H and Fo, which can be extracted from each single pulse.[191,192] Moreover, with a tomographic approach, only one-way time of flight constrains the pulse repetition frequency. Overall, these aspects allow for a higher time resolution, or faster acquisition time. Furthermore, as opposed to standard uncoded pulse-echo imaging, the pulse-length does not limit the axial-resolution. This allows for the use of longer pulses to enhance penetration and the signal to noise ratio. Moreover, the implementation of CPDI could benefit from existing speed-of-sound reconstruction algorithms which have already been developed for volumetric breast ultrasound scanners;[199,201] the time-of-flight could simply be replaced with CPD variations. These results are encouraging, and open the way to the development of dynamic contrast-specific ultrasound tomography, which could add important features to the multi-parametric ultrasound tomography of the breast, and improve breast cancer detection.

This paper reports on *in-vitro* results obtained by imaging the passage of UCA boluses through a cylindrical cavity surrounded by a homogeneous medium. In addition, the symmetry of the target was exploited for the tomographic reconstruction, i.e., CPD projections were assumed to be independent on the imaging angle. In real applications these two conditions do not apply and consequently impact on the image quality.

Future work will focus on taking new measurements with a breast ultrasound computed tomography scanner on heterogeneous and more complex flow-phantoms, with the ultimate aim of transferring this technology to patients.

6.5 Acknowledgements

This work is part of the research programme 10769, which is partly financed by the Netherlands Organization for Scientific Research (NWO). The research has also received funding from the European Research Council / ERC grant agreement n. 280209.

Part II

Tissue Markers

7

Viscoelasticity Mapping by Identification of Local Shear Wave Dynamics

Abstract - *Estimation of soft tissue elasticity is of interest in several clinical applications. For instance, tumours and fibrotic lesions are notoriously stiff compared to benign tissue. A fully quantitative measure of lesion stiffness can be obtained by shear wave elastography. This method uses an acoustic radiation force to produce laterally propagating shear waves that can be tracked to obtain the velocity, which in turn is related to the Young's modulus. However, not only elasticity, but also viscosity plays an important role in the propagation process of shear waves. In fact, viscosity itself is a parameter of diagnostic value for detection and characterization of malignant lesions. In this paper, we describe a new method that enables imaging viscosity from shear wave elastography by local model-based system identification. By testing the method on simulated datasets and performing in-vitro experiments, we show the ability of the proposed technique to generate parametric maps of the viscoelastic material properties from shear wave measurements, opening up new possibilities for non-invasive tissue characterization.*

From: R.J.G. van Sloun, R.R. Wildeboer, H. Wijkstra, and M. Mischi,"Viscoelasticity Mapping by Identification of Local Shear Wave Dynamics", *IEEE Transactions on Ultrasonics, Ferroelectrics, and Frequency Control*, ©IEEE, 2017.

7.1 Introduction

Imaging technologies for assessment of the elastic properties of soft tissue provide clinicians with an important asset for several diagnostic applications. Pathologies such as tissue fibrosis and cancer influence tissue elasticity. Accurate detection and staging of these pathologies is fundamental for providing adequate treatment and disease management. For this purpose, manual palpation is used extensively in clinical routine. Among the elastographic possibilities, ultrasound enables remote palpation using acoustic radiation force: shear wave (SW) elasticity imaging. By applying a push-pulse using high-intensity focused ultrasound, tissue is locally displaced in the axial direction, causing the formation of a laterally propagating SW. If one considers the medium to be purely elastic, its local shear modulus can be estimated by determining the local SW speed.

In practice, the assumption of pure elasticity does however not hold for many tissue types; tissue in which not only the stiffness, but also the shear viscosity plays an important role. Moreover, there is increasing evidence that viscosity itself could be a discriminant parameter for detection of malignancy. In,[202] Hoyt *et al.* assessed the elastic properties of prostate cancer tissue for their relevance as biomarkers. Their results revealed that the viscosity of cancerous prostate tissue is greater than that derived from normal tissue. Therefore, in this paper we aim at providing a joint estimate of tissue elasticity and viscosity based on SW elastography.

Initially, inversion of the Helmholtz equation was used to reconstruct SW speed from time-displacement data.[203,204] However, calculating the required second-order derivatives in space and time makes such an estimator very susceptible to the noisy signal conditions one can expect *in-vivo*. More recently-developed methods assess SW speed by calculating the wave arrival time across a set of axial displacement curves. In[205] and,[206] SW speed was obtained by assessing the lateral time-to-peak and exploiting linear regression to determine the rate-of-change across the set. Later, a more robust version of this approach was developed,[207] in which a random sample consensus (RANSAC) algorithm was employed to reliably perform such a regression in the presence of strong outliers. In,,[208] Rouze *et al.* showed that the SW time-of-flight can also be estimated using a Radon sum transformation, yielding a comparable robustness with respect to the RANSAC algorithm. An alternative approach determined the local SW speed by cross-correlating the displacement waveform at a specific position with that obtained at a reference location.[209] All of the above methods operate under the explicit assumption of negligible viscous dispersion across the evaluated region, translated in negligible wave shape deformation.

To assess the SW dispersion that originates from viscosity, Nenadic *et al.*[210] devised a method that relates the two-dimensional Fourier transform of time-displacement data to the frequency dependent SW phase velocity. By calculating the wave number (spatial frequency) that maximizes the spectrum at a given temporal frequency the phase velocity at each frequency can be obtained, which in turn can be parametrized using typical viscoelastic material models such as the Voigt model.[211] However, obtaining sufficient spatial frequency resolution to perform an accurate and reliable phase velocity estimate requires the use of a relatively large amount of space points. This seriously hampers its applicability to high-resolution mapping of viscosity. Rouze *et al.*[212] proposed the use of

a look-up table that relates the viscosity-driven difference in estimated SW group speed between axial particle velocity and displacement to the viscoelastic material parameters. Another elastographic imaging method aims at assessing the viscoelastic material parameters by estimating the mechanical relaxation time for a radiation-force-induced stress[213]. In,[214] single-tracking-location viscoelasticity estimation was proposed, in which viscosity was quantified through model-based quantification of wave dispersion of two laterally-spaced push pulses at a single tracking location.

In this work, we consider the viscoelastic material as a dynamic linear system, of which the impulse response can be locally identified by input-output (point-to-point) analysis of SW time-displacement curves. To this end, a local model-based estimator of the impulse response is derived from the Navier-Stokes equation, which is then fitted to the data in a least-squares fashion.

The SW data acquisition protocol and pre-processing steps are given in Secs. 7.2a and 7.2b, respectively. The details of the adopted signal model and an analytical description of the impulse response in viscoelastic materials are then given in Sec. 7.2. This impulse response is identified from the acquired data, to provide an estimation of the viscoelastic model parameters, as reported in Sec. 7.2d. The method is validated using simulated SW measurements (Sec. 7.3a) and *in-vitro* datasets (Sec. 7.3b.1), and the results are presented in Sec. 7.4. Finally, in Sec. 7.5, these results are discussed and conclusions derived.

7.2 Methods

7.2a Data acquisition

The experiments were performed using a Verasonics Vantage 128 ultrasound research platform (Redmond, WA, USA) in combination with an L11-4 linear array transducer. Shear waves (SW) were generated with acoustic radiation force, where the mechanical impulse delivered to the tissue is given by the product of acoustical force density and duration. Hence, to facilitate sufficient medium displacement, a 1500-cycle push-pulse with a centre frequency of 4.5 MHz was adopted (excitation-duration: 333 μs), and the excitation voltage was set to the maximum (overheating protected) value of 65 V. The resulting SW was tracked using an ultrafast imaging protocol operating at a frame rate of 10 kHz. A single-cycle pulse with a centre frequency of 6.25 MHz was used. The in-phase & quadrature (IQ) data were reconstructed after dynamic receive beamforming of the radiofrequency (RF) data, and stored for off-line processing. The final pixel dimensions in the axial and lateral directions were 0.086 mm and 0.208 mm, respectively. No additional averaging of repeated push-pulses was employed.

7.2b Pre-processing

To reveal the laterally propagating SW, we estimate its micron-scale axial displacements based on the well-known Loupass 2-D autocorrelator.[215] Initially developed for measuring blood flow velocity in Doppler systems, this approach estimates the mean axial velocity at each location by evaluating the 2D autocorrelation function of the IQ samples within a specific axial range N_{ax} and frame/ensemble range N_{ens}. In our experiments, these values were set to N_{ax} = 20 samples (1.7 mm) and N_{ens} = 5 frames

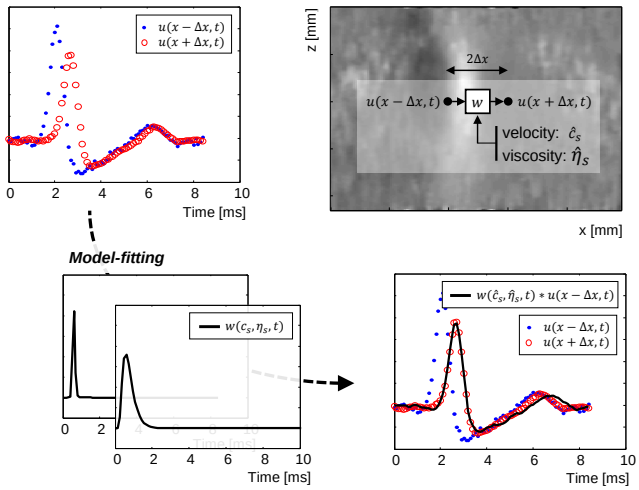

Figure 7.1: Illustrative overview of the proposed method, showing how the point-to-point impulse response is estimated from the time-displacement curves sampled at two spatial locations $x - \Delta x$ and $x + \Delta x$.

($500\mu s$), respectively. Finally, the axial velocity maps were spatially filtered using a 2D Gaussian kernel with a standard deviation of 1.2 samples in both the axial and lateral direction.

7.2c Shear wave signal model

For the purpose of estimating the SW propagation dynamics, we consider the displacement profiles measured at two laterally spaced pixels, and describe their relation as

$$u(x+\Delta x,t) = w(\Delta x,t) *_t u(x-\Delta x,t), \tag{7.1}$$

where $w(\Delta x,t)$ is the impulse response that characterizes the system describing the transition from $u(x-\Delta x,t)$ to $u(x+\Delta x,t)$. If one considers the SW propagation process as purely convective, the impulse response is a delayed delta function, and can be written as

$$w(\Delta x,t) = \delta\left(t - \frac{2\Delta x}{c_s}\right), \tag{7.2}$$

with c_s being the SW velocity. In this case, the model $w(\Delta x,t)$ can be identified by simply maximizing the cross correlation function between the two displacement profiles in order to find their time-delay, and thereby the SW velocity. In viscoelastic media, shear waves do not merely propagate in a convective manner; their shape also spreads over space. The Navier-Stokes equation provides us with a more general framework. Adopting the classical Voigt model to describe the viscoelastic properties of tissue,[211] i.e.

$$\sigma(t) = (\mu_0 + \eta\partial_t)\varepsilon(t), \tag{7.3}$$

with stress $\sigma(t)$, strain $\varepsilon(t)$, stiffness $\mu_0 = \rho c_s^2$ (elastic spring), and viscosity η (dashpot), SW particle displacements can be written as follows:[216]

$$\rho\partial_t^2 u(\vec{r},t) - (\rho c_s^2 + \eta_s\partial_t)\nabla^2 u(\vec{r},t) = S(\vec{r},t), \tag{7.4}$$

where ρ is the mass density and $S(\vec{r}, t)$ is the excitation source. The spatiotemporal impulse response of this system, termed the Green's function $g(\vec{r}, t)$, is then obtained by solving

$$\rho\partial_t^2 g(\vec{r}, t) - (\rho c_s^2 + \eta_s \partial_t)\nabla^2 g(\vec{r}, t) = \delta(\vec{r})\delta(t). \tag{7.5}$$

In one space dimension, x, Eq. (7.5) can be written in the 2D Fourier domain as

$$-\rho\omega^2 G(k_x, \omega) + (\rho c_s^2 + j\omega\eta_s)k_x^2 G(k_x, \omega) = 1. \tag{7.6}$$

Equation (7.6) is derived specifically for a Voigt material. It can however be generalized to describe other material models in terms of a frequency-dependent shear modulus $\mu(\omega)$, such that we obtain

$$-\rho\omega^2 G(k_x, \omega) + \mu(\omega)k_x^2 G(k_x, \omega) = 1, \tag{7.7}$$

from which we can derive the following Green's function solution:

$$G(k_x, \omega) = \frac{(1/\rho)}{[\mu(\omega)/\rho]k_x^2 - \omega^2}. \tag{7.8}$$

The inverse Fourier transform of (7.8) with respect to k_x is given by

$$G(x, \omega) = \frac{\sqrt{\pi/2}}{j\omega\rho\sqrt{\mu(\omega)/\rho}} \exp\left[-\frac{j\omega|x|}{\sqrt{\mu(\omega)/\rho}}\right]. \tag{7.9}$$

From (7.9), the impulse response $w(\Delta x, t)$ from one space point to another can be described in the frequency domain as

$$W(\Delta x, \omega) = \frac{G(|x| + 2\Delta x, \omega)}{G(|x|, \omega)} = \exp\left[-\frac{j\omega|2\Delta x|}{\sqrt{\mu(\omega)/\rho}}\right]. \tag{7.10}$$

7.2d Shear wave system identification

To locally estimate the viscoelastic model parameters in the Voigt model ($\mu(\omega) = \rho c_s^2 + j\omega\eta_s$), from (7.1) and (7.10), we formulate the following nonlinear least squares problem:

$$\begin{aligned}\{\hat{c}_s, \hat{\eta}_s, \hat{\alpha}\}(x) = \min_{c_s, \eta_s, \alpha} \| \mathcal{F}^{-1}[W(\Delta x, \omega)V(x - \Delta x, \omega)] \\ - v(x + \Delta x, t)\|_2^2,\end{aligned} \tag{7.11}$$

where $V(x - \Delta x, \omega)$ is the temporal Fourier transform of $v(x - \Delta x, t)$, the axial particle velocity signal. This Fourier domain implementation of the convolution between $v(x - \Delta x, t)$ and $w(\Delta x, t)$ avoids aliasing that can occur when sampling the impulse response $w(\Delta x, t)$ in the time domain. Such a situation is likely to occur in a low-viscosity case, where $w(\Delta x, t)$ approximates a delta function. On the other hand, sampling in the Fourier domain on the bandwidth determined by the sample rate produces a filtered version of the impulse response, without aliasing in the time domain (corresponding to a shifted and sampled Sinc function for $\eta = 0$). In addition, the approach allows for a computationally efficient implementation via the fast Fourier transform. Equation (7.11) is numerically solved in an iterative fashion using a Nelder-

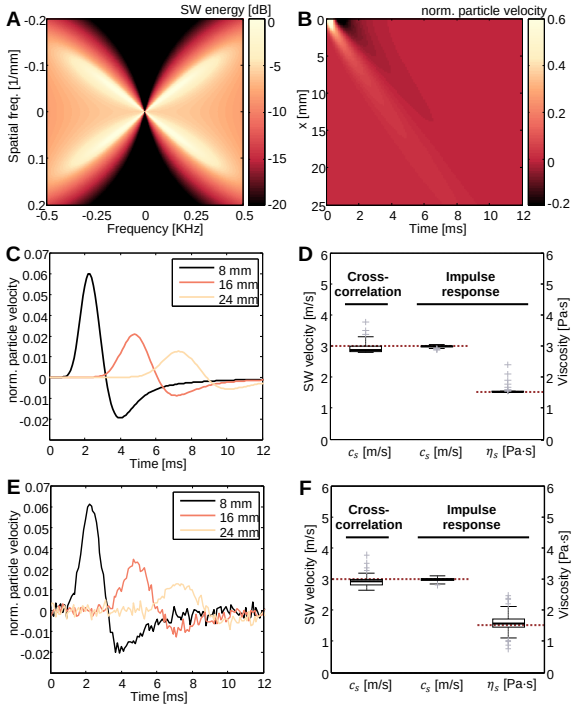

Figure 7.2: Simulation of shear wave (SW) propagation in a viscoelastic material with μ_0 = 9 kPa, ρ = 1000 kg/m^3, and η_s = 1.5 Pa·s based on.[218] In (A), the generated 2D Fourier domain SW data is shown and (B) gives the resulting particle velocity in the space-time domain. In (C,E), several particle velocity signals at different lateral positions are shown as a function of time, with and without additive Gaussian white noise (standard deviation: 5% of peak amplitude at 10 mm), respectively. Then, in (D,F), the resulting SW velocity ($\hat{c}_s = \sqrt{\mu_0/\rho}$) and viscosity estimates along the lateral position are summarized in box-plots. True values are indicated with dotted lines. For comparison, the results for SW velocity estimation based on a cross-correlation approach are also shown.

Mead simplex algorithm.[217] We employed a course grid search across c_s and η_s (10×10) to select appropriate initial conditions. The median number of iterations to reach convergence was 93.

Figure 7.1 gives an illustrative overview of the proposed method.

7.3 Validation Methodology

7.3a Simulation study

The proposed method was first tested on simulated datasets by generating particle velocity measurements based on an analytic description of SW propagation in a viscoelastic medium following a Gaussian excitation as described in.[218] The cylindrically symmetric Gaussian excitation has the following form:

$$\vec{f}(r,t) = W(t)\exp(-|\vec{x}|^2/\sigma^2)\hat{z}, \tag{7.12}$$

where $\hat{z}$ is the unit vector in the axial direction, σ = 1 mm gives the width, and $W(t)$ determines the time profile of the excitation: a rectangular window with a length of T = 333 μs. We adopted a Voigt material model with stiffness μ_0 and viscosity η, and generated 9 realizations of SW particle velocity measurements in materials with different degrees of viscosity.

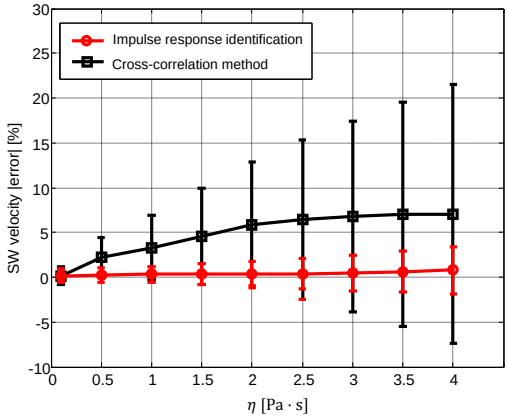

Figure 7.3: Shear wave velocity estimation errors in viscoelastic material simulations as a function of increasing viscosity. Bars indicate standard deviation of estimates across the lateral position. The proposed method is compared to a correlation-based time-of-flight method.

The datasets were then processed as described in Sections 7.2a to 7.2d in order to obtain estimates of SW velocity and viscosity as a function of the lateral position x. Δx was set to 1.25 mm. The results are compared to those obtained using a standard cross-correlation based time-of-flight method for SW velocity estimation[209] with the same Δx, and a two-dimensional Fourier transform (2D-FT) approach for frequency dependent SW phase velocity measurements.[210] The latter first calculates the 2D-FT of the full spatio-temporal SW signal, after which the average phase velocity at a specific temporal frequency is retrieved by locating the spatial frequency at which the 2D-FT is maximized: $c(f) = f/k_{max}(f)$.

7.3b In-vitro study

7.3b.1 Phantom design

In our experiments, commercially available tofu (Unicurd Food Company Pte Ltd., Singapore) served as a typical high-viscosity material. Because its elastographic and echographic properties are similar to those of some soft tissues, this poroelastic soy-based product has been used as a viscous tissue-mimicking phantom.[219] In[220], the effective Poisson's ratio ν of tofu was measured during 600 s of compression, displaying approximate incompressibility ($\nu \approx 0.5$) across the time frame of the measurements performed in our work (10 s). To mimic low-viscosity tissues, water-based 8 weight-% gelatin was prepared.[221,222] It consisted of 20-g gelatin, 9.95-g graphite scattering powder, and 225-mL water. In total, we prepared 3 phantoms from these materials: two homogeneous phantoms (one tofu, one gelatin), and one tofu phantom with a cylindrical gelatin inclusion (diameter of 9 mm).

7.3b.2 SW experiments

The SW experiments were performed as described in Section 7.2a. The data was then processed according to Sections 7.2a to 7.2d, with Δx set to 1.25 mm (i.e. 6 lateral samples).

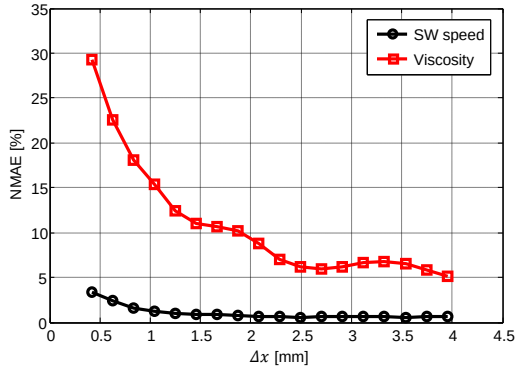

Figure 7.4: Normalized Mean Absolute Error (NMAE) of the shear wave velocity and viscosity estimates as a function of increasing lateral spacing Δx for a simulation with material parameters $\mu_0 = 9$ kPa and $\eta = 3$ Pa · s. Gaussian white noise (standard deviation: 5% of peak amplitude at 10 mm) was added to the particle velocity signals.

7.3b.3 Mechanical characterization

A material's viscoelastic behaviour can be directly estimated by assessing its creep curve, i.e., the time-dependent strain behaviour upon application of a constant load.[219] Considering a 3-parameter material model consisting of a Voigt model with an elastic element in series, the instantaneous response to the compression is regarded as purely elastic, whereas the subsequent creep curve is attributed to the presence of viscosity[221]. The tofu and gelatin phantoms were cut into blocks of similar size (6 cm × 5 cm × 2 cm) and subjected to a pre-compression force of ≈ 0.35 N. Then, their axial strain was monitored after the application of a sudden compressive load of about 200 g (2 N) across the footprint of the L11-4 linear array transducer.

For strain imaging during compression, ultrasound images were acquired at a frame rate of 50 Hz. Large frame-to-frame velocities (> 1 sample/frame) were estimated by block-wise cross correlation of log-compressed B-mode frames (speckle-tracking), and fine sub-sample displacements were captured by estimating the axial velocity from the IQ data using the Loupass 2-D autocorrelator.[215] The ensemble and axial ranges were set to 5 frames and 30 samples, respectively. The axial frame-to-frame displacements were then tracked over time using a Kalman filter[223] to measure the relative strain at a set depth after velocity estimation.

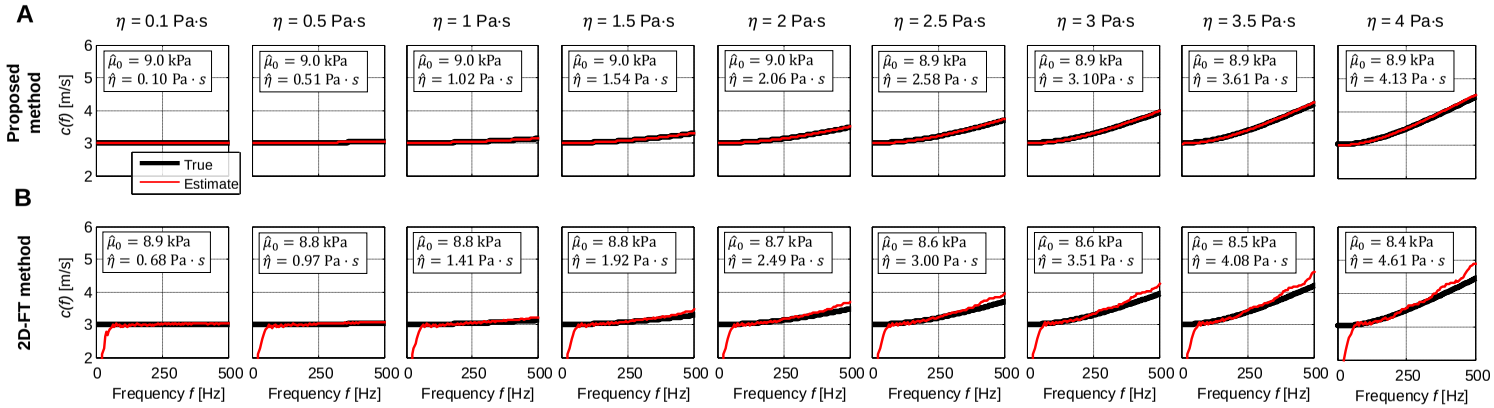

Figure 7.5: Frequency-dependent phase velocity estimates compared to the true values for simulated particle velocity measurements in several Voigt materials (stiffness $\mu_0 = 9$ kPa, mass density $\rho = 1000$ kg/m^3, and varying viscosity $\eta = [0.1 - 4]$ Pa·s). The estimates based on (A) the proposed method and (B) the 2D-FT method described by Nenadic *et al.*[210] are compared. For the latter, Eq. (7.13) is fitted to the phase velocity estimates in a frequency range of 70-500 Hz to obtain $\hat{\mu}_0$ and $\hat{\eta}$.

7.4 Results

7.4a Simulation results

Figure 7.2 displays an example of simulated data based on.[218] SW velocities c_s and material viscosities η_s are estimated along the lateral direction x based on the proposed method, and their distributions are summarized in box-plots (Figure 7.2D). One can observe that the estimates are very close to the true values (c_s = 3 m/s, η_s = 1.5 kPa). Moreover, the SW velocity estimates seem to be slightly improved with respect to those obtained using the correlation-based time-of-flight approach.[209] The improved estimation of SW velocity in simulated data by considering viscosity in the estimation procedure can also be noted from Figure 7.3. The estimates of SW velocity based on the proposed impulse response identification procedure yield lower errors and standard deviations compared to those obtained in a time-of-flight fashion, in particular for high viscosity.

The impact of altering the lateral spacing Δx (throughout this work set to 1.25 mm) on the estimates is shown in Figure 7.4. Overall, the estimation error decreases when increasing Δx, which comes at the price of a reduced spatial resolution.

Figure 7.5 shows different degrees of SW phase-velocity dispersion resulting from various levels of viscosity. The frequency-dependent phase velocities were computed from the median estimates of η_s and c_s along the lateral direction x in the following manner:[218]

$$c(\omega) = \sqrt{\frac{2\left(\mu_0^2 + (\eta_s\omega)^2\right)}{\rho\left(\mu_0 + \sqrt{\mu_0^2 + (\eta_s\omega)^2}\right)}}, \tag{7.13}$$

where the stiffness $\mu_0 = \rho c_s^2$. From the upper row of Figure 7.5, one can notice that the estimates are very close to the true phase velocities for all simulations. The bottom row shows the results of the 2D-FT method[210] applied to the full space-time data. Here, the estimated phase velocities deviate slightly from the true values, in particular for higher frequencies and viscosity.

7.4b In-vitro results

The creep curves presented in Figure 7.6 show how the gelatin and tofu phantoms display different time-strain behaviour. When subjected to a sudden stress, gelatin compresses instantly and shows little to no creep, whereas the tofu phantom creeps significantly and clearly presents more viscous behaviour.

Figure 7.7 summarizes the obtained pixel-based SW velocity and viscosity distributions for both phantoms when applying the proposed method. The SW velocity estimates are compared to those measured using the cross-correlation approach. Moreover, we compared the parameter distributions to the values obtained using the 2D-FT method. In line with the mechanical characterization, the estimated viscosity is significantly higher in tofu than in gelatin, while the velocity (and therefore stiffness) is not significantly different. While these characteristics are confirmed by the 2D-FT method, we notice a difference in the absolute viscosity values that is similar to the 2D-FT bias found in the simulation study (see Figure 7.5). The spread and range of estimated values

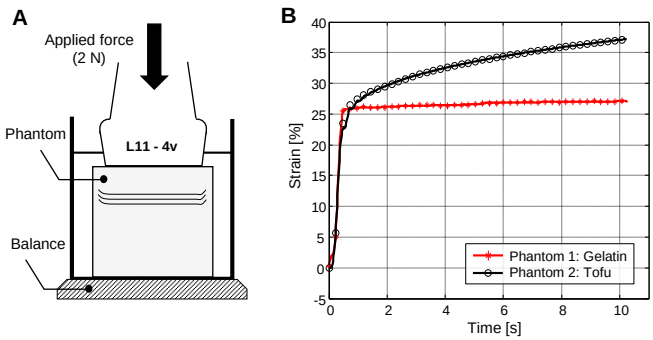

Figure 7.6: (A) Ultrasound strain measurements upon application of a sudden stress. (B) Resulting creep curves for gelatin and tofu phantoms, depicting a higher viscous creep for the latter.

is higher in the tofu phantom as compared to the gelatin phantom.

Finally, viscoelasticity imaging was performed on a tofu phantom containing a cylindrical inclusion of gelatin. The images were post-processed using a 2D median filter (kernel dimensions: 1 mm×3.5 mm) followed by a 2D Gaussian filter (standard deviation: 0.2 mm×0.6 mm). From Figure 7.8, one can appreciate that the less-viscous gelatin inclusion is indeed revealed by the viscosity maps, whereas the velocity images (portraying the purely elastic behaviour) fail to expose it. Where the results obtained with a push-focus on either side of the imaging domain (Figure 7.8B and 7.8C) qualitatively show great similarity in the central zone of the image, one can also observe that the estimates very close the push location and at the far end do not share the same degree of consistency.

7.5 Conclusions and Discussion

In this work, a new approach to determine tissue viscoelasticity based on SW elastography is presented. By locally characterizing SW propagation using a system identification approach, the proposed method enables not only mapping of tissue elasticity, but also of viscosity. The developed technique extends beyond the typical time-of-flight based methods by estimating the kinetics between laterally sampled time-displacement curves instead of just their time-delay.

The algorithm was first tested on simulated datasets, validating its technical correctness with respect to a well-defined ground truth. The assumption of negligible viscosity in a viscoelastic material leads to inadequate estimation of SW velocity based on time-of-flight. On the contrary, by jointly estimating SW velocity and material viscosity, the proposed method appropriately assesses both characteristics (Figure 7.2).

The impact of viscosity on time-of-flight SW velocity estimates was further investigated on a range of simulations with viscous materials (η = 0.1 Pa·s to η = 4 Pa·s). As expected, the presence of viscosity impairs the time-of-flight estimates, yielding high standard deviations along the lateral position. Frequency dependent attenuation causes lower frequencies (and their phase speeds) to become more dominant with increasing distance from the source, introducing a bias that depends on the lateral direction. The proposed method overcomes this issue by adequately modelling the effects of viscosity

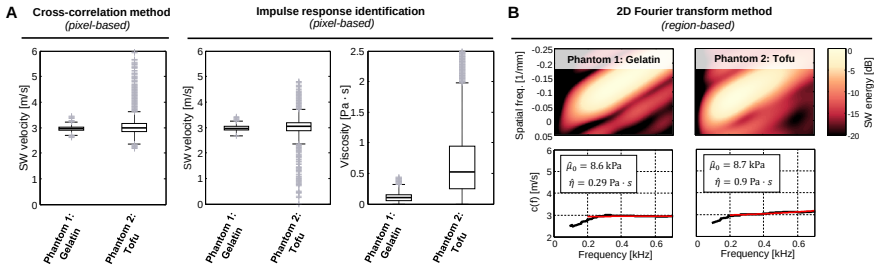

Figure 7.7: (A) Box plots displaying the distributions of pixel-based estimates of shear wave velocity ($\hat{c}_s = \sqrt{\mu_0/\rho}$) and viscosity in gelatin and tofu phantoms as obtained using the proposed method, compared to velocity estimates using a cross-correlation based time-of-flight method. Using cross-correlation, the gelatin phantom yielded shear wave speeds with a median, mean and standard deviation of 2.96, 2.79, and 0.70 m/s, respectively. For tofu, these values were 2.99, 2.87, and 0.79 m/s, respectively. Using the proposed method, the gelatin phantom yielded shear wave speeds with a median, mean and standard deviation of 2.96, 2.80, and 0.71 m/s, respectively. For tofu, these values were 3.04, 2.87, and 0.80 m/s, respectively. The proposed method yielded viscosity values for gelatin with a median, mean and standard deviation of 0.10, 0.11, and 0.08 Pa · s, respectively. For tofu, these values were 0.53, 0.66, and 0.59 Pa · s, respectively. (B) Comparison with the 2D Fourier transform method[210] applied to the entire region.

on SW propagation. As a result, the estimation errors and in particular their standard deviations are much smaller.

On the same range of viscous materials, the resulting phase velocities derived from the estimated material properties showed good agreement with true values (Figure 7.5). Interestingly, we observed that the 2D-FT method for phase velocity dispersion characterization displayed a bias, in particular for higher frequencies (towards 500 Hz) and viscosities. Such a bias was also noted by Rouze *et al.* in.[218] In this regard, we would like to point out that the simulated range of η represents expected viscosities in tissue. In,[224] Wang and Insana investigated the viscoelastic properties of fibroadenomas and carcinomas in rats by extracting and characterizing shear-velocity dispersion curves. Based on a Kelvin-Voigt model, they reported viscosity values that range from $\eta = 0.56 - 3.54$ Pa · s.

Based on the measured *in-vitro* SW data, we found that the method yielded material-property estimates which confirmed the mechanical characterization of the material; tofu and gelatin have similar stiffness, yet very distinct viscosity. We point out that this comparison is qualitative: the material might be well described by a particular viscoelastic model and set of coefficients for one range of frequencies (creep experiment, up to 25 Hz), but then described by the same model with a different set of coefficients over a second, dissimilar, range of frequencies (SW experiment, up to 500 Hz). As noted in Section 7.4b, the spread and range of estimated values was found higher in the tofu phantom as compared to the gelatin phantom. This may originate from substantial material heterogeneity in tofu, which is less evident in gelatin. Moreover, the degraded signal-to-noise level in tofu, which is caused by higher shear attenuation, may have impacted the estimation accuracy and thereby its variance. These practical aspects seem to overwhelm the theoretically-predicted decrease in variance for the SW velocity estimates by the proposed method, as observed in the simulation study.

By imaging a gelatin phantom with a cylindrical tofu inclusion, we showed that the

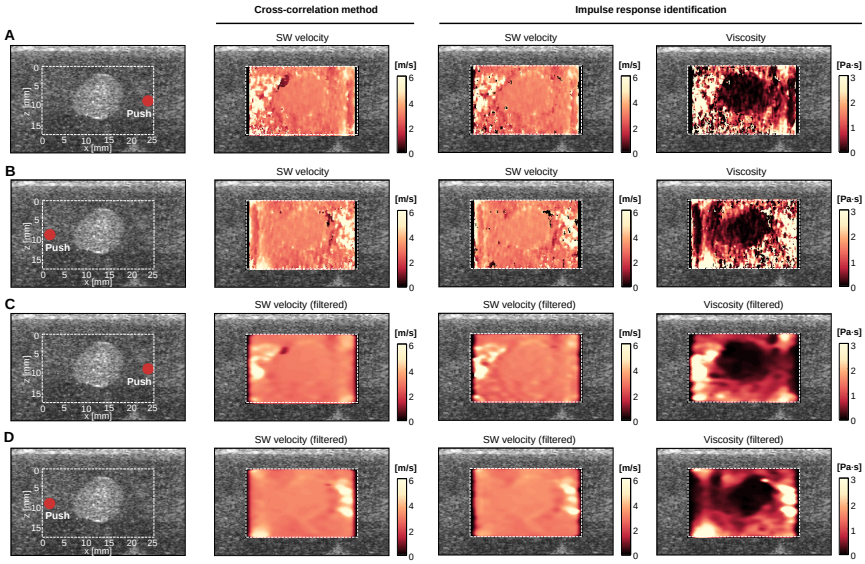

Figure 7.8: Proposed shear wave viscoelasticity imaging on a tofu phantom containing a cylindrical inclusion of gelatin, as compared to a typical correlation-based time-of-flight elastographic approach. The results are given without (A,B) and with spatial filtering (B,C). The maps obtained using an acoustic push focus positioned on the right lateral side (A,C) are compared to those obtained with a push on the left lateral side (B,D).

method is able to generate a viscosity map that reveals the inclusion. The possibility of yielding such a viscosity map using ultrasonic SW elastography was already discussed in,[216] where Bercoff *et al.* contemplated that adding viscosity maps in SW imaging could be of great interest for tumour characterization.

The artifacts in the viscosity maps that appear close to the acoustic push focus (Sec. 7.4b) occur when estimating the model parameters from data in the SW near-field. We may speculate that these artifacts originate from:

1. Non-plane wave propagation in the near-field; a condition for which our 1D model does not hold.
2. The fact that the push-pulse is not a delta-Dirac in space, leading to the presence of an additional apparent "source" between the two lateral positions from which the impulse response is assessed. This violates the assumption that those two points only record a passing SW and all measured axial displacement originates from this propagating wave.

At the lateral far end, we also observe the presence of estimation artifacts. Here, wave aberration and low signal-to-noise ratio are likely degrading the estimates. The aforementioned artifacts can be mitigated by proper combination of estimates from several SW measurements obtained using different lateral push foci.[225] Reliability can be assessed based on location (e.g. close to the push-focus) and signal quality. Such a multi-focus strategy can also be pursued in the axial direction to cover a wide spatial range.

Compared to other methods that aim at assessing viscosity from SW measurements, we like to stress that the proposed method is able to generate estimates in a pixel-based point-to-point fashion. This approach enables the generation of SW maps with a lateral resolution that is primarily determined by the adopted spacing between these points (in this work $2\Delta x$). Choosing a suitable Δx amounts to a trade-off. Decreasing Δx leads to fine estimates, close to the lateral resolution of the US acquisition. Yet, increasing Δx results in a more pronounced effect of the local material properties on the kinetics between the two points, accommodating a more robust estimation procedure in the presence of noise (see Figure 7.4) and a higher sensitivity. The appropriate value depends on the application; for tumour localization a resolution in the order of millimetres is required,[226] whereas characterization of diffuse hepatic steatosis may permit assessment on a larger scale.[227]

The work presented in this paper shows parallels with[214], where Langdon *et al.* describe a method that employs two laterally-spaced push pulses to generate two time-displacement curves at a single tracking location. These curves are then used to estimate the material parameters of the material between the two push-foci. Where such an approach requires two push pulses for each lateral position at which one desires to estimate the viscoelastic parameters, our method only requires one push pulse to generate a full map of the viscoelastic parameters.

To confirm the practical utility of the prosed method, it should be tested extensively on real tissue. Such tests can initially be conducted *ex-vivo*, but should eventually lead to *in-vivo* experiments. In these conditions, the impact of noise, diffraction and aberration, along with other disturbances, should be carefully investigated. The proposed method was applied to particle velocity signals which yield reduced low-frequency (motion) artifacts and a stronger signal morphology which is dominant on a more compact temporal support compared to displacement signals. Yet, particle velocity estimates are more susceptible to high frequency noise and hence require the use of more robust estimators. Although the method presented in this work was applied to SW data obtained from a single push pulse, one can imagine that the high *in-vivo* demands require strategies such as supersonic SW generation and SW compounding.[204] The former produces an intense source by generating shear waves that interfere constructively along a Mach cone to boost the signal-to-noise ratio. The latter combines the results from multiple shear waves to improve reliability of the estimates. Application of the proposed method in such a fashion is straightforward.

Besides improving the method reliability using a high-quality SW dataset, we can also resort to more advanced system identification techniques based on maximum-likelihood estimators that take full advantage of the expected noise statistics to yield robust parameter estimates. Such approaches require a careful design of the noise model for SW displacement signals, taking into account the full acquisition chain from the push source to the (Loupass) displacement estimator and any subsequent pre-processing.

Although the results presented herein were obtained assuming a Voigt material model, the approach can be readily generalized to facilitate characterization in terms of other viscoelastic material models, such as the typically adopted Maxwell or 3-parameter model. One would then merely need to select the appropriate frequency dependent shear modulus $\mu(\omega)$, and solve the minimization problem as described in Eq. (7.11) for the corresponding material parameters. It should be noted, however, that the

optimization procedure for a 3-parameter model with 2 stiffness constants is most-likely more challenging than for the 2-parameter Maxwell and Voigt models.

If the proposed method's applicability is confirmed *in-vivo*, it could in principle be readily implemented on any SW device without requiring hardware changes. This would open up new possibilities for the detection and characterization of pathologies based on their local viscoelasticity.

7.6 Acknowledgements

This research has received funding from the European Research Council / ERC grant agreement n. 280209, and was carried out in the framework of the IMPULSE2 program as a collaboration between Eindhoven University of Technology and Philips Research.

8

Ultrasound Coefficient of Nonlinearity Imaging

Abstract - *Imaging the acoustical coefficient of nonlinearity, β, is of interest in a number of healthcare interventional applications. It is an important feature that can be used for discriminating tissues. In this paper, we propose a nonlinearity characterization method that aims to locally estimate the coefficient of nonlinearity. The proposed method is based on a 1D solution of the nonlinear lossy Westervelt equation, thereby deriving a local relation between β and the pressure wave field. Based on several assumptions, a β imaging method is then presented that is based on the ratio between the harmonic and fundamental fields, therefore reducing the effect of spatial amplitude variations of the speckle pattern. By testing the method on simulated ultrasound pressure fields and an in vitro B-mode ultrasound acquisition, we show that the designed algorithm is able to estimate the coefficient of nonlinearity, and that the tissue types of interest are well discriminable. The proposed imaging method provides a new approach to β estimation, not requiring a special measurement setup or transducer, that seems particularly promising for in vivo imaging.*

Based on: R.J.G. van Sloun, L. Demi, C. Shan, and M. Mischi,"Ultrasound Coefficient of Nonlinearity Imaging", *IEEE Transactions on Ultrasonics, Ferroelectrics, and Frequency Control.*, vol. 62, No. 7, ©IEEE, 2015.

8.1 Introduction

Imaging the nonlinear propagation of ultrasound through tissue is of interest in a number of healthcare interventional applications. The acoustical coefficient of nonlinearity β, characterizing the nonlinear propagation of ultrasound through tissue, is an important feature that may be exploited for discriminating tissues[228] .

A promising application area for β imaging lies in the area of cancer detection and localisation. Compared to healthy tissue, cancer typically displays a greatly increased amount of tissue fluid, which is poorly drained and highly restricted.[73] The coefficient of nonlinearity β was shown to be influenced by the water content of tissue,[74] and its estimation can hence be considered in this context.

Besides the possibilities of employing β for tissue discrimination, using it to obtain information about temperature variations might also be possible[229]. Monitoring temperature variations could for instance be utilized during e.g. High Intensity Focused Ultrasound and Hyperthermia for cancer treatment. The possible alternative application of β estimation to temperature estimation is however not discussed in detail in this article, as tissue characterization is the main focus.

Estimation of the coefficient of nonlinearity in a clinical setting is most applicable using a single probe in pulse-echo mode. In[230], a β estimation method based on a high-frequency probe and pump waves propagating in opposite directions was suggested. However, requiring an acoustic reflector plane limits its practical use. Other possibilities for coefficient of nonlinearity imaging in echo mode have been studied in,[76] where extensions of the Direct,[231] Comparative[78] and Second-Order Ultrasound Field (SURF)[77] methods are derived such that they are applicable to echo mode imaging. The Direct method is the easiest, based on the second harmonic amplitude propagation theory proposed by Zang and Gong.[232] The SURF method relies on multi-frequency transmission requiring a special transducer and the Comparative method requires a particular setup where propagation through an inhomogeneous medium is compared to a known homogeneous reference. The authors in[76] conclude that the Comparative method, and the extension that compensates for inhomogeneous attenuation, is most promising and an alternative application based on high frame rate compounding of plane wave transmissions has been presented in[233]. However, both the SURF as well as the extended Comparative method are not directly feasible for *in vivo* US imaging. The fact that the Comparative method requires the presence of an area where the coefficient of nonlinearity is constant throughout the entire imaging depth poses serious limitations for the method's translation into clinical application. Also, inaccurate a priori knowledge of the attenuation coefficient in the spatial domain leads to cumulative errors in nonlinearity estimation.

In this paper, we propose a tissue nonlinearity imaging method that provides a new and local approach to β estimation, reducing cumulative errors. The influence of scatterer distribution variations is also addressed by considering the ratio between the harmonic and fundamental fields. The proposed method is based on a 1D solution of the nonlinear lossy Westervelt wave equation and does not require a special measurement setup or transducer, making it particularly promising for *in vivo* imaging. Its feasibility is shown by a detailed *in silico* analysis as well as initial *in vitro* results.

The paper is organized as follows. First, the physical background of nonlinear wave propagation through human tissues is given (Sec. 8.2a). Then, a method for extracting the coefficient of nonlinearity β from both the complete pressure wave fields (Sec. 8.2d) as well as echo mode images (Sec. 8.2e) is derived. Next, to assess its performance a numerical *in silico* analysis of pressure wave propagation based on several forms of the wave equations is done. The method is then also tested on an experimental *in vitro* measurement. The numerical and experimental results are given in Secs. 8.3a and 8.3b, respectively. Finally, the results are discussed and conclusions derived (Sec. 8.4).

8.2 Methods

8.2a Physical background of nonlinear wave propagation

As sound waves propagate through tissue, they distort due to medium dependent variation of the speed of sound with respect to pressure, quantified by the coefficient of nonlinearity β. Higher pressure results in an increased speed of sound whereas lower pressure results in a reduced speed of sound. This distortion results in the accumulation of harmonics.[234–236] In Table 8.1, β is given for some human tissues of interest. Also the attenuation coefficient α is given, describing the attenuation of a pressure wave with respect to depth as a result of medium dependent absorption. For the sake of clarity, α is given in both $\mathrm{dB}/(\mathrm{MHz}^y \times \mathrm{cm})$ and $\mathrm{Np}/((\mathrm{rad/s})^y \times \mathrm{m})$ because the latter can be directly substituted in the equations. Comparing the coefficient of nonlinearity β to the attenuation coefficient α, one can notice that the relative differences in β for these tissues are higher, making it an interesting candidate for tissue characterization. Acoustic pressure wave propagation can be compactly described in the form of wave equations, combining conservation of mass and momentum. In this section, we will first give an expression for the lossy nonlinear wave equation. The modification from the lossless linear wave equation is made explicit in the form of distributed sources S.

8.2b Lossy nonlinear wave equation

The general lossy 3D Westervelt wave equation [235, Chapter 3.6] may be written as:

$$\nabla^2 p(\mathbf{x},t) - \frac{1}{c_0^2}\partial_t^2 p(\mathbf{x},t) = -S_{at}[p(\mathbf{x},t)] - S_{nl}[p(\mathbf{x},t)], \tag{8.1}$$

where

$$S_{nl}[p(\mathbf{x},t)] = \frac{\beta(\mathbf{x})}{\rho_0 c_0^4}\partial_t^2 p^2(\mathbf{x},t) \tag{8.2}$$

denotes the nonlinear source.[196] The effects of attenuation, represented by $S_{at}[p(\mathbf{x},t)]$, can be modelled by explicitly introducing relaxation in the medium behaviour. Then, the following attenuation source is obtained:[237]

$$S_{at}[p(\mathbf{x},t)] = -\frac{1}{c_0^2}\partial_t^2 \left[A(\mathbf{x},t) *_t p(\mathbf{x},t)\right], \tag{8.3}$$

Table 8.1: Properties of some relevant tissues as described by [195, Appendix B].

Tissue	$\alpha[\mathrm{dB}/(\mathrm{MHz}^y \times \mathrm{cm})]$	$\alpha[\mathrm{Np}/((\mathrm{rad/s})^y \times \mathrm{m})]$	y	β
Fat	0.6	$1.10 \cdot 10^{-6}$	1*	6.1
Heart†	0.52	$0.95 \cdot 10^{-6}$	1*	3.9
Muscle	0.57	$1.04 \cdot 10^{-6}$	1*	4.7

*: Assumed value. † Heart mainly consists of muscle and blood.

where $*_t$ denotes the time domain convolution and $A(\mathbf{x}, t)$ describes the delayed response of the medium; its low pass filtering property. Attenuation through tissue is assumed to obey a power law dependence on frequency.[238, 239] As suggested in,[196, 240] a suitable representation of $A(\mathbf{x}, t)$ can be given in the Laplace domain:

$$\hat{A}(\mathbf{x}, s) = \left\{ 1 + \frac{c_0 \alpha_0(\mathbf{x}) s^{y(\mathbf{x})-1}}{\cos[\pi y(\mathbf{x})/2][1 + (s/s_{max})^d]} \right\}^2 - 1, \tag{8.4}$$

where $\alpha_0(\mathbf{x})$ is the attenuation coefficient in $\mathrm{Np} \cdot (\mathrm{rad/s})^{-y} \cdot \mathrm{m}^{-1}$, ω is the angular frequency in rad/s, $y(\mathbf{x})$ is the power law exponent that may not be an odd integer, and the factor $[1 + (s/s_{max})^d]$ ensures causality and finite wave speed, with s_{max} being a parameter larger than the maximum angular frequency of interest and d being a parameter that is larger than $y(\mathbf{x}) - 1$. The propagation coefficient $\hat{\gamma}(\mathbf{x}, s)$ is then given as

$$\hat{\gamma}(\mathbf{x}, s) = \frac{s}{c_0} \sqrt{\hat{A}(\mathbf{x}, s) + 1}. \tag{8.5}$$

After setting $s = j\omega$, we observe that the function $\hat{\gamma}(\mathbf{x}, \omega)$ consists of an attenuation and phase coefficient that can be approximated by[196]

$$\hat{\gamma}(\mathbf{x}, \omega) \approx \alpha_0(\mathbf{x}) |\omega|^{y(\mathbf{x})} + j \left[\frac{\omega}{c_0} + a_0(\mathbf{x}) \tan[\frac{\pi}{2} y(\mathbf{x})] \omega |\omega|^{y(\mathbf{x})-1} \right], \tag{8.6}$$

where the second term of the imaginary part describes the effects of dispersion.

8.2c Solution using Green's function

The solution of the lossy nonlinear wave equation with inclusion of a primary source term $S_{pr}(\mathbf{x}, t)$,[196] that models the effects of the transducer, can be formulated as an integral equation:

$$p(\mathbf{x}, t) = G(\mathbf{x}, t) *_{\mathbf{x},t} \{ S_{pr}(\mathbf{x}, t) + S_{nl}[p(\mathbf{x}, t)] + S_{at}[p(\mathbf{x}, t)] \}. \tag{8.7}$$

Here, $*_{\mathbf{x},t}$ denotes the convolution over space and time and $G(\mathbf{x}, t)$ is the Green's function of the lossless linear wave equation, given by

$$G(\mathbf{x}, t) = \frac{\delta\left(t - \frac{||\mathbf{x}||}{c_0}\right)}{4\pi ||\mathbf{x}||}, \tag{8.8}$$

where the $||\cdot||$ operator gives the length of a vector and $\delta(\cdot)$ denotes the Dirac delta function. In 1D, one can show that the Green's function is given by

$$G(x,t) = \frac{c_0}{2} H\left(t - \frac{|x|}{c_0}\right), \tag{8.9}$$

with $H(\cdot)$ being the Heaviside step function. The 1D version of Eqn. (8.7) can be written as

$$p(x,t) = p^{(0)}(x,t) + G(x,t) *_{x,t} \left\{S_{nl}[p(x,t)] + S_{at}[p(x,t)]\right\}, \tag{8.10}$$

where

$$p^{(0)}(x,t) = G(x,t) *_{x,t} S_{pr}(x,t) \tag{8.11}$$

denotes the linear lossless solution.

8.2d β Estimation based on the pressure wave field

We start this analysis by assuming that the pressure wave field is generally observable. To obtain a relation between the coefficient of nonlinearity $\beta(x)$ and the pressure wave field $p(x,t)$ we will first derive an expression of the harmonic pressure field. This is done by analysing the Green's function based contrast source solution of the 1D lossy nonlinear Westervelt equation (Eqn. (8.10)). Rewriting the total field as a combination of the fundamental and the harmonic field, i.e.

$$p(x,t) = p_f(x,t) + p_h(x,t), \tag{8.12}$$

we can reformulate Eqn. (8.7):

$$\begin{aligned} p(x,t) =& p^{(0)}(x,t) + G(x,t) *_{x,t} S_{nl}[p(x,t)] \\ &+ G(x,t) *_{x,t} S_{at}[p_f(x,t) + p_h(x,t)], \end{aligned} \tag{8.13}$$

and, realizing that the fundamental field can be approximated by a combination of the lossless linear field $p^{(0)}(x,t)$ and the attenuation source, assuming energy loss of the fundamental component due to harmonic generation to be negligible with respect to loss due to absorption, i.e.

$$p_f(x,t) \approx p^{(0)}(x,t) + G(x,t) *_{x,t} S_{at}[p_f(x,t)], \tag{8.14}$$

and exploiting linearity of the attenuation contrast source, we obtain

$$\begin{aligned} p_h(x,t) =& G(x,t) *_{x,t} \frac{\beta(x)}{\rho_0 c_0^4} \partial_t^2 p^2(x,t) - \\ & G(x,t) *_{x,t} \frac{1}{c_0^2} \partial_t^2 \{A(x,t) *_t p_h(x,t)\}. \end{aligned} \tag{8.15}$$

Using Eqn. (8.9) and exploiting the commutative property of the convolution we obtain

$$\begin{aligned} p_h(x,t) =& \frac{c_0}{2} H\left(t - \frac{|x|}{c_0}\right) *_{x,t} \frac{\beta(x)}{\rho_0 c_0^4} \partial_t^2 p^2(x,t) - \\ & \frac{c_0}{2} H\left(t - \frac{|x|}{c_0}\right) *_{x,t} \frac{1}{c_0^2} \partial_t^2 \{A(x,t) *_t p_h(x,t)\} \\ =& \frac{1}{2\rho_0 c_0^3} \delta\left(t - \frac{|x|}{c_0}\right) *_{x,t} \beta(x) \partial_t p^2(x,t) - \\ & \frac{1}{2c_0} \delta\left(t - \frac{|x|}{c_0}\right) *_{x,t} \{\partial_t A(x,t) *_t p_h(x,t)\}. \end{aligned} \tag{8.16}$$

Then, considering $x \geq 0$ and working out the spatiotemporal convolution integrals leads to

$$\begin{aligned} p_h(x,t) =& \frac{1}{2\rho_0 c_0^3} \int_0^x \beta(x') \partial_t p^2(x',t) dx' \\ & - \frac{1}{2c_0} \int_0^x \partial_t A(x',t) *_t p_h(x',t) dx'. \end{aligned} \tag{8.17}$$

The final step is to take the derivative of Eqn. (8.17) with respect to x, thereby using the fundamental theorem of Calculus,[241] such that

$$\partial_x p_h(x,t) = \frac{\beta(x)}{2\rho_0 c_0^3} \partial_t p^2(x,t) - \frac{1}{2c_0} \partial_t A(x,t) *_t p_h(x,t). \tag{8.18}$$

Rewriting Eqn. (8.18) yields

$$\partial_x p_h(x,t) + S_a[x,t,\alpha_0(x)] = \frac{\beta(x)}{2\rho_0 c_0^3} \partial_t p^2(x,t), \tag{8.19}$$

where

$$S_a[x,t,\alpha_0(x)] = \frac{1}{2c_0} \mathcal{F}^{-1}\left\{ j\omega A(x,\omega) \mathcal{F}\left\{p_h(x,t)\right\}\right\}, \tag{8.20}$$

with $\mathcal{F}\{\cdot\}$ and $\mathcal{F}^{-1}\{\cdot\}$ denoting the Fourier transform and its inverse, respectively. With the assumption that the pressure wave fields $p(x,t)$ and $p_h(x,t)$ are completely observable, the sampled version of Eqn. (8.19) can thus be solved for $\beta(x)$ using least squares optimization.

8.2e β Imaging in echo mode

For echo mode US, only echoes of the pressure wave field $p(x,t)$ are observable. These echoes may overlap, resulting in constructive and destructive interference. This significantly increases the difficulty of estimating β, and in this section a specific solution is presented which is derived based on several assumptions. First of all, we assume that the acoustic wave returning from the tissue boundary to the transducer propagates linearly, which is justified by its lower pressure amplitude. Furthermore, in the final imaging algorithm we only consider the second harmonic, and we neglect dispersive effects. For

Table 8.2: Overview of simulation settings for the numerical results.

#	Medium	Simulator	Dimensions	Excitation	f_0 [MHz]	Attenuation	Dispersion	β estimation	Figure
A.	1	Burgers	1D	Plane wave	1	Yes	No	Least Squares sol. of Eqn. (8.19)	Fig. **??**
B.	1	INCS	1D	Plane wave	1	Yes	Yes	Least Squares sol. of Eqn. (8.19)	Fig. 8.1
C.	2	INCS	3D	Plane wave	1	No	No	Least Squares sol. of Eqn. (8.19)	Fig. 8.2
D.	3	INCS	3D	Single element	1	Yes	Yes	Echo mode imaging method	Fig. 8.3
E.	3	INCS	3D	Linear array scan	1	Yes	Yes	Echo mode imaging method	Fig. 8.3

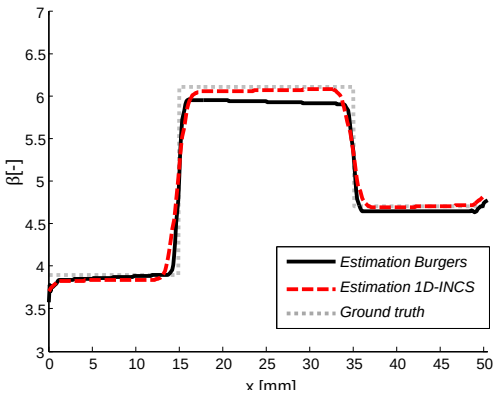

Figure 8.1: Medium 1, Simulators: Burgers Equation and 1D-INCS. β estimation using the Least Squares solution of Eqn. (8.19). A comparison between the results for pressure data simulated using Burgers equation at 1 MHz (blue) and 1D-INCS at 1 MHz (green). The red dashed line indicates the ground truth β.

backscattered US signals, β estimation is strongly dependent on spatial variations of scattering. To compensate for this phenomenon, we adopt an additional assumption, i.e. variations in the speckle pattern are similar for harmonic and fundamental components. We then consider relating β to the harmonic ratio through a function $f\{\cdot\}$, i.e

$$\beta(x) = f\left\{\frac{\hat{p}_h(x)}{\hat{p}_f(x)}\right\}, \tag{8.21}$$

where $\hat{p}_f(x)$ and $\hat{p}_h(x)$ denote the peak pressure of the fundamental and second harmonic envelopes in the time domain over depth, respectively. Such an expression can be obtained by analysing the derivative of the ratio $\frac{p_h(x,t)}{p_f(x,t)}$ with respect to x, allowing us to write

$$\left[\frac{p_f(x,t)}{p_h(x,t)}\right]\partial_x\left[\frac{p_h(x,t)}{p_f(x,t)}\right] = \frac{\partial_x p_h(x,t)}{p_h(x,t)} - \frac{\partial_x p_f(x,t)}{p_f(x,t)}. \tag{8.22}$$

Combining Eqns. (8.22) and (8.18), and considering the assumptions stated before, Eqn. (8.22) can be expressed (see Appendix 8.5) in terms of $\hat{p}_f(x)$ and $\hat{p}_h(x)$ as

$$\left[\frac{\hat{p}_f(x)}{\hat{p}_h(x)}\right]\partial_x\left[\frac{\hat{p}_h(x)}{\hat{p}_f(x)}\right] = \frac{\beta(x)\omega_o}{2\rho_o c_o^3}\frac{\hat{p}_f^2(x)}{\hat{p}_h(x)} - \frac{\omega_o}{c_o}\left[|A(x,2\omega_o)| - \frac{1}{2}|A(x,\omega_o)|\right], \tag{8.23}$$

where

$$A(x,\omega) = \frac{\alpha_o^2(x)c_o^2|\omega|^{2y(x)}}{\omega^2} - j\frac{2\alpha_o(x)c_o|\omega|^{y(x)}}{\omega}. \tag{8.24}$$

The resulting expression for $\beta(x)$ can then be derived as

$$\beta(x) \approx \left(\frac{2\rho_o c_o^3}{\omega_o \hat{p}_f(x)}\right)\left\{\partial_x\left[\frac{\hat{p}_h(x)}{\hat{p}_f(x)}\right] + \frac{\omega_o}{c_o}\left[|A(x,2\omega_o)| - \frac{1}{2}|A(x,\omega_o)|\right]\left[\frac{\hat{p}_h(x)}{\hat{p}_f(x)}\right]\right\}. \tag{8.25}$$

We will refer to this as the echo mode imaging method.

8.3 Results

8.3a Numerical Results

In this section, the derived methods are applied to simulated ultrasound fields considering several situations, referred to as simulations *A* to *E*. An overview of the numerical analysis is given in Table 8.2. We start with plane waves applied to simple 1D structures and gradually increase the complexity to eventually a finite aperture single-element transducer as well as a linear array scanning setup. The plane wave simulations (*A*, *B*, *C*) are analysed by solving the sampled version of Eqn. (8.19) for $\beta(x)$ using least squares optimization (Sec. 8.2d) whereas the echo mode imaging method (Sec. 8.2e) is used for the single element (*D*) and the linear array scan (*E*) simulations. The resulting Root Mean Squared Errors (RMSE) of the β estimation over space for all simulations are given in Table 8.3, were the RMSE is shown in terms of absolute β.

8.3a.1 General settings

First, Burgers equation is exploited as it is a recognized and simple description for 1D progressive plane waves.[242] Dispersive effects are not modelled. Then, the Iterative Nonlinear Contrast Source (INCS) approach[240] is used. INCS is based on an iterative solution of Eqn. (8.10), and is capable of simulating 3D pressure fields and modelling dispersive effects, as opposed to Burgers equation. For all simulations, the transmitted US pulse is given by:

$$p_{pulse} = p_0 \sin(2\pi f_0 t) e^{-\frac{(2t)^2}{T_w^2}}, \tag{8.26}$$

where $p_0 = 1$ MPa is the peak pressure, $f_0 = 1$ MHz is the fundamental frequency of the sinusoid, and $T_w = 6/f_0$ limits the pulse duration to 6 cycles. The chosen simulation source pressure is realistic for real imaging applications, see[243] where peak negative pressures on the order of -1.5 MPa have been measured in water for the ULA-OP scanner.

The speed of sound c_0 and mass density ρ_0 are assumed constant, being 1540 m/s and 1000 kg/m^3, respectively. In the algorithm, the attenuation coefficient is globally set to $\hat{\alpha}_0(x) = 0.57\text{dB}/(\text{MHz}^y \times \text{cm})$ and $y = 1.0001$ (it may not be an odd integer, see Eqn. (8.4)), if not stated otherwise. Because of numerical and real physical constraints (transducer bandwidth), only harmonics up to third order are considered. All spatial derivatives are implemented using Gaussian derivatives.[244]

The nonlinear media used throughout the simulations represent heart, fat and muscle tissue. Their attenuations and coefficients of nonlinearity are given in Table 8.1.

8.3a.2 Plane wave excitation (Burgers)

For this simulation, we consider three distinct tissue layers where the coefficients of nonlinearity $\{\beta_1, \beta_2, \beta_3\} = \{3.9, 6.1, 4.7\}$ and attenuation $\{\alpha_1, \alpha_2, \alpha_3\} = \{0.52, 0.60, 0.57\}$ in dB/(MHz$^y \times$ cm) are chosen such that they represent heart, fat, and muscle tissue, respectively. Here, we consider a simulation with $\{\Delta x_1, \Delta x_2, \Delta x_3\} = \{15, 20, 15\}$ mm based on Burgers equation. Fig. 8.1 shows the obtained $\beta(x)$ plot. Since Burgers equation does not model dispersion, it is also ignored in the estimation algorithm. That is,

the imaginary part of the propagation coefficient is set to ω/c_0 for these experiments.

8.3a.3 Plane wave excitation (1D-INCS)

Here, the method is tested by applying it to a simulation with the configuration described in Sec. 8.3a.2, now simulated using 1D-INCS, thereby considering dispersion. Fig. 8.1 shows the obtained $\beta(x)$ plot. Although the estimated nonlinearity is close to the ground truth, the effects of not knowing all harmonic terms and using a constant attenuation for all x can be observed. The resulting RMSEs for simulations A and B are similar (Table 8.3).

8.3a.4 Plane wave excitation (3D-INCS)

In this simulation we still consider plane wave excitation, but applied to a medium structure having 3D spatial variations. Fig. 8.2 shows the fields as well as the obtained β for a slice of the field simulated using 3D-INCS.[237] The region between the two dashed circles corresponds to a lossless nonlinear medium with $\beta = 4.38$, whereas the background is lossless and linear, i.e. $\beta = 0$. $\hat{\alpha}_0$ is thus set to zero in the algorithm. In this 3D simulation, the effects of the diffraction pattern can be seen from the harmonic pressure fields as well as the β image.

The RMSE increases mainly due to the impact of diffraction on amplitude and phase, which is not included in the 1D model Eqn. (8.19) is based on. Therefore, we now move to the proposed echo mode β imaging method. This method does not consider phase changes and is hence less sensitive to the diffraction.

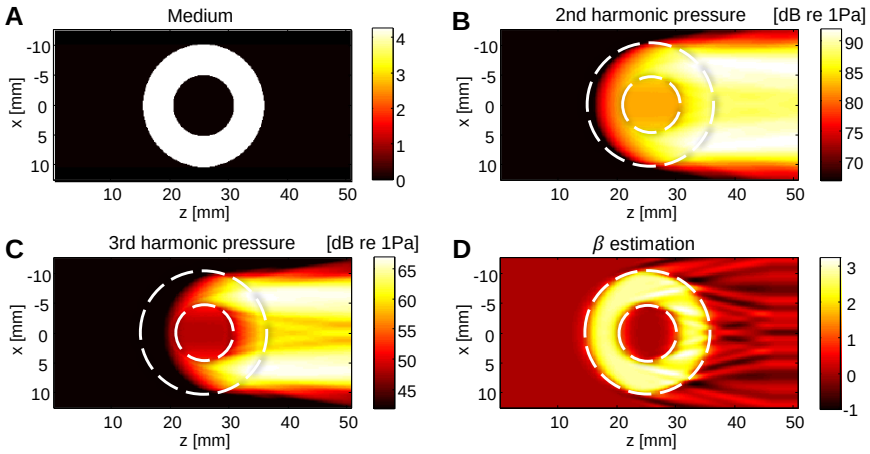

Figure 8.2: Medium 2, Simulator: 3D-INCS, plane wave excitation. β estimation using the Least Squares solution of Eqn. (8.19) for a 3D slice of data. Plot (A) shows the configuration where the colour scale indicates the coefficient of nonlinearity β. Plots (B) and (C) show the second and third harmonic maximum pressure fields, respectively. Plot (D) displays the obtained β map

#	Sim.	Excitation	RMSE
A.	Burgers	Plane wave	0.17
B.	1D-INCS	Plane wave	0.16
C.	3D-INCS	Plane wave	0.77
D.	3D-INCS	Single element*	0.62
E.	3D-INCS	Linear array scan	0.55

Table 8.3: Overview of the numerical analysis and Root Mean Squared Errors (RMSE) of the β estimation over space. $*$:Only values within 3.5 mm of the main beam axis are considered.

Algorithm parameters		RMSE
c_0 [m/s]	α_0 [dB/(MHz^y × cm)]	
1540	0.57	0.55
1540	0.4	0.61
1540	0.7	0.58
1400	0.57	0.85
1600	0.57	0.64

Table 8.4: Influence of algorithm parameters on the Root Mean Squared Errors (RMSE) of the β estimation over space for the linear array scan excitation (E).

8.3a.5 Single element excitation (3D-INCS)

We start by applying the echo mode method to transmission mode data, being a slice of the pressure field simulated using 3D-INCS, employing a rectangular single element having a width and height of 10 mm as source. The structures have contrast in attenuation and nonlinearity, and represent heart, fat, and muscle tissue (values given in Table 8.1). The background medium has an attenuation of 0.52 dB/(MHz^y × cm) and a nonlinearity $\beta = 1$. Fig. 8.3 shows the test configuration where the colour scale indicates the coefficient of nonlinearity β (top plot), as well as the second harmonic pressure field and the estimated β within the main beam (second and third plot respectively). The RMSE is 0.62 (Table 8.3) in the region of interest, which excludes the estimates close to the probe. The region is annotated in Fig. 8.3 (c).

8.3a.6 Linear array scan (3D-INCS)

The final part of this numerical analysis concerns the evaluation of the proposed echo mode β imaging method when considering a 52 element linear array scan, using pressure fields simulated with 3D-INCS. The medium configuration is identical to the one considered in Sec. 8.3a.5. The linear array consists of elements having a pitch of 0.77 mm. For each line, 13 elements are simultaneously excited and a β estimate is obtained within the resulting beam. The nonlinearity image is then formed by stepping along the array (step size: 2 elements) and combining the obtained β values for each scan line. As Fig. 8.3 shows, the original morphology is recognizable from the nonlinearity image (d). Moreover, the obtained β values are close to the ground truth, yielding a RMSE of 0.55 (Table 8.3) within the region of interest. The region is annotated in Fig. 8.3 (d) and (e). The resulting β maps when varying the algorithm parameters c_0 and a_0 are shown in Fig. 8.3 (f) to (j). Absolute β estimates are most affected by strong misestimations in speed of sound, whereas variations in attenuation play a smaller role (Table 8.4).

8.3b Experimental *in vitro* Results

The proposed echo mode β imaging method was tested by acquiring 128 RF lines *in vitro*, using an ULA-OP ultrasound scanner[243], transmitting Gaussian windowed pulses with frequency $f_0 = 3$ MHz and a pulse duration of 6 cycles. The number of active

elements is 64 and the pitch of the Esaote LA332 probe is 0.245 mm. The fundamental

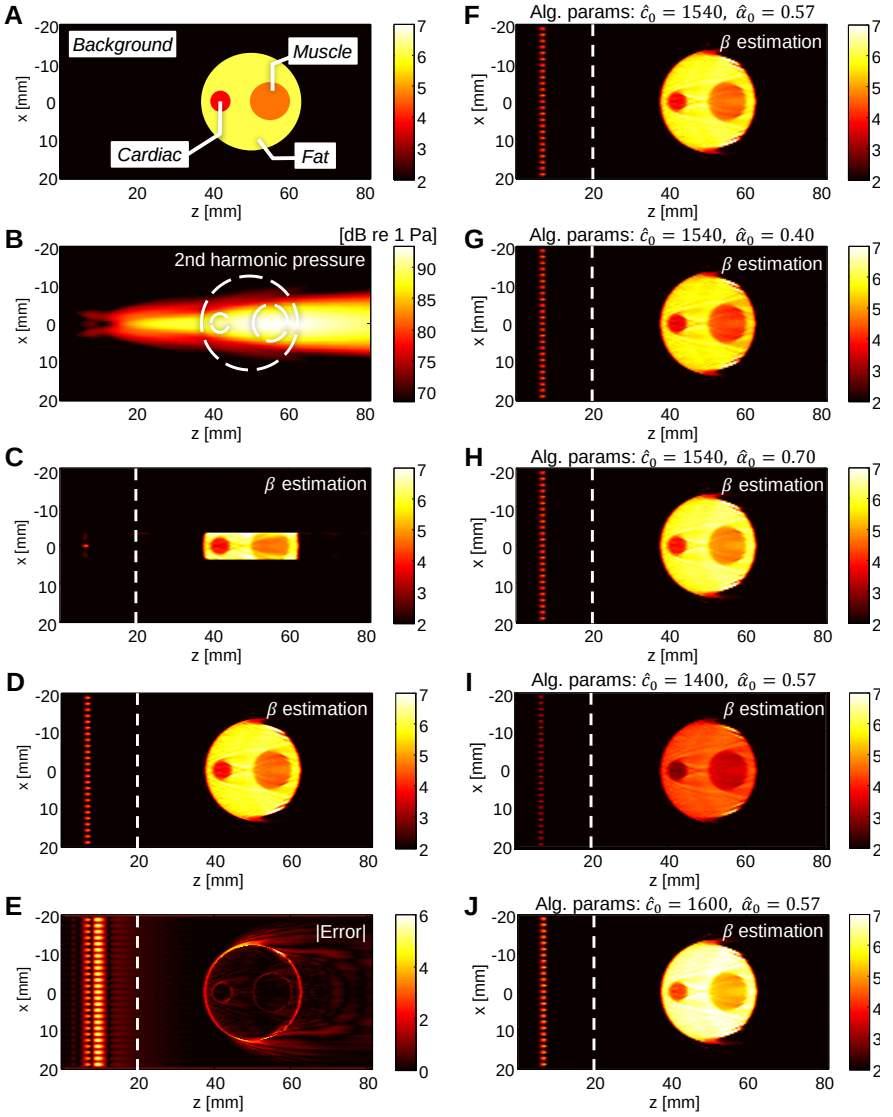

Figure 8.3: Medium 3, Simulator: 3D-INCS, single element and linear array scan excitation. β estimation using the echo mode imaging method for a 2D slice of data. Plot (A) shows the configuration where the colour scale indicates the coefficient of nonlinearity β. Three tissue types are considered, being heart, muscle and fat. Plot (B) shows the second harmonic beam profile for the centre scan line. Plots (C) and (D) show the obtained coefficient of nonlinearity $\beta(x)$ images for the single element within the beam and the linear array scan for the entire domain, respectively. The corresponding absolute error map of the latter is shown in plot (E). The RMSE measures are determined from the region on the right hand side of the dashed line in plot (C), (E), and (E), excluding the strong near field effects. The resulting β maps when varying the algorithm parameters c_0 (given in m/s) and a_0 (given in dB/(MHz^y×cm)) are shown in plots (F) to (J).

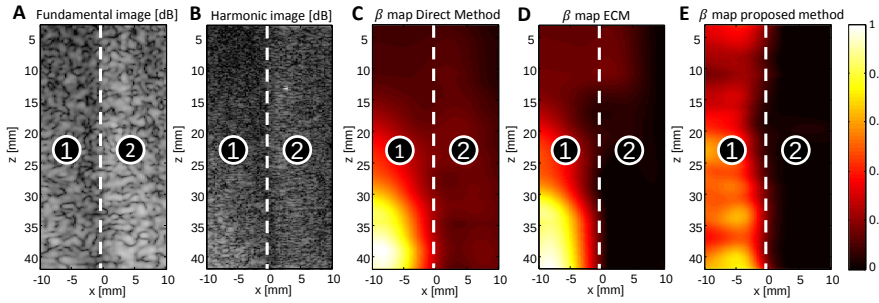

Figure 8.4: β imaging using the echo mode imaging method for experimental *in vitro* data acquired using a linear array. Plots (A) and (B) show the fundamental and 2nd harmonic image, respectively. The resulting β maps for the Direct method,[231] the Extended comparative method (ECM)[76] as well as the proposed harmonic ratio method are shown in plots (C), (D), and (E), respectively. The two phantom layers are annotated by '1' and '2'.

and second harmonic B-mode images are obtained using an 8th order Butterworth band pass filter around f_o = 3 MHz and f_2 = 6 MHz respectively, after which their envelopes are determined by employing the Hilbert transform. A line by line 5 mm moving average (boxcar) filter is applied to both the fundamental and second harmonic image in an effort to obtain continuous estimates of the pressure, weighted by the scatterer distribution. The size has been chosen empirically, being a trade off between the effective axial resolution of the estimator and the ability to cope with differences in summing of sub-wavelength scatterers for the fundamental and second harmonic components in reception. The used phantom combines 2 layers of tissue mimicking material, consisting of corn oil (4% and 50% mass respectively), water (91% and 45% mass respectively), gelatin (4%), and 10-μm aluminium oxide powder scatterers (1%). The layers consisting of 50% and 4% corn oil are referred to as layers 1 and 2, respectively. Corn oil is known to have a high nonlinearity (β = 6.2) and was exploited to obtain contrast.[245] The ratio water to corn oil modifies the β value in a layer. The images, as well as the normalized result of the proposed echo mode β imaging method are shown in Fig. 8.4. The echo mode algorithm (Eqn. (8.25)) has been applied assuming speed of sound c_o = 1540 m/s, mass density ρ_o = 1000 kg/m^3, ω_o = 6π rad/s, attenuation $\alpha_o(x)$ = 0.3dB/(MHz^y × cm) and y = 1.0001 For comparison, the results of the Direct method as well as the Extended Comparative Method (ECM), applied to the filtered second harmonic image, are also given. In this experiment, the ground truth absolute value of β in the two media is unknown, limiting the analysis to qualitative results. However, a relative spatial distribution of β can be observed for all three methods. The ECM seems to give a stronger β contrast between the two media than the Direct method. However, both methods show a strong dependency on depth. Furthermore, the region highlighted most in both maps appears to coincide with the region having the strongest harmonic speckle intensity. The proposed method shows a more homogeneous β distribution for both layers and seems less dependent on propagation depth. In layer 1, the standard deviations of the normalized β maps for the Direct method, the ECM and the proposed method are 0.29, 0.28, and 0.18, respectively. In layer 2, the standard deviations are 0.03, 0.04, and 0.03, respectively

8.4 Conclusions and Discussion

In this paper we proposed a nonlinearity estimation method based on a 1D solution of the inhomogeneous Westervelt equation. By testing the method on simulated ultrasound pressure fields, increasing the complexity of the numerical experiments with each step, we showed that the evaluated tissue types are well discriminable with the designed algorithm by exploiting their contrast in nonlinearity. This was first indicated by the one dimensional results of simulations *A* and *B*, where no diffraction was present. Simulation *C* showed the effects of medium diffraction by exciting a cylindrical object with a plane wave. The effects of finite aperture excitation were analysed using simulation *D*. The transducer's diffraction pattern and its effect on the β image can be observed in the near field, and the results obtained in this region are unreliable. Also, beam spreading as well as medium diffraction are visible, increasingly degrading the shape and accuracy of the β map over depth. The final step in the numerical analysis consisted of a linear array scan (simulation *E*). Again, its accuracy is low in the near field and degrades over depth in the far field, due to diffraction as well the unrealistic assumption of constant attenuation. However, in the region of interest, the morphology as well as the obtained β values were found to be close to the ground truth. Even when the assumptions on attenuation in the algorithm are crude (Fig. 8.3 (i) and (j)), the β estimates are not far off. In particular these results, being a good numerical representation of real B-mode imaging, are promising for the applicability of the proposed echo mode β imaging method.

A limitation of the simulation study lies in the assumption of homogeneous speed of sound c_0, while it in practice may vary considerably. Variations in speed of sound affect harmonics' generation; if wrongly estimated, they affect the β estimate. This is also indicated in Fig. 8.3 (i) and (j). A particularly troublesome case would be one were a medium has a strongly increased speed of sound as well as coefficient of nonlinearity with respect to another medium, making it difficult to distinguish between the two. However, when inspecting the tissues considered in this article, we point out that this situation does not occur. The only relatively strong variation in speed of sound comes from fat, with $c_0 = 1430$ m/s, as compared to heart and muscle, with $c_0 = 1554$ m/s and $c_0 = 1580$ m/s, respectively[195]. In fact, it actually increases the contrast of the apparent coefficient of nonlinearity estimate in this case, making identification of fat an easier task. On the other hand, distinguishing between heart and muscle becomes more challenging.

When comparing this work to other β estimation methods,[76–78] we point out that our method does not require a special transducer or setup, and provides a local estimation of the coefficient of nonlinearity based on the harmonic ratio, which reduces spatial accumulation of errors due to unknown attenuation. We observe that not knowing the attenuation at each point is not necessarily a problem when fluctuations are small, aided by the fact that part of the attenuation is compensated by employing the harmonic ratio. This can also be understood when evaluating the second term on the right hand side of Eqn. (8.25). In the special case of $y = 1$, the amount of attenuation requiring compensation is reduced by a factor two. Moreover, dedicated attenuation estimation algorithms[246–248] could be exploited to provide spatial information on $\alpha_0(x)$. This is particularly useful when considering media with strong contrast in attenuation.

The echo mode imaging algorithm is based on several assumptions. First of all, we assume that the acoustic wave returning from the tissue boundary to the transducer propagates linearly, which is justified by its lower pressure amplitude. Furthermore, in the final imaging algorithm we only consider the second harmonic, and we neglect dispersive effects. The impact of scatterers is addressed and contributions to the derivative term are limited to effects related to the wavelength dependency of scattering. Although speckle intensity variations are assumed similar for the fundamental and harmonic frequencies, there will be errors related to the fact that scattering for fundamental and harmonic frequencies is not equal. This problem requires interpolation or averaging of both fields echo responses, reducing the resolution of the β map. Higher transmission frequencies or shorter pulse lengths can mitigate this problem, but lead to higher attenuation or more overlap between the harmonic and fundamental frequencies, respectively. Although the contribution of speckle intensity variations to the derivative term is minimized, one can note that the estimated β values are still inversely proportional to the speckle intensity in the medium due to the fundamental field factor in the denominator. This type of dependency is however less significant compared to the impact of speckle intensity variations on e.g. the Direct and Comparative methods. For the latter in particular, differences between spatial variation of the speckle intensity in the region of interest and the reference region are highlighted.

Regarding the *in vitro* evaluation, the proposed method shows a more homogeneous β distribution for both layers and seems less dependent on propagation depth compared to the Direct and Extended comparative method. This might be due to the fact both reference methods suffer from significant spatial accumulation of errors due to unknown attenuation. The proposed method is based on the harmonic ratio and uses a different approach that avoids the integral-based attenuation compensation over depth. Although the initial *in vitro* results are promising, further *in vitro* and finally *in vivo* testing is required to evaluate its use for clinical imaging.

The physical arguments and mathematical formulations as well as the detailed numerical analysis described in this work aim at providing a theoretical foundation for β imaging, encouraging future research on practical implementations.

8.5 Appendix: Derivation β Imaging in Echo Mode:

First a description of the spatial derivative of the fundamental field is presented. Using Eqn. (8.14), we can obtain

$$\partial_x p_f(x,t) \approx -\frac{1}{2c_0}\partial_t A(x,t) *_t p_f(x,t), \tag{8.27}$$

thereby discarding the relatively small effect of energy transfer from the fundamental to the harmonic components when compared to energy loss due to attenuation in tissue.

Then, combining this with the result of Eqn. (8.18) and Eqn. (8.22), yields

$$\frac{p_f(x,t)}{p_h(x,t)}\partial_x\frac{p_h(x,t)}{p_f(x,t)} \approx \frac{\beta(x)}{2\rho_o c_o^3}\frac{\partial_t p^2(x,t)}{p_h(x,t)} + \frac{\partial_t A(x,t) *_t p_f(x,t)}{2c_o p_f(x,t)} - \frac{\partial_t A(x,t) *_t p_h(x,t)}{2c_o p_h(x,t)}. \tag{8.28}$$

Next, we assume

$$p(x,t) = \hat{p}_f(x)\sin(\omega_o t) + \hat{p}_h(x)\sin(2\omega_o t), \tag{8.29}$$

neglect any contributions $\omega > 2\omega_o$, and use the following trigonometric identities

$$\sin(x)\cos(x) = \frac{1}{2}\sin(2x), \tag{8.30}$$

$$\cos(2x)\sin(x) = \frac{1}{2}[\sin(3x) - \sin(x)], \tag{8.31}$$

$$\cos(x)\sin(2x) = \frac{1}{2}[\sin(x) + \sin(3x)], \tag{8.32}$$

such that we obtain

$$\begin{aligned}\partial_t p^2(x,t) =& \hat{p}_f^2(x)\omega_o\sin(2\omega_o t) - \hat{p}_f(x)\hat{p}_h(x)\omega_o\sin(\omega_o t)\\ \approx& \hat{p}_f^2(x)\omega_o\sin(2\omega_o t).\end{aligned} \tag{8.33}$$

With reference to the temporal convolutions used in Eqn. (8.28), these can be solved as

$$\partial_t A(x,t) *_t \sin(\omega t) = \omega|A(x,\omega)|\cos[\omega t + \phi_A(x,\omega)]. \tag{8.34}$$

To reduce complexity we neglect dispersion. In this case (recall Sec. 8.2a)

$$\begin{aligned}A(x,\omega) =& \left[\frac{\hat{\gamma}(x,\omega)c_o}{j\omega}\right]^2 - 1 = \left[\frac{\alpha_o(x)c_o|\omega|^{y(x)}}{j\omega} + \frac{\omega}{c_o}\frac{c_o}{\omega}\right]^2 - 1\\ =& \frac{\alpha_o^2(x)c_o^2|\omega|^{2y(x)}}{\omega^2} - j\frac{2\alpha_o(x)c_o|\omega|^{y(x)}}{\omega}.\end{aligned} \tag{8.35}$$

Since $\alpha_o(x)c_o << 1$, $\phi_A(x,\omega) = \arctan\left[\mathrm{Im}(A)/\mathrm{Re}(A)\right] \approx -\pi/2$. Using this together with Eqns. (8.33) and (8.35), Eqn. (8.28) can be rewritten as

$$\begin{aligned}\left[\frac{\hat{p}_f(x)}{\hat{p}_h(x)}\right]\partial_x\left[\frac{\hat{p}_h(x)}{\hat{p}_f(x)}\right] \approx& \frac{\frac{\beta(x)}{2\rho_o c_o^3}\hat{p}_f^2(x)\omega_o\sin(2\omega_o t)}{\hat{p}_h(x)\sin(2\omega_o t)} - \frac{\frac{\omega_o}{c_o}|A(x,2\omega_o)|\hat{p}_h(x)\sin(2\omega_o t)}{\hat{p}_h(x)\sin(2\omega_o t)}\\ &+ \frac{\frac{\omega_o}{2c_o}|A(x,\omega_o)|\hat{p}_f(x)\sin(\omega_o t)}{\hat{p}_f(x)\sin(\omega_o t)},\end{aligned} \tag{8.36}$$

leading to

$$\left[\frac{\hat{p}_f(x)}{\hat{p}_h(x)}\right]\partial_x\left[\frac{\hat{p}_h(x)}{\hat{p}_f(x)}\right] \approx \frac{\beta(x)\omega_o}{2\rho_o c_o^3}\frac{\hat{p}_f^2(x)}{\hat{p}_h(x)} - \frac{\omega_o}{c_o}\left[|A(x,2\omega_o)| - \frac{1}{2}|A(x,\omega_o)|\right]. \tag{8.37}$$

An expression for $\beta(x)$ is then given by

$$\beta(x) \approx \left(\frac{2\rho_0 c_0^3}{\omega_0 \hat{p}_f(x)}\right)\left\{\partial_x\left[\frac{\hat{p}_h(x)}{\hat{p}_f(x)}\right] + \frac{\omega_0}{c_0}\left[|A(x,2\omega_0)| - \frac{1}{2}|A(x,\omega_0)|\right]\left[\frac{\hat{p}_h(x)}{\hat{p}_f(x)}\right]\right\}. \tag{8.38}$$

8.6 Acknowledgements

The authors wish to acknowledge Martin D. Verweij for facilitating the use of INCS and thank Maarten P.J. Kuenen and Harm J.W. Belt for the useful comments and discussion on early drafts of the manuscript. This work is part of the research programme 10769, which is partly financed by the Netherlands Organization for Scientific Research (NWO). The research has also received funding from the European Research Council / ERC grant agreement n. 280209.

Epilogue

9

Mammography and ultrasound: a future perspective

This chapter is based on an editorial article, providing a potential outlook for the role of advanced ultrasound in breast cancer imaging, and its position with respect to mammography.

From: R.J.G. van Sloun, L. Demi, H. Wijkstra, and M. Mischi,"Mammography: developing a smarter and safer alternative", *Future Oncology*, vol. 6, ©Future Medicine Ltd., 2017

To date, mammography remains the golden standard for early detection of breast cancer. Breast cancer is the most common cancer, accounting for about 25% of all cases, in women worldwide.[249] The ability to scan a breast for dense masses using a fast and efficient procedure has led to widespread incorporation of X-ray mammography into cancer screening programs around the world.[34] Mammograms provide the clinician with a two-dimensional (2D) projection of tissue-induced energy attenuation. Dense, highly attenuating structures appear bright, whereas fatty tissues appear dark. Despite these appealing properties, current mammography has its drawbacks.

First of all, the procedure is commonly found unpleasant as a consequence of the strong physical compression required to squeeze the breast between the emitter and detector plates. Secondly, the radiation that illuminates the breast is ionizing. Whilst it should be noted that the clinical gains of imaging as a screening tool are typically worth the risk, X-rays are notorious for their ability to induce DNA mutations. These could ultimately lead to the development of cancer.[35] Generally, a single-view standard mammogram is considered safe enough to be used in routine screening,[250] where the amount of ionizing radiation is limited by restricting the imaging modality to 2D. This poses another limitation: 2D density images often fail to provide sufficient insight to reliably specify bright anomalies as malignant or benign, especially when the breast is generally denser. This condition is more likely to occur in younger women, who have a predominance of dense glandular tissue.[36] Therefore, a positive mammogram requires additional testing to confirm the presence of cancer via e.g. invasive biopsy, magnetic resonance imaging (MRI), or ultrasound imaging (US). Where biopsies are invasive and MRI is costly and time-consuming,[251] US has the potential to shine as a cost-effective, non-invasive technique that can limit the diagnostic burden on the healthcare system and the patient via an effective and accurate imaging protocol.

Over the last three decades US has been providing clinicians with an ever growing set of diagnostic tools, both on the anatomical as well as the functional side. Standard B-mode (or greyscale) imaging gives insight into anatomical structure, and can indicate anomalies such as cysts or solid masses (fibrous nodules or malignancies). B-mode breast US was shown to provide a more accurate diagnosis for pathologies than X-ray mammography in young subjects with dense breasts.[53] Doppler sonography allows functional blood flow imaging by detecting the US Doppler shifts induced by the transport of blood-cells. Using colour Doppler, Yang et al. showed that malignant axillary lymph nodes display significantly higher peripheral flow in 135 woman with primary breast cancer.[55] Contrast-enhanced US (CEUS) enables visualization of microvascular perfusion by administering an intravenous injection of US contrast agents which are then transported along the blood stream. For cancer diagnostics, several quantitative CEUS strategies exist that aim at visualizing tumour-induced angiogenesis, an important marker of cancer disease progression. Angiogenic vasculature is notably chaotic and inefficient, a typical feature that was exploited to localize prostate cancer with CEUS in.[71,143,150] Invasive breast cancers are notoriously stiff compared to benign tissue. Physicians assess nodular firmness by palpation, a subjective technique with a long history in medicine. Today, tissue stiffness can more reliably be evaluated using US elastography.[252] By palpating tissue using the ultrasound probe and consequently tracking the resulting echo displacements over time, tissue strain can be measured and displayed as a measure of elasticity. The applied stress can be imposed mechanically or via acoustic radiation force. A fully quantitative measure of lesion stiffness can be obtained by shear wave elastography (SWE), a method that uses a high-intensity acoustical

push pulse to produce laterally propagating shear waves that can be tracked to obtain the shear velocity, which is in turn related to the Young's modulus. In,[56] SWE and greyscale imaging are used to differentiate benign from malignant solid breast masses, yielding an accuracy of 86% for the detection of malignancy . Finally, ultrasound computed tomography (UCT) enables quantification of pure acoustic parameters such as sound speed and attenuation from their projections across the organ, being time-of-flight and amplitude decay, respectively.[253] This type of acoustical characterization is valuable in the context of tumour-localization, as sound waves travel differently through dense fibrotic structures and tumours as compared to fat. While US is well-known for its inability to effectively penetrate bone, making suitable projections in the human body often hard to acquire, the breast is an organ that is particularly suited for this line of technology.

Although it is reasonable to belief that all these diagnostic options allow a clinician to harvest a broad and useful spectrum of information, the possibilities may be overwhelming, and clinicians rely mostly on experience to select the tools they need. As a consequence, the full potential of US has most likely not been reached. In another domain, an important clinical breakthrough was recently made by the introduction of multi-parametric MRI (mpMRI),[254] in which the rich but complex toolset provided by MRI is exploited by devising diagnostic protocols that combine multiple MRI parameters. With this achievement in mind, it seems logical to translate it to the field of US by incorporating the full set of US tools into a clearly defined multi-parametric protocol (mpUS). The ultimate goal is to provide an operator-independent mpUS solution that suits the clinical workflow, and enables not only the detection of lesions in 3D space, but also their risk-assessment with an accurate BI-RADS (Breast Imaging Reporting and Data System) score.

On the technical side, one can imagine a matrix of US elements (e.g. cylindrical or hemi-spherical) that encapsulates the entire breast, and is able to perform a sequence of experiments based on the US tools described above. Similar transducer systems are already being developed and tested for UCT,[255] and are able to generate reproducible 3D echo (reflectivity) and sound speed images of the breast. The adaptation of the full range of US tools to such a system is another technical challenge that has to be addressed. Its ability to generate high pressure push pulses and perform high frame-rate tracking for SWE, as well as reaching a suitable sensitivity to US contrast agents are vital in this context. With respect to the latter, a feasibility study of dynamic contrast-enhanced UCT has recently been published.[256] After the acquisition phase, all information extraction by the various investigations can be combined in a multi-parametric fashion based on either: 1) a clinician scoring and grading the elements individually and using a scheme that combines these scores into an overall BI-RADS score (as for mpMRI), or 2) machine leaning technology to combine the available information using advanced computer algorithms.[115, 257]

While the availability of such technology would most likely put ultrasound in a very competitive position with respect to other post-screening exams, a major question remains unanswered. Can ultrasound-based technology replace X-ray mammography for screening? This depends on many factors. Is mpUS more accurate than mammography? Is it time-wise feasible in clinical routine? Is it more cost-effective? In this regard, one should evaluate whether all aspects of mpUS should already be incorporated at the screening level. For instance, CEUS requires an intravenous injection of relatively

costly contrast-agents and about 2-minute acquisition time. One may therefore wonder whether a CEUS measurement is feasible for screening.

In any case, the future for US-based technologies looks bright, covering an increasingly broad spectrum of anatomical and functional imaging while retaining the high cost-effectiveness that makes it so appealing.

10

Discussion and Future Prospects

This final chapter provides a critical discussion and conclusion of the research conducted in the thesis, along with future prospects.

In this work, several opportunities for assessment of important cancer markers have been investigated by ultrasound imaging, exploiting features that range from vascular characteristics to tissue behaviour. These aspects are assessed or quantified through dedicated signal processing strategies for various ultrasound modalities. The resulting observations, contributions and main limitations of each of these strategies are discussed separately in the following sections. Finally, general conclusions are drawn and some future prospects are given.

10.1 Vascular markers

The following vascular markers were extracted from clinical dynamic contrast-enhanced ultrasound (DCE-US) acquisitions.

10.1a Assessment of contrast-agent transport kinetics (Chapter 2)

Cancer induces angiogenesis, which in turn alters the hemodynamic conditions of blood flow. We hypothesise that these remodelled conditions have a clear impact on the transport kinetics of ultrasound-contrast-agents. Consequently, assessment of the related transport kinetics should provide relevant information on the presence and extent of angiogenic activity. A well-know parameter to characterize mass transport phenomena in fluid-dynamical systems is the Péclet number: the ratio between convective and diffusive/dispersive transport rates, here being the velocity and dispersion of ultrasound-contrast-agents, respectively. Therefore, in Chapter 2, a new method is proposed that considers the vascular network as a dynamic linear system, whose impulse response can be locally identified. To this end, model-based parameter estimation is employed, permitting extraction of the apparent dispersion coefficient, velocity, and Péclet number of the system.

Main observations and contributions

- With respect to previous methods that aim at characterizing contrast agent bolus dispersion,[71,72,88,98] the proposed approach enabled for the first time independent extraction of UCA dispersion and velocity from DCE-US.
- Malignant areas yielded lower UCA dispersion values, which may be a result of the tortuous nature of angiogenic neovasculature, limiting the dispersion of contrast agents in the measurement cell. This process is very similar to the diffusion of particles through porous media, where a decrease in macroscopic diffusion owing to irregular geometry of the porous media is predicted.[92] The effective diffusion decreases with increasing tortuosity.[107] Angiogenic vascularity is also characterized by high-velocity arteriovenous shunts[108,109] that may cause the observed elevated flow velocities in malignant regions.
- The estimated velocity values are mostly in the sub-millimetre per second range; suggesting that flow in the capillaries is indeed measured.[111]

- Clinical evaluation using data recorded from 25 patients shows that the proposed method can be applied effectively to DCE-US, and that exploiting the Péclet number as a feature yields promising results (receiver-operating-characteristic curve area of 0.84) for prostate cancer localization.

Challenges and limitations

- The validity of the results presented in this work is hampered by the limitations of the quantitative validation procedure. First of all, histological assessment of Haematoxylin & Eosin stained prostate specimens is based on the level of cell-differentiation, whereas the developed methods aim at detecting angiogenesis. Hence, not all malignantly labelled time-intensity curves are necessarily probing angiogenic vasculature. In this regard, it would be interesting to validate the methods presented in this work with stains of the endothelial marker CD31, or the angiogenesis-stimulating vascular endothelial growth factor (VEGF). Moreover, several non-malignancies such as inflammation and benign prostatic hyperplasia also exhibit angiogenic activity.
- The registration procedure has some pitfalls. The ultrasound imaging planes are in general not parallel to the histology slices,[258] as specific pathological guidelines constrain the dissection procedure. Finally, the performance is biased towards large tumours and those that are consistent through multiple slices. This is a consequence of the infeasibility of drawing reliable regions-of-interest for small and scattered tumours, given the adopted registration procedure.
- While histopathology after radical prostatectomy enables detailed and pathologically-reliable assessment of the proposed method, it should be noted that the patient population is therefore biased; radical intervention is only performed on patients with biopsy-proven, significant prostate cancer.
- The DCE-US data used in this study is limited to 2D spatial information. Because of this, local channel estimation is affected by out of plane flows. In the worst case, the apparent causality between the measured output and input indicator dilution curves may not represent physical causality. This can occur for flow directions that are perpendicular to the imaging plane.

10.1b Estimation of blood flow heterogeneity (Chapter 3)

Blood flow in angiogenic vasculature is notoriously heterogeneous, governed by factors such as arteriovenous shunting, irregular branching, vessel tortuosity and increased flow resistance.[85,125] We therefore hypothesize that quantification of the heterogeneity of flow may provide an additional marker for localizing angiogenesis. To this end, statistics based on flow magnitude as well as its orientation can be exploited. In Chapter 3, we present a new DCE-US method that enables estimation of the blood flow velocity fields in the human prostate, and provide a statistical characterization of the heterogeneity in these fields through assessment of their local entropy.

Main observations and contributions

- Vector flow imaging based on local time-delay estimation allows assessment of macroscopic flow patterns in perfused tissue, effectively dealing with severe frame-to-frame speckle de-correlation,[259] typical for contrast-agent kinetics in the microvasculature.
- Qualitatively, the complexity of the flow patterns in cancerous areas was noticeable. Across 24 patients, the entropy of the flow fields was found significantly higher in malignant pixels as compared to benign pixels ($p \ll 0.01$). This result is in line with previous observations on the heterogeneous nature of blood flow in tumours,[85] and a recently proposed DCE-US perfusion clustering algorithm developed for the assessment of perfusion heterogeneity.[131]
- For pixel-based classification, the proposed parameters outperformed all other evaluated DCE-US features, yielding an ROC curve area of approximately 0.85.

Challenges and limitations

- The validation limitations of this work are similar to those of the work presented in Chapter 2. The use of H&E stained prostate specimens for validating a method that aims at detecting angiogenesis relies on the (not entirely valid) assumption that the degree of tumour cell-differentiation correlates with the presence of angiogenesis. This hypothesis is for instance violated in the presence of non-malignancies that exhibit angiogenic activity, such as inflammation.[260]
- A central assumption in this work is that dilution curves show a strong local similarity in shape. Violations of this assumption impact the time-delay estimation accuracy. In case of high local bolus dispersion or diffusion, a model-based transit time estimator that incorporates the dilution-curve shape alteration (e.g. the model used in Chapter 2) may be employed.
- In 2D, out of plane flows affect the velocity estimates and lead to an ambiguity between the elevational orientation and magnitude of the velocity vector.

10.1c Determining 3D blood flow trajectories (Chapter 4)

The proposed developments in the quantitative, macroscopic interpretation of clinical DCE-US videos showed their promise. Yet we also strived to develop a technique that provides explicit information on the underlying vascular architecture using these standard clinical protocols. In Chapter 4, we propose contrast-enhanced ultrasound tractography, which combines concepts from diffusion tensor tractography (DTT) MRI for fibre visualization[146] with DCE-US blood flow vector imaging, yielding 3D images of contrast agent trajectories. The method was applied *in-vivo*, using unique 4D CEUS recordings of the human prostate obtained in a clinical setting, with a clinically approved ultrasound system (LOGIC E9, GE Healthcare, Wauwatosa, WI, USA) and ultrasound contrast agent (SonoVue ®, Bracco, Milan, Italy).

Main observations and contributions

- We demonstrated that the techniques developed for DTT MRI can be adapted to enable characterization of the 3D microbubble flow vector fields obtained from DCE-US. The method can be applied effectively to standard DCE-US data that is acquired with a clinical ultrasound scanner in a clinical setting using approved contrast agents.
- In two out of three evaluated prostate-cancer cases, the spatial density of trajectories qualitatively showed a striking resemblance with the malignancies found by histopathology. Interestingly, the third case displayed widespread benign hyperplasia, also associated with the presence of angiogenesis.

Challenges and limitations

- This study aimed at providing a proof-of-principle, including a qualitative evaluation on three cancer cases. No quantitative assessment was performed. With merely three samples, statistical analysis of these results would add limited value and could be misleading. For this purpose, extensive validation based on a larger amount of patients should be pursued.
- Validation was performed through histological assessment of the Gleason score from H&E stained prostate specimens,[13] which is based on degree of cell-differentiation rather than explicit vascular characteristics.
- While the method's ability to reveal vascular networks was tested *in-silico*, no *in-vivo* proof could be given. As an intermediate step one could resort to *in-vitro* investigations of contrast-agents flowing through branching channels in a dedicated vascular phantom.[261]

10.1d Super-resolution ultrasound imaging of vasculature (Chapter 5)

In highly controlled laboratory settings, even more fine assessment of vascular networks can be achieved through super-resolution ultrasound microscopy.[154] The availability of such a technique in clinical practice would open up new possibilities for precise vascular characterization with the aim of localizing tumour-driven angiogenesis. In general, the fidelity and achieved resolution of the recovered image is dictated by the density of localized microbubbles and their localization accuracy, often achieved by imaging a fixed organ for long times with low bubble densities.[154] In a clinical scenario, investigation time is limited, and organ motion is generally inevitable. It is hence desirable to pin-point a substantial amount of microbubbles in as short time-span as possible. To this end, in Chapter 5, a new super-resolution ultrasound method that is designed specifically to deal with high-density clinically-acquired DCE-US data was introduced.

Main observations and contributions

- Microbubbles can be localized, even if their point-spread-functions show significant overlap.
- The proposed sparse recovery method effectively deals with high-density environments, enabling effective estimation of many microbubble locations in each frame, thereby reducing the required amount of frames.
- The amount of imaging frames used for recovery was predominantly limited by the increasingly impaired robustness of motion compensation after longer accumulation time.

Challenges and limitations

- Dealing with significant tissue motion remains a major challenge for super-resolution methods.[262] While in this work dedicated registration techniques were exploited to mitigate its impact, one can not account for out-of-plane movements which are in practice inevitable. This stresses the need for methods that can reach a high density of localized bubbles in a very short time in a clinical setting, and exploitation of 3D ultrasound acquisitions that facilitate complete registration in all directions.
- The localization performance should be thoroughly assessed through dedicated *in-silico* and *in-vitro* experiments where the ground truth vascular morphology is available. Alternatively, the proposed method could be compared against established high-resolution imaging techniques such as optical coherence tomography.[263]

10.1e Macroscopic versus microscopic assessment

Macroscopic and microscopic assessment of vascular characteristics both have their advantages and disadvantages. Microscopy effectively provides the means towards explicit characterization of cancer-related vascular features such as tortuosity and density. Yet, reliability and robustness in a clinical setting are currently lower than those of its macroscopic counterpart. For instance, subtle organ motion hardly impacts the macroscopic assessment of flow kinetics, but, when inadequately corrected for, can result in super-resolution images with invalid and distorted representations of vessels that are perceived as e.g. more tortuous.

10.1f Dynamic contrast-specific ultrasound tomography (Chapter 6)

Quantitative contrast-enhanced ultrasound technologies rely on methods that accurately detect and gauge contrast agents. Imaging methods often exploit the peculiar nonlinear response of microbubbles to ultrasound for this purpose, with the amplitude of the backscattered harmonic components being a typically adopted measure in commercial systems. Yet, being non-specific, these approaches suffer from nonlinear-propagation artifacts that impair the resulting quantification accuracy.[128,264] In this

context, we investigate the use of a contrast-agent-specific marker for DCE-US, a cumulative phase-shift between the second harmonic and fundamental components of the ultrasound wave. A proof-of-concept aimed at quantification of contrast agents in a tomographic fashion is presented in Chapter 6, displaying the potential of "Cumulative Phase Delay Imaging" (CPDI).

Main observations and contributions

- CPDI can be applied successfully to image and quantify ultrasound-contrast-agent kinetics in a tomographical setting.
- Quantification based on CPDI and harmonic imaging yields equivalent results, confirming the ability of CPDI to measure contrast-agent concentrations.
- Phase-delay values attained during the passage of ultrasound contrast agents were confirmed to be positive. This allows full separation between tissue and contrast agents, since these values are inherently negative in tissue.

Challenges and limitations

- In this proof-of-concept, the filtered back-projection algorithm was exploited to reconstruct CPDI from projection measurements. A primordial and unrealistic assumption in this approach is that the ultrasound rays travel in a straight path through multiple media, without refracting.[193] The method could hence benefit from existing and more advanced speed-of-sound reconstruction algorithms which have already been developed for volumetric breast ultrasound scanners;[199,201] the time-of-flight could simply be replaced with phase-delay variations.
- The method was tested *in-vitro* using a simplistic flow phantom. Hence, future work should include measurements with a dedicated breast ultrasound computed tomography scanner on heterogeneous and more complex targets.
- Ultrasound transmission tomography has inherent limitations with respect to imaging of small breasts and the breast lymph nodes that reside in the axillary area close to the chest and under the arm.

10.2 Tissue markers

The following tissue markers were developed and validated in a pre-clinical, *in-vitro* setting with open ultrasound platforms.

10.2a Viscoelastic behaviour (Chapter 7)

Tumours are stiffer than benign tissue, but also viscosity is a parameter of diagnostic value for detection and characterization of malignant lesions.[202] In Chapter 7, we

describe a new method that enables imaging not only stiffness, but also tissue viscosity from shear wave elastography by local model-based system identification.

Main observations and contributions

- The developed technique extends beyond the typical time-of-flight based methods by estimating the kinetic evolution between laterally sampled time-displacement curves instead of just their time-delay.
- By testing the method on simulated datasets and performing *in-vitro* experiments, we show the ability of the proposed technique to generate parametric maps of the viscoelastic material properties from shear wave measurements.
- The *in-silico* and *in-vitro* experiments show good agreement between the parameter estimates measured using the proposed method, and those obtained using the state-of-the art 2D Fourier transform method.[210]
- Compared to other methods that aim at assessing viscosity from shear wave measurements,[210,265] we like to stress that the proposed method is able to generate estimates in a pixel-based point-to-point fashion. This approach enables the generation of viscoelasticity maps with a lateral resolution that is primarily determined by the adopted spacing between these points.
- Although the results presented herein were obtained assuming a Voigt material model,[211] the approach can be readily generalized to facilitate characterization in terms of other viscoelastic material models, such as the typically adopted Maxwell or 3-parameter model.

Challenges and limitations

- To confirm the practical utility of the prosed method, it should be tested extensively on real tissue. Such tests can initially be conducted *ex-vivo*, but should eventually lead to *in-vivo* experiments. In these conditions, the impact of noise, diffraction and aberration, along with other disturbances, should be carefully investigated.[266]
- For tumour localization, a resolution in the order of millimetres is required.[226] As such, the lateral point-to-point distance across which the kinetics are estimated and the extent of spatial smoothing is limited, potentially increasing the impact of noise.

10.2b Degree of acoustic nonlinearity (Chapter 8)

A method that is able to characterize the nonlinear nature of ultrasound propagation would provide relevant information related to tissue fluid content,[74] a known cancer marker.[73] For this purpose, in Chapter 8, a new method is proposed that aims at quantifying this process through estimation of the coefficient of nonlinearity. The mathematical formulations and detailed numerical analysis described in this work aim

at providing a theoretical foundation for imaging this parameter, encouraging future research on practical implementations.

Main observations and contributions

- When comparing this work to other methods that aim at estimating the coefficient of nonlinearity,[76–78] we point out that the present method does not require a special transducer or setup, and provides a local estimation of the coefficient of nonlinearity based on the ratio of the second harmonic and fundamental components, thereby reducing spatial accumulation of errors due to unknown attenuation.
- The impact of inhomogeneous scatterer distributions on the estimates is addressed and contributions to the derivative term are limited to effects related to the wavelength dependency of scattering phenomena. Although speckle intensity variations are assumed similar for the fundamental and harmonic frequencies, there will be errors related to the fact that scattering for fundamental and harmonic frequencies is not equal.

Challenges and limitations

- Imaging the coefficient of nonlinearity in echo-mode is challenging. Estimates are impaired by incoherent and coherent summation of echoes originating from numerous sub-wavelength displaced scatterers, leading to a specific speckle pattern. While this issue was addressed by expressing the estimator in terms of the ratio of the second harmonic and fundamental envelopes and applying significant low-pass filtering, other (more dedicated) estimators that account for the speckle characteristics can be considered.
- Although the coefficient of nonlinearity was shown to be influenced by the water content of tissue, and we hence hypothesise that cancer exhibits distinct behaviour in this regard, no explicit characterization in cancer was performed. In particular, establishing profound knowledge on the relation between the coefficient of nonlinearity and various cancer phenotypes is important, but still lacking.

10.3 General Discussion

The diagnostic opportunities provided by ultrasound imaging have been growing steadily over the last few decades. Imaging modes such as (power) Doppler, contrast-enhancement and strain elastography are already adopted in the clinic, and newer techniques such as vector velocity imaging and shear wave elastography are finding their way into the latest high-end ultrasound devices.

This dissertation is mainly aimed at broadening the scope of ultrasound even further, providing access to more diagnostic information that characterizes cancer. Vascular features that are typical of malignant tumours can now be assessed through estimation of macroscopic characteristics such as microbubble dispersion, velocity, and irregularity of streams. At a smaller scale, we can determine streamline density by ultrasound tractography, and reveal truly microscopic features via super-resolution ultrasound. Complementary tissue features can be imaged through the proposed shear wave viscoelastography technology, and the exploitation of nonlinear acoustics for tissue characterization is also investigated and discussed. Despite these advancements, use of the full potential of ultrasound is still far away.

Although the ability to infer vascular and tissue characteristics from contrast-agent dispersion, blood flow velocity, vessel tortuosity, viscoelasticity, and acoustic nonlinearity would in theory aid cancer diagnosis and phenotyping, clinical implementation requires another step. For the clinician managing routine daily practice, the ever growing possibilities may actually become overwhelming and solutions diffused into scattered and competing elements. With the increasing complexity, it remains a challenge to attain wide-spread and optimal use of the proposed new technologies. With this in mind, great care should be taken to ensure effective translation of new technologies into the clinic, involving multiple iterations with clinical experts, well-designed clinical studies and promotion of the technology.

In a different domain, an important clinical breakthrough was recently made by the establishment of multi-parametric MRI (mpMRI), in which the rich but also complex toolset provided by MRI is exploited by devising diagnostic protocols that combine multiple MRI parameters. Considering this achievement, translation of such a strategy into the field of ultrasound by incorporating the full set of ultrasound tools into a clearly defined multi-parametric protocol (mpUS) seems sensible and necessary. Ultimately, this should provide an mpUS solution that suits the clinical workflow, is as operator-independent as possible, and enables not only the detection of lesions, but also their risk-assessment with an accurate score, similar to the BI-RADS or PI-RADS scores (Breast and Prostate Imaging Reporting and Data system, respectively).

Multi-parametric integration of the information extracted by the various ultrasound imaging modes could follow a scoring system that is similar to the aforementioned PI-RADS score. A multi-modal solution, in which multiple diagnostic modalities are combined may provide a further boost to the diagnostic performance, but adds complexity. Merging the work presented in this dissertation with recent trends in signal processing on artificial interpretation of the available data (machine learning) can elevate it to another level. Ultimately, technology should make routine diagnosis easier, clearer, and faster, while improving its accuracy and overall quality.

10.4 Conclusions

In this dissertation, new signal-processing methods for a variety of ultrasound imaging modalities are introduced. Building upon those characteristics that are typical for cancer, several limitations (listed in Chapter 1) of today's imaging in cancer are addressed through:

- Development of imaging solutions based on cost-effective and non-ionizing ultrasound to limit the diagnostic burden on the healthcare system and the patient.
- Considering both vascular and tissue characteristics as markers for cancer.
- Macroscopic assessment as well as microscopic imaging of the vascular net through dedicated signal processing methods for contrast-enhanced ultrasound.
- Introduction of a new high-resolution imaging method for estimation of tissue viscoelasticity (and hence detection of local viscoelastic remodelling accompanying cancer) based on ultrasound shear wave elastography.
- Establishment of the theoretical basis for a new method to image the extent of acoustic nonlinearity (related to fluid content) accumulated by distinct tissue types.

On their own, these contributions provide a step in the direction of accurate assessment of several specific cancer markers. Together they provide a broad spectrum of anatomical and functional information for ultrasound-based cancer imaging, while retaining the high cost-effectiveness that makes ultrasound so appealing.

10.5 Future Prospects

The heterogeneous nature of cancer and the wide range of tumour phenotypes makes it highly challenging (and perhaps, unlikely) to find a single feature to characterize them all. The chance of success is likely to increase when harvesting as much relevant information as possible. It is conceivable that exploiting a broad range of distinctive and orthogonal features will yield a better classification outcome when brought together.[69]

The new diagnostic options provided in this dissertation will allow clinicians to harvest a broader (and useful) spectrum of information, but the possibilities may be overwhelming. Therefore, incorporating the full set of ultrasound tools into a clearly defined multi-parametric protocol is of significant importance for clinical implementation of these techniques. Future work should therefore include the development of a multi-parametric solution that suits the clinical workflow, and enables not only the detection of malignancies, but also their grading. Along this line, machine learning techniques could be used to optimally combine features, e.g. through probabilistic frameworks such as Gaussian mixture models,[257] with the aim of inferring which condition or phenotype is likely to be present, and with which degree of certainty.

Bibliography

[1] American Cancer Society. Global cancer facts and figures 3rd edition. *American Cancer Society*, 2015.

[2] Shanthi Mendis et al. *Global status report on noncommunicable diseases 2010*. World Health Organization, 2014.

[3] Paul Hanly, Isabelle Soerjomataram, and Linda Sharp. Measuring the societal burden of cancer: The cost of lost productivity due to premature cancer-related mortality in europe. *International journal of cancer*, 136(4), 2015.

[4] Elena B Elkin and Peter B Bach. Cancer's next frontier: addressing high and increasing costs. *JAMA*, 303(11):1086–1087, 2010.

[5] Vincenzo Scattoni, Alexandre Zlotta, Rodolfo Montironi, Claude Schulman, Patrizio Rigatti, and Francesco Montorsi. Extended and saturation prostatic biopsy in the diagnosis and characterisation of prostate cancer: a critical analysis of the literature. *European urology*, 52(5):1309–1322, 2007.

[6] Andrew Vickers, Angel Cronin, Monique Roobol, Caroline Savage, Mari Peltola, Kim Pettersson, Peter T Scardino, Fritz Schröder, and Hans Lilja. Reducing unnecessary biopsy during prostate cancer screening using a four-kallikrein panel: an independent replication. *Journal of Clinical Oncology*, 28(15):2493–2498, 2010.

[7] D Di Gioia, P Stieber, GP Schmidt, D Nagel, V Heinemann, and A Baur-Melnyk. Early detection of metastatic disease in asymptomatic breast cancer patients with whole-body imaging and defined tumour marker increase. *British journal of cancer*, 112(5):809, 2015.

[8] Sukhwinder Kaur, Michael J Baine, Maneesh Jain, Aaron R Sasson, and Surinder K Batra. Early diagnosis of pancreatic cancer: challenges and new developments. *Biomarkers in medicine*, 6(5):597–612, 2012.

[9] Michael N Pollak and William D Foulkes. Opinion: Challenges to cancer control by screening. *Nature Reviews. Cancer*, 3(4):297, 2003.

[10] Andrew Wolf, Richard C Wender, Ruth B Etzioni, Ian M Thompson, Anthony V D'Amico, Robert J Volk, Durado D Brooks, Chiranjeev Dash, Idris Guessous, Kimberly Andrews, et al. American cancer society guideline for the early detection of prostate cancer: update 2010. *CA: a cancer journal for clinicians*, 60(2):70–98, 2010.

[11] Observer variation in recording clinical data from women presenting with breast lesions. report from the yorkshire breast cancer group. *BMJ*, 2(6096):1196–1199, 1977.

[12] Zhengshan Chen and Jiang Gu. Immunoglobulin g expression in carcinomas and cancer cell lines. *The FASEB Journal*, 21(11):2931–2938, 2007.

[13] Donald F Gleason. Histologic grading of prostate cancer: a perspective. *Human pathology*, 23(3):273–279, 1992.

[14] Nicolas Mottet, Joaquim Bellmunt, Michel Bolla, Erik Briers, Marcus G Cum-

berbatch, Maria De Santis, Nicola Fossati, Tobias Gross, Ann M Henry, Steven Joniau, et al. EAU-ESTRO-SIOG guidelines on prostate cancer. part 1: screening, diagnosis, and local treatment with curative intent. *European urology*, 71(4):618–629, 2017.

[15] KA Roehl, JV Antenor, and WJ Catalona. Serial biopsy results in prostate cancer screening study. *The Journal of urology*, 167(6):2435–2439, 2002.

[16] A Urruticoechea, R Alemany, J Balart, A Villanueva, F Vinals, and G Capella. Recent advances in cancer therapy: an overview. *Current pharmaceutical design*, 16(1):3–10, 2010.

[17] Michael L Blute, David G Bostwick, Erik J Bergstralh, Jeff M Slezak, Sandra K Martin, Christopher L Amling, and Horst Zincke. Anatomic site-specific positive margins in organconfined prostate cancer and its impact on outcome after radical prostatectomy. *Urology*, 50(5):733–739, 1997.

[18] Bo Lennernäs, Maliha Edgren, Michael Häggman, Bo J Norlén, and Sten Nilsson. Postoperative radiotherapy after prostatectomy a review. *Scandinavian journal of urology and nephrology*, 37(1):10–15, 2003.

[19] Bruce A Chabner and Thomas G Roberts Jr. Chemotherapy and the war on cancer. *Nature reviews. Cancer*, 5(1):65, 2005.

[20] Aurelio B Castrellon and Stefan Glück. Adjuvant therapy for her2 positive breast cancer: are anthracyclines still necessary. *Clin Adv Hematol Oncol*, 6:666–72, 2008.

[21] Naveen S Vasudev and Andrew R Reynolds. Anti-angiogenic therapy for cancer: current progress, unresolved questions and future directions. *Angiogenesis*, 17(3):471–494, 2014.

[22] Geoff Delaney, Susannah Jacob, Carolyn Featherstone, and Michael Barton. The role of radiotherapy in cancer treatment. *Cancer*, 104(6):1129–1137, 2005.

[23] Michel Bolla, Hein van Poppel, Laurence Collette, Paul van Cangh, Kris Vekemans, Luigi Da Pozzo, Theo M De Reijke, Antony Verbaeys, Jean-François Bosset, Roland Van Velthoven, et al. Postoperative radiotherapy after radical prostatectomy: a randomised controlled trial (eortc trial 22911). *The Lancet*, 366(9485):572–578, 2005.

[24] Phillip M Devlin. *Brachytherapy: applications and techniques*. Springer Publishing Company, 2015.

[25] Hashim Uddin Ahmed, Caroline Moore, and Mark Emberton. Minimally-invasive technologies in uro-oncology: the role of cryotherapy, hifu and photodynamic therapy in whole gland and focal therapy of localised prostate cancer. *Surgical oncology*, 18(3):219–232, 2009.

[26] Patrizia Agostinis, Kristian Berg, Keith A Cengel, Thomas H Foster, Albert W Girotti, Sandra O Gollnick, Stephen M Hahn, Michael R Hamblin, Asta Juzeniene, David Kessel, et al. Photodynamic therapy of cancer: an update. *CA: a cancer journal for clinicians*, 61(4):250–281, 2011.

[27] Barbara W Henderson, Sandra O Gollnick, John W Snyder, Theresa M Busch,

Philaretos C Kousis, Richard T Cheney, and Janet Morgan. Choice of oxygen-conserving treatment regimen determines the inflammatory response and outcome of photodynamic therapy of tumors. *Cancer research*, 64(6):2120–2126, 2004.

[28] Edward W Lee, Susan Thai, and Stephen T Kee. Irreversible electroporation: a novel image-guided cancer therapy. *Gut and liver*, 4(Suppl 1):S99, 2010.

[29] Craig S Levin. Primer on molecular imaging technology. *European journal of nuclear medicine and molecular imaging*, 32(2):S325–S345, 2005.

[30] Sanjiv Sam Gambhir. Molecular imaging of cancer with positron emission tomography. *Nature reviews. Cancer*, 2(9):683, 2002.

[31] Ali Afshar-Oromieh, Eleni Avtzi, Frederik L Giesel, Tim Holland-Letz, Heinz G Linhart, Matthias Eder, Michael Eisenhut, Silvan Boxler, Boris A Hadaschik, Clemens Kratochwil, et al. The diagnostic value of pet/ct imaging with the 68ga-labelled psma ligand hbed-cc in the diagnosis of recurrent prostate cancer. *European journal of nuclear medicine and molecular imaging*, 42(2):197–209, 2015.

[32] Hossein Jadvar. Prostate cancer: Pet with 18f-fdg, 18f-or 11c-acetate, and 18f-or 11c-choline. *Journal of Nuclear Medicine*, 52(1):81–89, 2011.

[33] Avinash C Kak and Malcolm Slaney. *Principles of computerized tomographic imaging*. SIAM, 2001.

[34] Karla Kerlikowske, Deborah Grady, Susan M Rubin, Christian Sandrock, and Virginia L Ernster. Efficacy of screening mammography: a meta-analysis. *Jama*, 273(2):149–154, 1995.

[35] L H Breimer. Ionizing radiation-induced mutagenesis. *British journal of cancer*, 57(1):6–18, 1988.

[36] Valerie P Jackson, R Edward Hendrick, Stephen A Feig, and Daniel B Kopans. Imaging of the radiographically dense breast. *Radiology*, 188(2):297–301, 1993.

[37] Justin E Costello, Nathan D Cecava, Jonathan E Tucker, and Jennifer L Bau. Ct radiation dose: current controversies and dose reduction strategies. *American Journal of Roentgenology*, 201(6):1283–1290, 2013.

[38] National Research Council et al. *Health risks from exposure to low levels of ionizing radiation: BEIR VII phase 2*, volume 7. National Academies Press, 2006.

[39] William R Hendee and Christopher J Morgan. Magnetic resonance imaging part i — physical principles. *Western Journal of Medicine*, 141(4):491, 1984.

[40] Leonard Marks, Shelena Young, and Shyam Natarajan. Mri–ultrasound fusion for guidance of targeted prostate biopsy. *Current opinion in urology*, 23(1):43, 2013.

[41] Brian M Dale, Mark A Brown, and Richard C Semelka. *MRI: basic principles and applications*. John Wiley & Sons, 2015.

[42] Anwar R Padhani, Guoying Liu, Dow Mu-Koh, Thomas L Chenevert, Harriet C Thoeny, Taro Takahara, Andrew Dzik-Jurasz, Brian D Ross, Marc Van Cauteren, David Collins, et al. Diffusion-weighted magnetic resonance imaging as a cancer

biomarker: consensus and recommendations. *Neoplasia*, 11(2):102–125, 2009.

[43] Milan Hajek and Monika Dezortova. Introduction to clinical in vivo mr spectroscopy. *European journal of radiology*, 67(2):185–193, 2008.

[44] Kristine Glunde and Zaver M Bhujwalla. Metabolic tumor imaging using magnetic resonance spectroscopy. In *Seminars in oncology*, volume 38, pages 26–41. Elsevier, 2011.

[45] AREND Heerschap, GERRIT J Jager, M Graaf, JELLE O Barentsz, JJMHC de la Rosette, GON Oosterhof, TEG Ruijter, and JHJ Ruijs. In vivo proton mr spectroscopy reveals altered metabolite content in malignant prostate tissue. 1997.

[46] Nicolas Barry Delongchamps, Arnaud Lefèvre, Naïm Bouazza, Frédéric Beuvon, Paul Legman, and François Cornud. Detection of significant prostate cancer with magnetic resonance targeted biopsies—should transrectal ultrasound-magnetic resonance imaging fusion guided biopsies alone be a standard of care? *The Journal of urology*, 193(4):1198–1204, 2015.

[47] Baris Turkbey and Peter L Choyke. Multiparametric mri and prostate cancer diagnosis and risk stratification. *Current opinion in urology*, 22(4):310–315, 2012.

[48] Dan Sperling. Multiparametric mri vs. histoscanning for prostate cancer detection, 2017.

[49] James PB O'connor, Alan Jackson, Geoff JM Parker, Caleb Roberts, and Gordon C Jayson. Dynamic contrast-enhanced mri in clinical trials of antivascular therapies. *Nature reviews Clinical oncology*, 9(3):167–177, 2012.

[50] Paul S Tofts, Gunnar Brix, David L Buckley, Jeffrey L Evelhoch, Elizabeth Henderson, Michael V Knopp, Henrik BW Larsson, Ting-Yim Lee, Nina A Mayr, Geoffrey JM Parker, et al. Estimating kinetic parameters from dynamic contrast-enhanced t 1-weighted mri of a diffusable tracer: standardized quantities and symbols. *Journal of magnetic resonance imaging*, 10(3):223–232, 1999.

[51] Caroline MA Hoeks, Jelle O Barentsz, Thomas Hambrock, Derya Yakar, Diederik M Somford, Stijn WTPJ Heijmink, Tom WJ Scheenen, Pieter C Vos, Henkjan Huisman, Inge M van Oort, et al. Prostate cancer: multiparametric mr imaging for detection, localization, and staging. *Radiology*, 261(1):46–66, 2011.

[52] Baris Turkbey, Haresh Mani, Vijay Shah, Ardeshir R Rastinehad, Marcelino Bernardo, Thomas Pohida, Yuxi Pang, Dagane Daar, Compton Benjamin, Yolanda L McKinney, et al. Multiparametric 3t prostate magnetic resonance imaging to detect cancer: histopathological correlation using prostatectomy specimens processed in customized magnetic resonance imaging based molds. *The Journal of urology*, 186(5):1818–1824, 2011.

[53] A Patricia Harper, Elizabeth Kelly-Fry, and J Stephen Noe. Ultrasound breast imaging—the method of choice for examining the young patient. *Ultrasound in medicine & biology*, 7(3):231235–233237, 1981.

[54] Jonathan M Rubin, Ronald O Bude, Paul L Carson, Robert L Bree, and Ronald S Adler. Power doppler us: a potentially useful alternative to mean frequency-based color doppler us. *Radiology*, 190(3):853–856, 1994.

[55] Wei Tse Yang, Jenny Chang, and Constantine Metreweli. Patients with breast cancer: differences in color doppler flow and gray-scale us features of benign and malignant axillary lymph nodes. *Radiology*, 215(2):568–573, 2000.

[56] A Evans, P Whelehan, K Thomson, K Brauer, L Jordan, C Purdie, D McLean, L Baker, S Vinnicombe, and A Thompson. Differentiating benign from malignant solid breast masses: value of shear wave elastography according to lesion stiffness combined with greyscale ultrasound according to bi-rads classification. *British journal of cancer*, 107(2):224, 2012.

[57] Barry B Goldberg, Ji-Bin Liu, and Flemming Forsberg. Ultrasound contrast agents: a review. *Ultrasound in Medicine & Biology*, 20(4):319–333, 1994.

[58] J Folkman. Role of angiogenesis in tumor growth and metastasis. In *Seminars in oncology*, volume 29, pages 15–18. Elsevier, 2002.

[59] Michael K Brawer. Quantitative microvessel density: a staging and prognostic marker for human prostatic carcinoma. *Cancer*, 78(2):345–349, 1996.

[60] Noel Weidner, PR Carroll, J Flax, W Blumenfeld, and J Folkman. Tumor angiogenesis correlates with metastasis in invasive prostate carcinoma. *The American journal of pathology*, 143(2):401, 1993.

[61] Douglas Hanahan and Robert A Weinberg. The hallmarks of cancer. *cell*, 100(1):57–70, 2000.

[62] Ethan J Halpern. Contrast-enhanced ultrasound imaging of prostate cancer. *Reviews in Urology*, 8:S29, 2006.

[63] Bjoern Grabski, Leif Baeurle, Annemie Loch, Bjoern Wefer, Udo Paul, and Tillmann Loch. Computerized transrectal ultrasound of the prostate in a multicenter setup (C-TRUS-MS): detection of cancer after multiple negative systematic random and in primary biopsies. *World journal of urology*, 29(5):573–579, 2011.

[64] Johan Braeckman, Philippe Autier, Christian Garbar, Miriam Pipeleers Marichal, Cristina Soviany, Rina Nir, Dror Nir, Dirk Michielsen, Harry Bleiberg, Lars Egevad, et al. Computer-aided ultrasonography (histoscanning): a novel technology for locating and characterizing prostate cancer. *BJU international*, 101(3):293–298, 2008.

[65] Wen-Jie Wu and Woo Kyung Moon. Ultrasound breast tumor image computer-aided diagnosis with texture and morphological features. *Academic radiology*, 15(7):873–880, 2008.

[66] Moritz Franz Hamann, C Hamann, A Trettel, KP Jünemann, and CM Naumann. Computer-aided transrectal ultrasound: does prostate HistoScanning™ improve detection performance of prostate cancer in repeat biopsies? *BMC urology*, 15(1):76, 2015.

[67] Giovanna Russo, Massimo Mischi, Wout Scheepens, Jean J De la Rosette, and Hessel Wijkstra. Angiogenesis in prostate cancer: onset, progression and imaging. *BJU international*, 110(11c), 2012.

[68] Saradwata Sarkar and Sudipta Das. A review of imaging methods for prostate cancer detection. *Biomedical engineering and computational biology*, 7(Suppl 1):1,

2016.

[69] Arnoud Postema, Massimo Mischi, Jean de la Rosette, and Hessel Wijkstra. Multiparametric ultrasound in the detection of prostate cancer: a systematic review. *World journal of urology*, 33(11):1651–1659, 2015.

[70] Yanmi Li, Jie Tang, Xiang Fei, and Yi Gao. Diagnostic performance of contrast enhanced ultrasound in patients with prostate cancer: a meta-analysis. *Academic radiology*, 20(2):156–164, 2013.

[71] M P J Kuenen, M Mischi, and H Wijkstra. Contrast-ultrasound diffusion imaging for localization of prostate cancer. *IEEE Transactions on Medical Imaging*, 30(8):1493–1502, 2011.

[72] MPJ Kuenen, TA Saidov, H Wijkstra, JJMCH de La Rosette, and M Mischi. Spatiotemporal correlation of ultrasound contrast agent dilution curves for angiogenesis localization by dispersion imaging. *IEEE Transactions on Ultrasonics, Ferroelectrics, and Frequency Control*, 60(12):2665–2669, 2013.

[73] Jennifer M Munson and Adrian C Shieh. Interstitial fluid flow in cancer: implications for disease progression and treatment. *Cancer management and research*, 6:317, 2014.

[74] Y Yang and F Dunn. Acoustic non-linearity method for estimating the ratio of bound to free water of biological media. *Ultrasonics*, 31(1):35–38, 1993.

[75] CM Sehgal, GM Brown, RC Bahn, and James F Greenleaf. Measurement and use of acoustic nonlinearity and sound speed to estimate composition of excised livers. *Ultrasound in medicine & biology*, 12(11):865–874, 1986.

[76] Francois Varray, Olivier Basset, Piero Tortoli, and et al. Extensions of nonlinear b/a parameter imaging methods for echo mode. *Ultrasonics, Ferroelectrics and Frequency Control, IEEE Transactions on*, 58(6):1232–1244, 2011.

[77] S Ueno, M Hashimoto, H Fukukita, and et al. Ultrasound thermometry in hyperthermia. In *Ultrasonics Symposium, 1990. Proceedings., IEEE 1990*, pages 1645–1652. IEEE, 1990.

[78] Gong Xiu-fen, Feng Ruo, Zhu Cheng-ya, and et al. Ultrasonic investigation of the nonlinearity parameter b/a in biological media. *The Journal of the Acoustical Society of America*, 76(3):949–950, 1984.

[79] American Cancer Society. *Cancer Facts & Figures 2015*. American Cancer Society, Atlanta, 2015.

[80] S Loeb, A Vellekoop, HU Ahmed, J Catto, M Emberton, R Nam, DJ Rosario, V Scattoni, and Y Lotan. Systematic review of complications of prostate biopsy. *European urology*, 64(6):876–892, 2013.

[81] Dwayne TS Chang, Benjamin Challacombe, and Nathan Lawrentschuk. Transperineal biopsy of the prostate - is this the future? *Nature Reviews Urology*, 10(12):690–702, 2013.

[82] GJ Lueck, TK Kim, PN Burns, and AL Martel. Hepatic perfusion imaging using factor analysis of contrast enhanced ultrasound. *IEEE Transactions on Medical Imaging*, 27(10):1449–1457, 2008.

[83] D Cosgrove and N Lassau. Imaging of perfusion using ultrasound. *European journal of nuclear medicine and molecular imaging*, 37(1):65–85, 2010.

[84] K Wei, E Le, J Bin, M Coggins, J Thorpe, and S Kaul. Quantification of renal blood flow with contrast-enhanced ultrasound. *Journal of the American College of Cardiology*, 37(4):1135–1140, 2001.

[85] Robert J Gillies, Paul A Schomack, Timothy W Secomb, and Natarajan Raghunand. Causes and effects of heterogeneous perfusion in tumors. *Neoplasia*, 1(3):197–207, 1999.

[86] M Cao, Y Liang, C Shen, KD Miller, and KM Stantz. Developing dce-ct to quantify intra-tumor heterogeneity in breast tumors with differing angiogenic phenotype. *IEEE Transactions on Medical Imaging*, 28(6):861–871, 2009.

[87] TS Koh, XY Wu, LH Cheong, and CCT Lim. Assessment of perfusion by dynamic contrast-enhanced imaging using a deconvolution approach based on regression and singular value decomposition. *IEEE Transactions on Medical Imaging*, 23(12):1532–1542, 2004.

[88] MPJ Kuenen, TA Saidov, H Wijkstra, and M Mischi. Contrast-ultrasound dispersion imaging for prostate cancer localization by improved spatiotemporal similarity analysis. *Ultrasound in medicine & biology*, 39(9):1631–1641, 2013.

[89] LL Scharf. *Statistical signal processing*, volume 98. Addison-Wesley Reading, MA, 1991.

[90] RF Wagner, SW Smith, JM Sandrik, and H Lopez. Statistics of speckle in ultrasound b-scans. *IEEE Transactions on Sonics and Ultrasonics*, 30(3):156–163, 1983.

[91] M Wax and T Kailath. Detection of signals by information theoretic criteria. *IEEE Transactions on Acoustics, Speech and Signal Processing*, 33(2):387–392, 1985.

[92] S Whitaker. Diffusion and dispersion in porous media. *AIChE Journal*, 13(3):420–427, 1967.

[93] W Perl and FP Chinard. A convection-diffusion model of indicator transport through an organ. *Circulation research*, 22(2):273–298, 1968.

[94] G Taylor. Dispersion of soluble matter in solvent flowing slowly through a tube. In *Proceedings of the Royal Society of London A: Mathematical, Physical and Engineering Sciences*, volume 219, pages 186–203. The Royal Society, 1953.

[95] DG Duffy. *Green's functions with applications*. CRC Press, 2001.

[96] M Mischi. *Contrast Echocardiography for Cardiac Quantifications*. PhD thesis, Jan. 2004.

[97] LG Leal. *Advanced transport phenomena: fluid mechanics and convective transport processes*. Cambridge University Press, 2007.

[98] MPJ Kuenen, IHF Herold, HHM Korsten, JJMCH de la Rosette, H Wijkstra, and M Mischi. Maximum-likelihood estimation for indicator dilution analysis. *IEEE Transactions on Biomedical Engineering*, 61(3):821–831, 2014.

[99] RD Yates and DJ Goodman. Probability and stochastic processes. *John Willey &*

Sons, 2005.

[100] S Zacks. *The theory of statistical inference*, volume 34. Wiley New York, 1971.

[101] WF Hamilton, JW Moore, JM Kinsman, and RG Spurling. Simultaneous determination of the pulmonary and systemic circulation times in man and of a figure related to the cardiac output. *American Journal of Physiology–Legacy Content*, 84(2):338–344, 1928.

[102] GN Stewart. Researches on the circulation time and on the influences which affect it. *The Journal of physiology*, 22(3):159–183, 1897.

[103] Steven B Feinstein. The powerful microbubble: from bench to bedside, from intravascular indicator to therapeutic delivery system, and beyond. *American Journal of physiology-heart and circulatory physiology*, 287(2):H450–H457, 2004.

[104] Nico de Jong, Peter JA Frinking, Ayache Bouakaz, and Folkert J Ten Cate. Detection procedures of ultrasound contrast agents. *Ultrasonics*, 38(1):87–92, 2000.

[105] R Montironi, T van der Kwast, L Boccon-Gibod, AV Bono, and L Boccon-Gibod. Handling and pathology reporting of radical prostatectomy specimens. *European urology*, 44(6):626–636, 2003.

[106] JA Hanley and BJ McNeil. The meaning and use of the area under a receiver operating characteristic (roc) curve. *Radiology*, 143(1):29–36, 1982.

[107] M Sahimi. *Flow and transport in porous media and fractured rock: from classical methods to modern approaches*. John Wiley & Sons, 2011.

[108] C Sohn, J Blohmer, and U Hamper. *Breast ultrasound: a systematic approach to technique and image interpretation*. Thieme, 1999.

[109] KJ Taylor, I Ramos, D Carter, SS Morse, D Snower, and K Fortune. Correlation of doppler us tumor signals with neovascular morphologic features. *Radiology*, 166(1):57–62, 1988.

[110] A Bollinger, P Butti, J-P Barras, H Trachsler, and W Siegenthaler. Red blood cell velocity in nailfold capillaries of man measured by a television microscopy technique. *Microvascular research*, 7(1):61–72, 1974.

[111] M Stücker, V Baier, T Reuther, K Hoffmann, K Kellam, and P Altmeyer. Capillary blood cell velocity in human skin capillaries located perpendicularly to the skin surface: measured by a new laser doppler anemometer. *Microvascular research*, 52(2):188–192, 1996.

[112] David M Brizel, Bruce Klitzman, J Michael Cook, Jeri Edwards, Gary Rosner, and Mark W Dewhirst. A comparison of tumor and normal tissue microvascular hematocrits and red cell fluxes in a rat window chamber model. *International Journal of Radiation Oncology*Biology*Physics*, 25(2):269–276, 1993.

[113] Mark W Dewhirst, CY Tso, Regina Oliver, Cindy S Gustafson, Timothy W Secomb, and Joseph F Gross. Morphologic and hemodynamic comparison of tumor and healing normal tissue microvasculature. *International Journal of Radiation Oncology*Biology*Physics*, 17(1):91–99, 1989.

[114] Rakesh K Jain, Nina Safabakhsh, Axel Sckell, Yi Chen, Ping Jiang, Laura Ben-

jamin, Fan Yuan, and Eli Keshet. Endothelial cell death, angiogenesis, and microvascular function after castration in an androgen-dependent tumor: role of vascular endothelial growth factor. *Proceedings of the National Academy of Sciences*, 95(18):10820–10825, 1998.

[115] CM Bishop et al. *Pattern recognition and machine learning*, volume 4. springer New York, 2006.

[116] G Renaud, JG Bosch, GL Ten Kate, V Shamdasani, R Entrekin, Nico de Jong, and AFW Van der Steen. Counter-propagating wave interaction for contrast-enhanced ultrasound imaging. *Physics in medicine and biology*, 57(21):L9, 2012.

[117] Stefan G Schalk, Arnoud Postema, Tamerlan A Saidov, Libertario Demi, Martijn Smeenge, Jean JMCH de la Rosette, Hessel Wijkstra, and Massimo Mischi. 3d surface-based registration of ultrasound and histology in prostate cancer imaging. *Computerized Medical Imaging and Graphics*, 47:29–39, 2016.

[118] U H Stenman, Jari Leinonen, Wan-Ming Zhang, and Patrik Finne. Prostate-specific antigen. In *Seminars in cancer biology*, volume 9, pages 83–93. Elsevier, 1999.

[119] N Mottet, J Bellmunt, E Briers, M Bolla, P Cornford, M De Santis, A Henry, S Joniau, T Lam, M D Mason, V Matveev, H van der Poel, T H van der Kwast, O Rouvière, and T Wiegel. Eau guidelines on prostate cancer. 2016.

[120] Massimo Mischi, Simona Turco, Cristina Lavini, Kyveli Kompatsiari, Jean JMCH de la Rosette, Marcel Breeuwer, and Hessel Wijkstra. Magnetic resonance dispersion imaging for localization of angiogenesis and cancer growth. *Investigative radiology*, 49(8):561–569, 2014.

[121] SG Schalk, L Demi, M Smeenge, DM Mills, KD Wallace, JJMCH de la Rosette, H Wijkstra, and M Mischi. 4-D spatiotemporal analysis of ultrasound contrast agent dispersion for prostate cancer localization: a feasibility study. *IEEE Transactions on Ultrasonics, Ferroelectrics, and Frequency Control*, 62(5):839–851, 2015.

[122] James E Thompson, Daniel Moses, Ron Shnier, Phillip Brenner, Warick Delprado, Lee Ponsky, Marley Pulbrook, Maret Böhm, Anne-Maree Haynes, Andrew Hayen, et al. Multiparametric magnetic resonance imaging guided diagnostic biopsy detects significant prostate cancer and could reduce unnecessary biopsies and over detection: a prospective study. *The Journal of urology*, 192(1):67–74, 2014.

[123] Srinivas Vourganti, Ardeshir Rastinehad, Nitin K Yerram, Jeffrey Nix, Dmitry Volkin, An Hoang, Baris Turkbey, Gopal N Gupta, Jochen Kruecker, W Marston Linehan, et al. Multiparametric magnetic resonance imaging and ultrasound fusion biopsy detect prostate cancer in patients with prior negative transrectal ultrasound biopsies. *The Journal of urology*, 188(6):2152–2157, 2012.

[124] Joan Chang and Janine Erler. Hypoxia-mediated metastasis. In *Tumor Microenvironment and Cellular Stress*, pages 55–81. Springer, 2014.

[125] D Cosgrove. Angiogenesis imaging–ultrasound. *The British journal of radiology*, 2014.

[126] Thomas P Gauthier, Michalakis A Averkiou, and Edward LS Leen. Perfusion

quantification using dynamic contrast-enhanced ultrasound: The impact of dynamic range and gain on time–intensity curves. *Ultrasonics*, 51(1):102–106, 2011.

[127] Thomas P Gauthier, Mohamed Chebil, Pierre Peronneau, and Nathalie Lassau. In vitro evaluation of the impact of ultrasound scanner settings and contrast bolus volume on time–intensity curves. *Ultrasonics*, 52(1):12–19, 2012.

[128] M-X Tang, H Mulvana, T Gauthier, AKP Lim, DO Cosgrove, RJ Eckersley, and E Stride. Quantitative contrast-enhanced ultrasound imaging: a review of sources of variability. *Interface Focus*, 1(4):520–539, 2011.

[129] Alan Jackson, James PB O'Connor, Geoff JM Parker, and Gordon C Jayson. Imaging tumor vascular heterogeneity and angiogenesis using dynamic contrast-enhanced magnetic resonance imaging. *Clinical Cancer Research*, 13(12):3449–3459, 2007.

[130] Peter Frinking, Laurent Mercier, Nicolas Rognin, Marcel Arditi, François Tranquart, and Michel Schneider. Real-time contrast-enhanced ultrasound parametric imaging in prostate. In *Proceedings of the 15th european symposium on ultrasound contrast imaging*, pages 40–49, 2010.

[131] Guillaume Barrois, Alain Coron, and S Lori Bridal. Detection of early therapeutic response with dynamic contrast enhanced ultrasound using a perfusion clustering algorithm. In *2014 IEEE International Ultrasonics Symposium*, pages 1754–1757. IEEE, 2014.

[132] PG Saffman. A theory of dispersion in a porous medium. *Journal of Fluid Mechanics*, 6(03):321–349, 1959.

[133] John M Hudson, Raffi Karshafian, and Peter N Burns. Quantification of flow using ultrasound and microbubbles: a disruption replenishment model based on physical principles. *Ultrasound in medicine & biology*, 35(12):2007–2020, 2009.

[134] Martin Krix, Fabian Kiessling, Nabeel Farhan, Kerstin Schmidt, Johannes Hoffend, and Stefan Delorme. A multivessel model describing replenishment kinetics of ultrasound contrast agent for quantification of tissue perfusion. *Ultrasound in medicine & biology*, 29(10):1421–1430, 2003.

[135] Mark O Hill. Diversity and evenness: a unifying notation and its consequences. *Ecology*, 54(2):427–432, 1973.

[136] Claude Elwood Shannon. A mathematical theory of communication. *ACM SIGMOBILE Mobile Computing and Communications Review*, 5(1):3–55, 2001.

[137] Roger Bourne. *Fundamentals of digital imaging in medicine*. Springer Science & Business Media, 2010.

[138] Guillaume Barrois, Alain Coron, Thomas Payen, Alexandre Dizeux, and Lori Bridal. A multiplicative model for improving microvascular flow estimation in dynamic contrast-enhanced ultrasound (dce-us): theory and experimental validation. *IEEE transactions on ultrasonics, ferroelectrics, and frequency control*, 60(11):2284–2294, 2013.

[139] Asoke K Nandi. On the subsample time delay estimation of narrowband ultra-

sonic echoes. *IEEE Transactions on Ultrasonics, Ferroelectrics, and Frequency Control*, 42(6):993–1001, 1995.

[140] Costas Strouthos, Marios Lampaskis, Vassilis Sboros, Alan McNeilly, and Michalakis Averkiou. Indicator dilution models for the quantification of microvascular blood flow with bolus administration of ultrasound contrast agents. *IEEE Transactions on Ultrasonics, Ferroelectrics, and Frequency Control*, 57(6):1296–1310, 2010.

[141] William H Kruskal and W Allen Wallis. Use of ranks in one-criterion variance analysis. *Journal of the American statistical Association*, 47(260):583–621, 1952.

[142] Zdravko I Botev, Joseph F Grotowski, Dirk P Kroese, et al. Kernel density estimation via diffusion. *The Annals of Statistics*, 38(5):2916–2957, 2010.

[143] Ruud JG van Sloun, Libertario Demi, Arnoud W Postema, Jean JMCH de la Rosette, Hessel Wijkstra, and Massimo Mischi. Ultrasound-contrast-agent dispersion and velocity imaging for prostate cancer localization. *Medical Image Analysis*, 35:610–619, 2017.

[144] Michael Leunig, Fan Yuan, Michael D Menger, Yves Boucher, Alwin E Goetz, Konrad Messmer, and Rakesh K Jain. Angiogenesis, microvascular architecture, microhemodynamics, and interstitial fluid pressure during early growth of human adenocarcinoma ls174t in scid mice. *Cancer Research*, 52(23):6553–6560, 1992.

[145] T E J Behrens, H Johansen-Berg, M W Woolrich, S M Smith, C A M Wheeler-Kingshott, P A Boulby, G J Barker, E L Sillery, K Sheehan, O Ciccarelli, et al. Non-invasive mapping of connections between human thalamus and cortex using diffusion imaging. *Nature Neuroscience*, 6(7):750–757, 2003.

[146] P Mukherjee, JI Berman, SW Chung, CP Hess, and RG Henry. Diffusion tensor mr imaging and fiber tractography: theoretic underpinnings. *American Journal of Neuroradiology*, 29(4):632–641, 2008.

[147] A Kunimatsu, S Aoki, Y Masutani, O Abe, H Mori, and K Ohtomo. Three-dimensional white matter tractography by diffusion tensor imaging in ischaemic stroke involving the corticospinal tract. *Neuroradiology*, 45(8):532–535, 2003.

[148] Laura M Rowland, Elena A Spieker, Alan Francis, Peter B Barker, William T Carpenter, and Robert W Buchanan. White matter alterations in deficit schizophrenia. *Neuropsychopharmacology*, 34(6):1514–1522, 2009.

[149] Jonathan R Lindner. Microbubbles in medical imaging: current applications and future directions. *Nature Reviews Drug Discovery*, 3(6):527–533, 2004.

[150] R J G van Sloun, Libertario Demi, Arnoud Postema, Jean de la Rosette, Hessel Wijkstra, and Massimo Mischi. Entropy of ultrasound-contrast-agent velocity fields for angiogenesis imaging in prostate cancer. *IEEE Transactions on Medical Imaging*, 36(3):826–837, 2016.

[151] Sarah E Shelton, Yueh Z Lee, Mike Lee, Emmanuel Cherin, F Stuart Foster, Stephen R Aylward, and Paul A Dayton. Quantification of microvascular tortuosity during tumor evolution using acoustic angiography. *Ultrasound in Medicine & Biology*, 41(7):1896–1904, 2015.

[152] Denis Le Bihan. Looking into the functional architecture of the brain with diffusion mri. *Nature Reviews Neuroscience*, 4(6):469–480, 2003.

[153] Ruud J G van Sloun, Libertario Demi, Arnoud W Postema, Jean J M C H de la Rosette, Hessel Wijkstra, and Massimo Mischi. Ultrasound-contrast-agent dispersion and velocity imaging for prostate cancer localization. *Medical Image Analysis*, 35:610–619, 2017.

[154] Claudia Errico, Juliette Pierre, Sophie Pezet, Yann Desailly, Zsolt Lenkei, Olivier Couture, and Mickael Tanter. Ultrafast ultrasound localization microscopy for deep super-resolution vascular imaging. *Nature*, 527(7579):499–502, 2015.

[155] Yann Desailly, Juliette Pierre, Olivier Couture, and Mickael Tanter. Resolution limits of ultrafast ultrasound localization microscopy. *Physics in Medicine and Biology*, 60(22):8723, 2015.

[156] Olivier Couture. Super-resolution imaging with ultrafast ultrasound localization microscopy (uulm). In *Proceedings of European Symposium on Ultrasound Contrast Imaging*, Rotterdam, The Netherlands, January 19-20, 2017.

[157] Ryan C Gessner, Stephen R Aylward, and Paul A Dayton. Mapping microvasculature with acoustic angiography yields quantifiable differences between healthy and tumor-bearing tissue volumes in a rodent model. *Radiology*, 264(3):733–740, 2012.

[158] Hang Gao, Piet Claus, Mihaela-Silvia Amzulescu, Ivan Stankovic, Jan D'hooge, and Jens-Uwe Voigt. How to optimize intracardiac blood flow tracking by echocardiographic particle image velocimetry? exploring the influence of data acquisition using computer-generated data sets. *European Heart Journal-Cardiovascular Imaging*, pages 490–499, 2011.

[159] Luke Bloy and Ragini Verma. On computing the underlying fiber directions from the diffusion orientation distribution function. *Medical Image Computing and Computer-Assisted Intervention–MICCAI 2008*, pages 1–8, 2008.

[160] J Markel. FFT pruning. *IEEE Transactions on Audio and Electroacoustics*, 19(4):305–311, 1971.

[161] Peter J Basser, Sinisa Pajevic, Carlo Pierpaoli, Jeffrey Duda, and Akram Aldroubi. In vivo fiber tractography using dt-mri data. *Magnetic Resonance in Medicine*, 44(4):625–632, 2000.

[162] Zhaohua Ding, John C Gore, and Adam W Anderson. Reduction of noise in diffusion tensor images using anisotropic smoothing. *Magnetic Resonance in Medicine*, 53(2):485–490, 2005.

[163] Damien Rohmer, Arkadiusz Sitek, and Grant T Gullberg. Reconstruction and visualization of fiber and laminar structure in the normal human heart from ex vivo diffusion tensor magnetic resonance imaging (dtmri) data. *Investigative Radiology*, 42(11):777–789, 2007.

[164] Elizabeth Bullitt, Donglin Zeng, Guido Gerig, Stephen Aylward, Sarang Joshi, J Keith Smith, Weili Lin, and Matthew G Ewend. Vessel tortuosity and brain tumor malignancy: a blinded study. *Academic Radiology*, 12(10):1232–1240, 2005.

[165] Jonathan I Epstein, Lars Egevad, Mahul B Amin, Brett Delahunt, John R Srigley, Peter A Humphrey, Grading Committee, et al. The 2014 international society of urological pathology (ISUP) consensus conference on gleason grading of prostatic carcinoma: definition of grading patterns and proposal for a new grading system. *The American journal of surgical pathology*, 40(2):244–252, 2016.

[166] S J Shih, M A Dall'Era, J R Westphal, J Yang, C G J Sweep, R Gandour-Edwards, and Christopher P Evans. Elements regulating angiogenesis and correlative microvessel density in benign hyperplastic and malignant prostate tissue. *Prostate Cancer and Prostatic Diseases*, 6(2):131–137, 2003.

[167] M E Deering, S A Bigler, M Brown, and M K Brawer. Microvascularity in benign prostatic hyperplasia. *The Prostate*, 26:111––115, 1995.

[168] Eric Betzig, George H Patterson, Rachid Sougrat, O Wolf Lindwasser, Scott Olenych, Juan S Bonifacino, Michael W Davidson, Jennifer Lippincott-Schwartz, and Harald F Hess. Imaging intracellular fluorescent proteins at nanometer resolution. *Science*, 313(5793):1642–1645, 2006.

[169] Yann Desailly, Olivier Couture, Mathias Fink, and Mickael Tanter. Sono-activated ultrasound localization microscopy. *Applied Physics Letters*, 103(17):174107, 2013.

[170] Michael J Rust, Mark Bates, and Xiaowei Zhuang. Sub-diffraction-limit imaging by stochastic optical reconstruction microscopy (storm). *Nature methods*, 3(10):793–796, 2006.

[171] Thomas Dertinger, Ryan Colyer, Gopal Iyer, Shimon Weiss, and Jörg Enderlein. Fast, background-free, 3d super-resolution optical fluctuation imaging (sofi). *Proceedings of the National Academy of Sciences*, 106(52):22287–22292, 2009.

[172] Avinoam Bar-Zion, Charles Tremblay-Darveau, Oren Solomon, Dan Adam, and Yonina C Eldar. Fast vascular ultrasound imaging with enhanced spatial resolution and background rejection. *IEEE transactions on medical imaging*, 36(1):169–180, 2017.

[173] Avinoam Bar-Zion, Oren Solomon, Charles Tremblay-Darveau, Dan Adam, and Yonina C Eldar. Sparsity-based ultrasound super-resolution imaging. In *Proceedings of the 23rd European symposium on Ultrasound Contrast Imaging*, pages 156–157. ICUS, 2017.

[174] Yonina C Eldar and Gitta Kutyniok. *Compressed sensing: theory and applications*. Cambridge University Press, 2012.

[175] Amir Beck and Marc Teboulle. A fast iterative shrinkage-thresholding algorithm for linear inverse problems. *SIAM journal on imaging sciences*, 2(1):183–202, 2009.

[176] Charlie Demené, Thomas Deffieux, Mathieu Pernot, Bruno-Félix Osmanski, Valérie Biran, Jean-Luc Gennisson, Lim-Anna Sieu, Antoine Bergel, Stéphanie Franqui, Jean-Michel Correas, et al. Spatiotemporal clutter filtering of ultrafast ultrasound data highly increases doppler and fultrasound sensitivity. *IEEE transactions on medical imaging*, 34(11):2271–2285, 2015.

[177] Bryan P Schneider and Kathy D Miller. Angiogenesis of breast cancer. *Journal of Clinical Oncology*, 23(8):1782–1790, 2005.

[178] Kirsten Christensen-Jeffries, Richard J Browning, Meng-Xing Tang, Christopher Dunsby, and Robert J Eckersley. In vivo acoustic super-resolution and super-resolved velocity mapping using microbubbles. *IEEE transactions on medical imaging*, 34(2):433–440, 2015.

[179] Brooks D Lindsey, Juan D Rojas, K Heath Martin, Sarah E Shelton, and Paul A Dayton. Acoustic characterization of contrast-to-tissue ratio and axial resolution for dual-frequency contrast-specific acoustic angiography imaging. *IEEE transactions on ultrasonics, ferroelectrics, and frequency control*, 61(10):1668–1687, 2014.

[180] Fabrizio Calliada, Rodolfo Campani, Olivia Bottinelli, Anna Bozzini, and Maria Grazia Sommaruga. Ultrasound contrast agents: basic principles. *European journal of radiology*, 27:S157–S160, 1998.

[181] Peter JA Frinking, Ayache Bouakaz, Johan Kirkhorn, Folkert J Ten Cate, and Nico De Jong. Ultrasound contrast imaging: current and new potential methods. *Ultrasound in medicine & biology*, 26(6):965–975, 2000.

[182] Cecile Huang-Wei, Aurore Bleuzen, Pascal Bourlier, Jérome Roumy, Ayache Bouakaz, Léandre Pourcelot, and François Tranquart. Differential diagnosis of focal nodular hyperplasia with quantitative parametric analysis in contrast-enhanced sonography. *Investigative radiology*, 41(3):363–368, 2006.

[183] P Ricci, V Cantisani, L Ballesio, E Pagliara, E Sallusti, FM Drudi, F Trippa, F Calascibetta, SM Erturk, M Modesti, et al. Benign and malignant breast lesions: efficacy of real time contrast-enhanced ultrasound vs. magnetic resonance imaging. *Ultraschall in der Medizin-European Journal of Ultrasound*, 28(01):57–62, 2007.

[184] Jing Du, Lin Wang, Cai-Feng Wan, Jia Hua, Hua Fang, Jie Chen, and Feng-Hua Li. Differentiating benign from malignant solid breast lesions: combined utility of conventional ultrasound and contrast-enhanced ultrasound in comparison with magnetic resonance imaging. *European journal of radiology*, 81(12):3890–3899, 2012.

[185] Marianne Gauthier, Farid Tabarout, Ingrid Leguerney, Mélanie Polrot, Stéphanie Pitre, Pierre Peronneau, and Nathalie Lassau. Assessment of quantitative perfusion parameters by dynamic contrast-enhanced sonography using a deconvolution method. *Journal of ultrasound in medicine*, 31(4):595–608, 2012.

[186] Douglas Hanahan and Judah Folkman. Patterns and emerging mechanisms of the angiogenic switch during tumorigenesis. *cell*, 86(3):353–364, 1996.

[187] Meng-Xing Tang and Robert J Eckersley. Nonlinear propagation of ultrasound through microbubble contrast agents and implications for imaging. *IEEE transactions on ultrasonics, ferroelectrics, and frequency control*, 53(12), 2006.

[188] Hojun Yu, Hyun-Jung Jang, Tae Kyoung Kim, Korosh Khalili, Ross Williams, Gord Lueck, John Hudson, and Peter N Burns. Pseudoenhancement within the local ablation zone of hepatic tumors due to a nonlinear artifact on contrast-enhanced ultrasound. *American Journal of Roentgenology*, 194(3):653–659, 2010.

[189] Nebojsa Duric, Peter Littrup, Lou Poulo, Alex Babkin, Roman Pevzner, Earle

Holsapple, Olsi Rama, and Carri Glide. Detection of breast cancer with ultrasound tomography: First results with the computed ultrasound risk evaluation (cure) prototype. *Medical physics*, 34(2):773–785, 2007.

[190] Nicole V Ruiter, Michael Zapf, Torsten Hopp, Robin Dapp, Ernst Kretzek, Matthias Birk, Benedikt Kohout, and Hartmut Gemmeke. 3d ultrasound computer tomography of the breast: A new era? *European journal of radiology*, 81:S133–S134, 2012.

[191] Libertario Demi, Hessel Wijkstra, and Massimo Mischi. Cumulative phase delay between second harmonic and fundamental components—a marker for ultrasound contrast agents. *The Journal of the Acoustical Society of America*, 136(6):2968–2975, 2014.

[192] Libertario Demi, Ruud JG Van Sloun, Hessel Wijkstra, and Massimo Mischi. Cumulative phase delay imaging for contrast-enhanced ultrasound tomography. *Physics in medicine and biology*, 60(21):L23, 2015.

[193] Frank Natterer. *The mathematics of computerized tomography*. SIAM, 2001.

[194] M O'Donnell, ET Jaynes, and JG Miller. Kramers–kronig relationship between ultrasonic attenuation and phase velocity. *The Journal of the Acoustical Society of America*, 69(3):696–701, 1981.

[195] Thomas L Szabo. *Diagnostic ultrasound imaging: inside out*. Elsevier, -, 2004.

[196] Libertario Demi, Koen Van Dongen, and Martin Verweij. A contrast source method for nonlinear acoustic wave fields in media with spatially inhomogeneous attenuation. *The Journal of the Acoustical Society of America*, 129(3):1221–1230, 2011.

[197] Enrico Boni, Luca Bassi, Alessandro Dallai, Francesco Guidi, Alessandro Ramalli, Stefano Ricci, James Housden, and Piero Tortoli. A reconfigurable and programmable fpga-based system for nonstandard ultrasound methods. *IEEE transactions on ultrasonics, ferroelectrics, and frequency control*, 59(7):1378–1385, 2012.

[198] FT d'Astous and FS Foster. Frequency dependence of ultrasound attenuation and backscatter in breast tissue. *Ultrasound in medicine & biology*, 12(10):795–808, 1986.

[199] Cuiping Li, Nebojsa Duric, Peter Littrup, and Lianjie Huang. In vivo breast sound-speed imaging with ultrasound tomography. *Ultrasound in medicine & biology*, 35(10):1615–1628, 2009.

[200] Kathryn Hibbs, Robert J Eckersley, Alison Noble, and Meng-Xing Tang. Ultrasound phase velocities in sonovue™ as a function of pressure and bubble concentration. In *Ultrasonics Symposium (IUS), 2009 IEEE International*, pages 1829–1832. IEEE, 2009.

[201] Jakob Nebeker and Thomas R Nelson. Imaging of sound speed using reflection ultrasound tomography. *Journal of Ultrasound in Medicine*, 31(9):1389–1404, 2012.

[202] Kenneth Hoyt, Benjamin Castaneda, Man Zhang, Priya Nigwekar, P Anthony

di Sant'Agnese, Jean V Joseph, John Strang, Deborah J Rubens, and Kevin J Parker. Tissue elasticity properties as biomarkers for prostate cancer. *Cancer Biomarkers*, 4(4-5):213–225, 2008.

[203] Kathryn Nightingale, Stephen McAleavey, and Gregg Trahey. Shear-wave generation using acoustic radiation force: in vivo and ex vivo results. *Ultrasound in medicine & biology*, 29(12):1715–1723, 2003.

[204] Jérémy Bercoff, Mickael Tanter, and Mathias Fink. Supersonic shear imaging: a new technique for soft tissue elasticity mapping. *IEEE transactions on ultrasonics, ferroelectrics, and frequency control*, 51(4):396–409, 2004.

[205] Mark L Palmeri, Michael H Wang, Jeremy J Dahl, Kristin D Frinkley, and Kathryn R Nightingale. Quantifying hepatic shear modulus in vivo using acoustic radiation force. *Ultrasound in medicine & biology*, 34(4):546–558, 2008.

[206] Michael H Wang, Mark L Palmeri, Cynthia D Guy, Liu Yang, Laurence W Hedlund, Anna Mae Diehl, and Kathryn R Nightingale. In vivo quantification of liver stiffness in a rat model of hepatic fibrosis with acoustic radiation force. *Ultrasound in medicine & biology*, 35(10):1709–1721, 2009.

[207] Michael H Wang, Mark L Palmeri, Veronica M Rotemberg, Ned C Rouze, and Kathryn R Nightingale. Improving the robustness of time-of-flight based shear wave speed reconstruction methods using ransac in human liver in vivo. *Ultrasound in medicine & biology*, 36(5):802–813, 2010.

[208] Ned C Rouze, Michael H Wang, Mark L Palmeri, and Kathryn R Nightingale. Robust estimation of time-of-flight shear wave speed using a radon sum transformation. *IEEE transactions on ultrasonics, ferroelectrics, and frequency control*, 57(12), 2010.

[209] Joyce McLaughlin and Daniel Renzi. Shear wave speed recovery in transient elastography and supersonic imaging using propagating fronts. *Inverse Problems*, 22(2):681, 2006.

[210] Ivan Nenadic, Matthew W Urban, Bo Qiang, Shigao Chen, and James Greenleaf. Model-free quantification of shear wave velocity and attenuation in tissues and its in vivo application. *The Journal of the Acoustical Society of America*, 134(5):4011–4011, 2013.

[211] A Cemal Eringen. Mechanics of continua. *Huntington, NY, Robert E. Krieger Publishing Co., 1980. 606 p.*, 1, 1980.

[212] Ned C Rouze, Yufeng Deng, Mark L Palmeri, and Kathryn R Nightingale. Robust characterization of viscoelastic materials from measurements of group shear wave speeds. In *Ultrasonics Symposium (IUS), 2016 IEEE International*, pages 1–4. IEEE, 2016.

[213] Mallory R Selzo and Caterina M Gallippi. Viscoelastic response (visr) imaging for assessment of viscoelasticity in voigt materials. *IEEE transactions on ultrasonics, ferroelectrics, and frequency control*, 60(12):2488–2500, 2013.

[214] Jonathan H Langdon, Etana Elegbe, and Stephen A McAleavey. Single tracking location acoustic radiation force impulse viscoelasticity estimation (stl-ve): A method for measuring tissue viscoelastic parameters. *IEEE transactions on*

ultrasonics, ferroelectrics, and frequency control, 62(7):1225–1244, 2015.

[215] Thanasis Loupas, JT Powers, and Robert W Gill. An axial velocity estimator for ultrasound blood flow imaging, based on a full evaluation of the doppler equation by means of a two-dimensional autocorrelation approach. *IEEE transactions on ultrasonics, ferroelectrics, and frequency control*, 42(4):672–688, 1995.

[216] Jérémy Bercoff, Mickaël Tanter, Marie Muller, and Mathias Fink. The role of viscosity in the impulse diffraction field of elastic waves induced by the acoustic radiation force. *IEEE transactions on ultrasonics, ferroelectrics, and frequency control*, 51(11):1523–1536, 2004.

[217] John A Nelder and Roger Mead. A simplex method for function minimization. *The computer journal*, 7(4):308–313, 1965.

[218] Ned C Rouze, Mark L Palmeri, and Kathryn R Nightingale. An analytic, fourier domain description of shear wave propagation in a viscoelastic medium using asymmetric gaussian sources. *The Journal of the Acoustical Society of America*, 138(2):1012–1022, 2015.

[219] Raffaella Righetti, Mariapaola Righetti, Jonathan Ophir, and Thomas A Krouskop. The feasibility of estimating and imaging the mechanical behavior of poroelastic materials using axial strain elastography. *Physics in medicine and biology*, 52(11):3241, 2007.

[220] Anuj Chaudhry. Estimation of effective poissons ratio in non-homogeneous porous media using two ultrasound transducers: A feasibility study. *Imaging in Medicine*, 8(4), 2016.

[221] Mallika Sridhar and Michael F Insana. Ultrasonic measurements of breast viscoelasticity. *Medical physics*, 34(12):4757–4767, 2007.

[222] Michael F Insana, Claire Pellot-Barakat, Mallika Sridhar, and Karen K Lindfors. Viscoelastic imaging of breast tumor microenvironment with ultrasound. *Journal of mammary gland biology and neoplasia*, 9(4):393–404, 2004.

[223] Rudolph Emil Kalman et al. A new approach to linear filtering and prediction problems. *Journal of basic Engineering*, 82(1):35–45, 1960.

[224] Yue Wang and Michael F Insana. Viscoelastic properties of rodent mammary tumors using ultrasonic shear-wave imaging. *Ultrasonic imaging*, 35(2):126–145, 2013.

[225] Pengfei Song, Armando Manduca, Heng Zhao, Matthew W Urban, James F Greenleaf, and Shigao Chen. Fast shear compounding using robust 2-d shear wave speed calculation and multi-directional filtering. *Ultrasound in medicine & biology*, 40(6):1343–1355, 2014.

[226] Thomas A Stamey, Fuad S Freiha, John E McNeal, Elise A Redwine, Alice S Whittemore, and Hans-Peter Schmid. Localized prostate cancer. relationship of tumor volume to clinical significance for treatment of prostate cancer. *Cancer*, 71(S3):933–938, 1993.

[227] Thomas Deffieux, Jean-Luc Gennisson, Laurence Bousquet, Marion Corouge, Simona Cosconea, Dalila Amroun, Simona Tripon, Benoit Terris, Vincent Mal-

let, Philippe Sogni, et al. Investigating liver stiffness and viscosity for fibrosis, steatosis and activity staging using shear wave elastography. *Journal of hepatology*, 62(2):317–324, 2015.

[228] Francis A Duck. Nonlinear acoustics in diagnostic ultrasound. *Ultrasound in medicine & biology*, 28(1):1–18, 2002.

[229] Koen Van Dongen and Martin Verweij. Sensitivity study of the acoustic nonlinearity parameter for measuring temperatures during high intensity focused ultrasound treatment. *Journal of the Acoustical Society of America*, 123(5):3225, 2008.

[230] Charles A Cain. Ultrasonic reflection mode imaging of the nonlinear parameter b/a: I. a theoretical basis. *The Journal of the Acoustical Society of America*, 80(1):28–32, 1986.

[231] WK Law, LA Frizzell, and F Dunn. Determination of the nonlinearity parameter b/a of biological media. *Ultrasound in medicine & biology*, 11(2):307–318, 1985.

[232] Dong Zhang and Xiu-Fen Gong. Experimental investigation of the acoustic nonlinearity parameter tomography for excised pathological biological tissues. *Ultrasound in medicine & biology*, 25(4):593–599, 1999.

[233] Matthieu Toulemonde, François Varray, Olivier Basset, Piero Tortoli, and Christian Cachard. High frame rate compounding for nonlinear b/a parameter ultrasound imaging in echo mode—simulation results. In *Acoustics, Speech and Signal Processing (ICASSP), 2014 IEEE International Conference on*, pages 5153–5157. IEEE, 2014.

[234] Robert T Beyer. Parameter of nonlinearity in fluids. *The Journal of the Acoustical Society of America*, 31(11):1586–1586, 2005.

[235] Mark F Hamilton, David T Blackstock, and et al. *Nonlinear acoustics*, volume 237. Academic Press, San Diego, 1998.

[236] Libertario Demi and Martin Verweij. Nonlinear acoustics. In *Comprehensive Biomedical Physics*. Elsevier, in press, The Netherlands, 2014.

[237] Libertario Demi, Martin D Verweij, and Koen WA van Dongen. Modeling three-dimensional nonlinear acoustic wave fields in media with spatially varying coefficient of nonlinearity, attenuation and speed of sound. In *Ultrasonics Symposium (IUS), 2012 IEEE International*, pages 519–522. IEEE, 2012.

[238] PNT Wells. Absorption and dispersion of ultrasound in biological tissue. *Ultrasound in medicine & biology*, 1(4):369–376, 1975.

[239] Francis A. Duck. *Physical properties of tissues: a comprehensive reference book*. Academic Press, 1990.

[240] Jacobus Huijssen. Modeling of nonlinear medical diagnostic ultrasound. 2008.

[241] Louis Leithold. The calculus with analytic geometry. 1986.

[242] CH Su and CS Gardner. Korteweg-de vries equation and generalizations. iii. derivation of the korteweg-de vries equation and burgers equation. *Journal of Mathematical Physics*, 10(3):536–539, 1969.

[243] Piero Tortoli, Luca Bassi, Enrico Boni, and et al. Ula-op: an advanced open platform for ultrasound research. *Ultrasonics, Ferroelectrics and Frequency Control, IEEE Transactions on*, 56(10):2207–2216, 2009.

[244] Luc MJ Florack, Bart M ter Haar Romeny, Jan J Koenderink, and Max A Viergever. Scale and the differential structure of images. *Image and Vision Computing*, 10(6):376–388, 1992.

[245] Fang Dong, Ernest L Madsen, MacDonald, and et al. Nonlinearity parameter for tissue-mimicking materials. *Ultrasound in medicine & biology*, 25(5):831–838, 1999.

[246] Laugier P Baldeweck, T, A Herment, and et al. Application of autoregressive spectral analysis for ultrasound attenuation estimation: interest in highly attenuating medium. *Ultrasonics, Ferroelectrics and Frequency Control, IEEE Transactions on*, 42(1):99–110, 1995.

[247] Marius Cloostermans and Johan Thijssen. A beam corrected estimation of the frequency dependent attenuation of biological tissues from backscattered ultrasound. *Ultrasonic Imaging*, 5(2):136–147, 1983.

[248] Hyungsuk Kim and Tomy Varghese. Attenuation estimation using spectral cross-correlation. *Ultrasonics, Ferroelectrics and Frequency Control, IEEE Transactions on*, 54(3):510–519, 2007.

[249] World Cancer Research Fund International. Breast cancer statistics, 2012.

[250] Martin J Yaffe and James G Mainprize. Risk of Radiation-induced Breast Cancer from Mammographic Screening. *Radiology*, 258(1):98–105, 2011.

[251] Susan G Moore, Pareen J Shenoy, Laura Fanucchi, John W Tumeh, and Christopher R Flowers. Cost-effectiveness of MRI compared to mammography for breast cancer screening in a high risk population. *BMC health services research*, 9(1):1, 2009.

[252] Ako Itoh, Ei Ueno, Eriko Tohno, Hiroshi Kamma, Hideto Takahashi, Tsuyoshi Shiina, Makoto Yamakawa, and Takeshi Matsumura. Breast disease: clinical application of us elastography for diagnosis. *Radiology*, 239(2):341–350, 2006.

[253] Federico Badalà, Kouros Nouri-mahdavi, and Duna A Raoof. In Vivo Breast Sound-Speed Imaging with Ultrasound Tomography. *Ultrasound in medicine & biology*, 144(5):724–732, 2008.

[254] Michael A Jacobs, Peter B Barker, David A Bluemke, Cindy Maranto, Cheryl Arnold, Edward H Herskovits, and Zaver Bhujwalla. Benign and malignant Breast lesions: diagnosis with multiparametric MR imaging 1. *Radiology*, 229(1):225–232, 2003.

[255] Nicole V. Ruiter, Michael Zapf, Torsten Hopp, Robin Dapp, Ernst Kretzek, Matthias Birk, Benedikt Kohout, and Hartmut Gemmeke. 3D ultrasound computer tomography of the breast: A new era? *European Journal of Radiology*, 81:S133–S134, 2012.

[256] Libertario Demi, Ruud J. G. Van Sloun, Hessel Wijkstra, and Massimo Mischi. Towards Dynamic Contrast Specific Ultrasound Tomography. *Scientific Reports*,

6:34458, 2016.

[257] Rogier R Wildeboer, Arnoud W Postema, Libertario Demi, Maarten PJ Kuenen, Hessel Wijkstra, and Massimo Mischi. Multiparametric dynamic contrast-enhanced ultrasound imaging of prostate cancer. *European radiology*, 27(8):3226–3234, 2017.

[258] RR Wildeboer, SG Schalk, L Demi, H Wijkstra, and M Mischi. Three-dimensional histopathological reconstruction as a reliable ground truth for prostate cancer studies.

[259] Tiantian Xu and Gregory R Bashford. Lateral blood flow velocity estimation based on ultrasound speckle size change with scan velocity. *IEEE transactions on ultrasonics, ferroelectrics, and frequency control*, 57(12), 2010.

[260] Jeffrey R Jackson, MP Seed, CH Kircher, DA Willoughby, and JD Winkler. The codependence of angiogenesis and chronic inflammation. *The FASEB Journal*, 11(6):457–465, 1997.

[261] Christian Demitri, Alessandro Sannino, Francesco Conversano, Sergio Casciaro, Alessandro Distante, and Alfonso Maffezzoli. Hydrogel based tissue mimicking phantom for in-vitro ultrasound contrast agents studies. *Journal of Biomedical Materials Research Part B: Applied Biomaterials*, 87(2):338–345, 2008.

[262] Fanglue Lin, Sarah E Shelton, David Espíndola, Juan D Rojas, Gianmarco Pinton, and Paul A Dayton. 3-d ultrasound localization microscopy for identifying microvascular morphology features of tumor angiogenesis at a resolution beyond the diffraction limit of conventional ultrasound. *Theranostics*, 7(1):196, 2017.

[263] David Huang, Eric A Swanson, Charles P Lin, Joel S Schuman, William G Stinson, Warren Chang, Michael R Hee, Thomas Flotte, Kenton Gregory, Carmen A Puliafito, et al. Optical coherence tomography. *Science (New York, NY)*, 254(5035):1178, 1991.

[264] Meng-Xing Tang, Naohisa Kamiyama, and Robert J Eckersley. Effects of nonlinear propagation in ultrasound contrast agent imaging. *Ultrasound in medicine & biology*, 36(3):459–466, 2010.

[265] Shigao Chen, William Sanchez, Matthew R Callstrom, Brian Gorman, Jason T Lewis, Schuyler O Sanderson, James F Greenleaf, Hua Xie, Yan Shi, Michael Pashley, et al. Assessment of liver viscoelasticity by using shear waves induced by ultrasound radiation force. *Radiology*, 266(3):964–970, 2013.

[266] Simon Chatelin, Jean-Luc Gennisson, Miguel Bernal, Mickael Tanter, and Mathieu Pernot. Modelling the impulse diffraction field of shear waves in transverse isotropic viscoelastic medium. *Physics in medicine and biology*, 60(9):3639, 2015.

Acknowledgements

First and foremost, I would like to thank my co-promotor Dr. ir. Massimo Mischi. Massimo, we first met when I started to work on my Master's thesis at Philips Research. After a few months, without knowing much of me, you offered me a PhD position in the prostate cancer imaging project of your group. A prestigious position, which I gladly accepted. Across this period, I was given an incredible amount of freedom to experiment and do what I thought was best. I could follow my scientific "nose" wherever it would take me (more often than not without knowing whether it would ever lead to something useful for the project), and you have never told me to let something go. I have tremendous appreciation for the trust you have put in me. It allowed me to grow very quickly and it put me a creative zone. Over the last few years, we had many work-related discussions, but also plenty others that could range from the purpose of life to the warmth that pets can bring to it. Combine this with a location such as the Taipei 101 sky-bar, and it is not strange that we forgot about time and ended up way too late for our dinner appointment. It made the travels to and around conferences very pleasant.

Secondly, I want to thank my promotor, Prof. dr. ir. Hessel Wijkstra. I admire the no-nonsense down-to-earth way in which you approach clinically-driven technical research. When needed, you criticised and thoroughly tested the validity and applicability of my work. Although dealing with such criticism may seem tough, this was actually not at all the case, as I also got to know you as a truly warm person that is always willing to help and gets the very best out of a person.

Then I would like to thank Dr. Libertario Demi. Libe, it is you who inspired me to pursue a PhD, and I am grateful that I had the privilege to do research with such a talented and passionate scientist. We spend many days in the lab together, "engineering" ultrasound phantoms out of (Dr. Oetker) gelatin, building a (leaky) tubing system, imaging very small lipid-shelled bubbles flowing through it, and finally sharing an extreme happiness that only few will understand when we actually measured the tiny phase shifts we hoped to see. We had a great time, published papers together and became friends. I sincerely hope that we get the chance to collaborate again in the future.

The research presented in this thesis was conducted within a project team of highly dedicated engineers and clinicians. Maudy, Arnoud and Christophe; as clinicians your inputs have been crucial to ensure that the technology we develop is actually implementable and meaningful in clinical routine. Thanks to your efforts we have established an ever growing database of measurements that is indispensable for the development and validation of our algorithms. I have learned a lot from our long consensus meetings at the hospital, while enjoying the real "Bossche Bollen" kindly provided by Maudy.

In line with this, I would like to thank Dr. Harrie Beerlage for giving me the opportu-

nity to be in the OR and see a robot-assisted radical prostatectomy, accompanied with a clear explanation of the full procedure. I also want to thank you for inviting me to the yearly *Imaging in Urology* symposium, where I hope to shed some light on the future possibilities that ultrasound has to offer for urologists.

That brings me to my fellow-engineers in the team, Simona, Anastasiia, Libe, Stefan and Rogier. It is both inspiring and humbling to work with you, but besides that also just a lot of fun. Simona proved to be an excellent tour guide and every once in a while Stefan managed to squeeze in an admittedly funny *Limburger*-joke. Rogier, I am happy that we do a major part of our research together; everything becomes better and more enjoyable in good company, like playing some blues and jazz together in the late after work hours, or drinking a neat whisky and contemplating life.

I would then like to express my gratitude to the chairman of our Signal Processing Systems (SPS) group, Prof. dr. ir. Jan Bergmans, for facilitating a friendly and personal research environment, despite its considerable size. A warm thanks also goes to my other dearly valued colleagues in the SPS group, (to name a few) Rik, Chiara, Sebastiaan, Piet, Nienke, Celine, Federica, Aline, Eleni, Guy, Salvatore, Paul, Linda and Mustafa. I had the pleasure to work with some of you, while others proved to be great discussion partners during the enjoyable after-work "borrels" or mood-boosters with *Brabantse gezelligheid* like Nienke. Then I would like to gratefully thank our secretaries, Marieke and Carla, who deal with the administrative mess that scientists tend to create, and manage that without ever losing their optimism and reassuring smiles.

I want to extend my gratitude to Prof. dr. Yonina Eldar for providing me the opportunity to work in her prestigious SAMPL lab at the Technion institute of technology in Israel. Oren, Regev, Tanja, Gal, and Shahar, you made me feel extremely welcome, and immediately invited me for parties and drinks in the beautiful city of Haifa. The day after Oren figured out that I did not bring my beloved guitar to Israel, his own guitar was waiting for me on my new desk. Thanks!

Dan wil ik graag nog een aantal mensen in mijn privésfeer bedanken: Allereerst natuurlijk mijn familie en vrienden, voor alle gezelligheid en de welkome afleiding. Het was af en toe ook hard nodig.

Naast het doen van onderzoek heb ik de afgelopen jaren met een bijzondere groep mensen intensief muziek mogen maken. Niels, Job, Rim en Bart, ik heb genoten van alle uren en dagen die we door de jaren heen samen in de (vaak muffe) repetitieruimtes en op de diverse poppodia hebben doorgebracht. Ik hoop dat we ook in de toekomst de tijd kunnen vinden om dit te blijven doen.

Dan wil ik mijn paranimfen Bart en Niels bedanken: mijn broertje en neef, maar vooral ook mijn beste vrienden. Jullie zijn beiden ontzettend belangrijk voor mij en ik ben dan ook erg blij dat juist jullie aan mijn zijde staan. Daarnaast wil ik Jelle Janssen bedanken voor alle tijd en energie die hij in het ontwerpen van het fantastische artwork van dit boekje heeft gestoken. Het is mooier geworden dan ik had kunnen bedenken.

Ik wil ook mijn schoonouders Jac en Aggie bedanken, waar ik altijd welkom ben en al jaren een tweede thuis heb mogen vinden.

Een woord van dank ook voor mijn oom John, de eerste die me uitlegde wat spanning en stroom nu precies waren. Ik zal de middagen en avonden waarop we samen pedalboards en robotjes in elkaar waren aan het solderen nooit vergeten. Het heeft er

waarschijnlijk voor gezorgd dat ik Elektrotechniek ben gaan studeren en uiteindelijk op dit punt ben beland.

Pap, mam; aan jullie ben ik heel veel verschuldigd. Door jullie ben ik geworden wie ik nu ben en ik ben jullie erg dankbaar voor alle steun en de liefdevolle, warme jeugd die ik heb mogen genieten. Ik ben opgegroeid in een ontzettend stimulerende omgeving waarbij het aan enthousiasme nooit ontbrak en jullie altijd interesse hadden in wat me bezighield. Bedankt voor jullie vertrouwen in mij, dat zelfs niet wankelde toen ik aan het einde van het VWO spontaan overwoog om muzikant te worden in plaats van een baanzekere opleiding te volgen aan een technische universiteit.

Een laatste dankjewel is bestemd voor een speciaal persoon. Femke, met jou heb ik deze reis samen doorlopen. Een reis waarin je niet alleen de mooie dingen van het promoveren met me hebt gedeeld en gevierd, maar er ook voor me was tijdens de momenten waarop het even niet mee zat. Zonder jouw steun, liefde en de vele gezellige etentjes na het werk was dit proefschrift er niet geweest. Je realisme is ontwapenend en je was buitengewoon goed in staat om me met beide benen op de grond zetten als ik weer eens te diep in gedachten was verzonken over het werk en dit onderzoek. Ik kijk er naar uit om samen nog veel mooie dingen te beleven.

– Ruud

About the author

Ruud van Sloun was born in Roermond, The Netherlands, in 1990. After completing pre-university education at the Connect college in Echt, he studied Electrical Engineering at the Eindhoven University of Technology in The Netherlands, where he graduated with honours and received the MSc. degree with distinction cum laude in 2014. During his study, he completed two internships at Philips Research Eindhoven, working on signal processing solutions for array sensing technology and medical ultrasound imaging, respectively. He then continued as a PhD candidate in the Signal Processing Systems group of the Eindhoven University of Technology, carrying out research on prostate cancer localization by advanced ultrasound imaging. Ruud has authored over 30 publications, including 12 papers in international peer-reviewed scientific journals, two of which were selected as featured articles by the editorial boards of the IEEE Transactions on Medical Imaging, and Physics in Medicine & Biology, respectively. A third paper was part of the 2016 IEEE Transactions on Ultrasonics, Ferroelectrics, and Frequency Control "Editor's selection". His paper "Entropy of ultrasound-contrast-agent velocity fields for angiogenesis imaging of prostate cancer" received the 2015-2016 best paper award of the IEEE-EMBS Belelux chapter. In 2017, Ruud received the EFSUMB Young Investigator's award from the European Federation of Societies for Ultrasound in Medicine and Biology for his research on prostate cancer localization with contrast-enhanced ultrasound. His current research interests include quantitative ultrasound imaging, signal and image processing, compressed sensing, machine learning and artificial intelligence.